

THE COSMOLOGICAL CONTEXT OF THE  
MILKY WAY THROUGH THE ANALYSIS OF  
GALACTIC SURVEYS AND NUMERICAL  
SIMULATIONS

J. Ted Mackereth

Astrophysics Research Institute

A thesis submitted in partial fulfilment of the requirements of

Liverpool John Moores University

for the degree of

Doctor of Philosophy.

December 2018

# **Declaration**

The work presented in this thesis was carried out at the Astrophysics Research Institute, Liverpool John Moores University. Unless otherwise stated, it is the original work of the author.

While registered as a candidate for the degree of Doctor of Philosophy, for which submission is now made, the author has not been registered as a candidate for any other award. This thesis has not been submitted in whole, or in part, for any other degree.

J. Ted Mackereth  
Astrophysics Research Institute  
Liverpool John Moores University  
IC2, Liverpool Science Park  
146 Brownlow Hill  
Liverpool  
L3 5RF  
UK

SEPTEMBER 4, 2018

# **Abstract**

Add abstract here

# **Publications**

In the course of completing the work presented in this thesis, the following papers have been submitted for publication in a refereed journal:

[Add publication list here](#)

# Acknowledgements

Add acknowledgements here

*“Handle a book as a bee does a flower, extract its sweetness but do not damage it.”*

- John Muit

**“OH, NO! NOT THE BEES! NOT THE BEES! AAAAHHHHH! OH, THEY'RE IN  
MY EYES! MY EYES! AAAHHHHH! AAAAGGHHH!”**

- Nicolas Cage

# Contents

<b>Declaration</b>	ii
<b>Abstract</b>	iii
<b>Publications</b>	iv
<b>Acknowledgements</b>	v
<b>Contents</b>	vii
List of Tables . . . . .	viii
List of Figures . . . . .	ix
<b>1 APOGEE</b>	1
1.1 Introduction . . . . .	1
1.2 Data . . . . .	5
1.2.1 The APOGEE Catalogue . . . . .	5
1.2.2 Distance estimates . . . . .	9
1.2.3 Age estimates . . . . .	10
1.3 Method . . . . .	16

1.3.1	Density Fitting Procedure . . . . .	17
1.3.2	Adopted stellar number density models . . . . .	20
1.3.3	Stellar surface-mass densities . . . . .	21
1.4	Results . . . . .	22
1.4.1	The radial profile of mono-age, mono-[Fe/H] populations . .	23
1.4.2	The vertical profile of the disk . . . . .	27
1.4.3	The mass contribution of mono-age, mono-[Fe/H] populations	28
1.5	Discussion . . . . .	32
1.5.1	Surface-mass density systematics . . . . .	36
1.5.2	Comparison with MAPs results . . . . .	38
1.5.3	Comparison with other Milky Way disk studies . . . . .	40
1.5.4	Implications for the formation of the Galactic disk . . . . .	42
1.6	Conclusions . . . . .	49
1.7	Density Fits . . . . .	53
1.8	The effect of uncertainties on trends with age . . . . .	56
<b>2</b>	<b>EAGLE</b>	<b>59</b>
2.1	Introduction . . . . .	59
2.2	Numerical Simulations & methods . . . . .	64
2.2.1	The EAGLE simulations . . . . .	64
2.2.2	Identification and characterisation of galaxies . . . . .	67
2.3	The elemental abundances of disc stars in Milky Way-like galaxies . .	69
2.3.1	The distribution of disc stars on the $[\alpha/\text{Fe}]-[\text{Fe}/\text{H}]$ plane . . .	70

2.3.2	Galaxy-to-galaxy diversity of $\alpha$ -enrichment . . . . .	78
2.4	The origin of the $[\alpha/\text{Fe}]-[\text{Fe}/\text{H}]$ distribution of disc stars . . . . .	82
2.4.1	Applicability to galaxies in the Ref-L100N1504 simulation . .	90
2.5	Connecting disc star element abundances to halo mass accretion histories	93
2.6	Summary and discussion . . . . .	96
2.7	Subgrid physics variations . . . . .	102
<b>3</b>	<b>High Eccentricity Population</b>	<b>104</b>
3.1	Introduction . . . . .	104
3.2	Sample and Data . . . . .	108
3.2.1	APOGEE DR14 . . . . .	108
3.2.2	<i>Gaia</i> DR2 and cross matching . . . . .	109
3.2.3	Orbital parameters . . . . .	111
3.2.4	The EAGLE simulations . . . . .	111
3.3	The high eccentricity halo population . . . . .	113
3.3.1	Chemical Compositions . . . . .	118
3.3.2	Kinematics . . . . .	126
3.4	Accreted Stellar Populations in EAGLE . . . . .	128
3.5	Summary and Conclusions . . . . .	135
3.6	Modelling as a function of $[\text{Fe}/\text{H}]$ . . . . .	137
<b>A</b>	<b>Example Appendix</b>	<b>139</b>

# List of Tables

2.1 Basic properties of the three present-day galaxies shown in Figure ??.	78
The rows correspond to, respectively: the labels applied to each galaxy in the text, their Galaxy ID and FOF ID in public EAGLE galaxy catalogues, their stellar mass, halo mass, their specific star formation rate (sSFR), their $\kappa_{\text{co}}$ value, and their half-mass radius. . . . .	78

# List of Figures

1.1	The full RGB sample in $[\alpha/\text{Fe}]$ – $[\text{Fe}/\text{H}]$ space. The coloured regions show our division between low and high $[\alpha/\text{Fe}]$ subsamples. At each $[\text{Fe}/\text{H}]$ the division between the samples is $[\alpha/\text{Fe}] = 0.05$ dex, roughly twice the mean uncertainty on $[\alpha/\text{Fe}]$ abundance determinations in APOGEE DR12. The bimodality in $[\alpha/\text{Fe}]$ at fixed $[\text{Fe}/\text{H}]$ is visible across many $[\text{Fe}/\text{H}]$ , and the lower number of stars in the high $[\alpha/\text{Fe}]$ sample is clear from this plot. . . . .	7
1.2	2D histograms of the spatial distribution (in Galactocentric $R$ and $Z$ ) of the high and low $[\alpha/\text{Fe}]$ subsamples shown in Figure ???. The high $[\alpha/\text{Fe}]$ sample appears more diffuse and extended in height even before selection effects are accounted for. Readers should notice the different colour scale adopted for each panel, due to the much lower number of stars in the high $[\alpha/\text{Fe}]$ sample. . . . .	8

1.3 Comparison of APOGEE red clump catalogue (APOGEE-RC) distances $D_{RC}$ with distances derived by ?, $D_{MH}$ . The top panel directly compares the distances, where the bottom panel shows the difference as a fraction of $D_{MH}$ , as a function of that distance. There are many stars with good agreement, but a distinct fraction of MH distances are underestimated compared to RC ( $\sim 20\%$ with distances underestimated by more than $\sim 10\%$ ). As the variations in the density occur on scales which are, in general, far larger than these discrepancies, these are not problematic in our analysis. The two distance scales differ systematically by a factor of $\sim 5\%$ , but we do not correct for this in the following discussion and it does not impact any of our results. . . . .	11
1.4 Asteroseismically determined ages from APOKASC against the [C/M] and [N/M] based ages from ?. The line gives the fitted correction for ages from ?, based on the values for the APOKASC training set, given in their Table 1. We fit the data using a non-parametric lowess fit. Before corrections, older ages are under-predicted, and young ages are over-predicted. The corrections mainly change the scaling of the ages, such that the high $[\alpha/\text{Fe}]$ sample occupies an age range more in-line with the existing literature (e.g. ??) . . . . .	14
1.5 2D Histograms showing the raw number of stars in each (age,[Fe/H]) bin of the low ( <i>left</i> ) and high ( <i>right</i> ) $[\alpha/\text{Fe}]$ sub-samples. We draw the reader’s attention to the difference in amplitude between the two sub-samples (and the associated difference in colour scale normalisation). Although the majority of bins are well sampled ( $\gtrsim 30$ stars), there are some greatly undersampled bins, for which well-defined fits are not possible. . . . .	15



1.9 Mean $h_Z$ at $R_0$ ( <i>left</i> ) and $R_{\text{flare}}^{-1}$ ( <i>right</i> ) against age. The mean value in each age bin is calculated by multiplying together the posterior PDFs of the density fits. The panels show both the low ( <i>purple</i> ) and high ( <i>green</i> ) $[\alpha/\text{Fe}]$ populations. The left panel shows the total surface-mass density weighted mean as a dashed line, which demonstrates that the vertical distribution of the high $[\alpha/\text{Fe}]$ population is only important at the solar radius at old ages due to its low surface-mass density contribution. $h_Z$ increases with age for both low and high $[\alpha/\text{Fe}]$ populations. $R_{\text{flare}}^{-1}$ behaves similarly for the low $[\alpha/\text{Fe}]$ population, meaning flaring decreases with age, but the high $[\alpha/\text{Fe}]$ population shows an opposite behaviour. . . . .	30
1.10 The surface-mass density contribution of mono-age, mono-[Fe/H] populations at $R_0$ (where low and high $[\alpha/\text{Fe}]$ are combined). The total contribution $\Sigma_{R_0, \text{tot}}$ is displayed at the top of the main panel. The colour scale is linear and spans the surface-mass density range between $0 < \Sigma_{R_0} < 1.5 \text{ M}_\odot \text{ pc}^{-2}$ . The marginalised distributions along each axis are shown above and to the right. The mass at the solar radius increases monotonically with both age and [Fe/H]. . . . .	33
1.11 The surface-mass density contributions of the low ( <i>left</i> ) and high ( <i>right</i> ) $[\alpha/\text{Fe}]$ sub-samples. The total contributions $\Sigma_{R_0, \text{tot}}$ are displayed at the top of each panel. We draw the attention of the reader to the difference in colour scale between the high and low $[\alpha/\text{Fe}]$ panels, which differs by an order of magnitude, and is adopted to better show the behaviour in the high $[\alpha/\text{Fe}]$ sample. The low $[\alpha/\text{Fe}]$ sub-sample has mass at all ages and [Fe/H] but is concentrated mostly at young ages. The high $[\alpha/\text{Fe}]$ sub-sample contributes far less mass and is concentrated at old age. . . . .	34



1.14 The surface-mass density weighted [Fe/H] distribution (MDF) at 3 radii for profiles fit to the low $[\alpha/\text{Fe}]$ populations. The distribution shown is marginalised in age across all our age bins. The coloured bands give the 95% uncertainty ranges, where uncertainties are dominated by those on the fitted density profiles. The mean [Fe/H] is lower at greater $R$ . Qualitatively, the skew of the MDF's changes with $R$ , such that the innermost $R$ has a tail going to low [Fe/H], and the outermost $R$ has a tail going to high [Fe/H] . . . . .	45
1.15 The behaviour of $R_{\text{peak}}$ with age and [Fe/H] for the low $[\alpha/\text{Fe}]$ populations. The high $[\alpha/\text{Fe}]$ populations are better fit by single exponentials, and so $R_{\text{peak}}$ is not an informative diagnostic of these populations. The coloured lines and bands give the surface-mass density weighted mean and standard deviation within an age or [Fe/H] bin. The mean $R_{\text{peak}}$ does not vary significantly with age, whereas it shows a clear decrease with [Fe/H]. However, the dispersion in $R_{\text{peak}}$ does increase with age for low $[\alpha/\text{Fe}]$ populations. High $[\alpha/\text{Fe}]$ populations show a slight increasing trend for increasing age and [Fe/H], albeit at low significance.	47
1.16 Comparison between the best fit models and the APOGEE data for mono-age, mono-[Fe/H] populations in the low $[\alpha/\text{Fe}]$ sub-sample. The grey histogram shows the distance modulus distribution of the APOGEE data for the mono-age, mono-[Fe/H] bin indicated by the ([Fe/H] [dex], age [Gyr]) coordinate given in each panel. The coloured curves show the distance modulus distribution found when the best fit broken exponential (black) and single exponential (red) density model is run through the effective selection function. It is clear that the broken exponential density model provides a qualitatively better fit to the data in all cases. . . . .	54

1.17 Comparison between the best fit models and the APOGEE data for mono-age, mono-[Fe/H] populations in the high $[\alpha/\text{Fe}]$ sub-sample. The grey histogram shows the distance modulus distribution of the APOGEE data for the mono-age, mono-[Fe/H] bin indicated by the $([\text{Fe}/\text{H}] [\text{dex}], \text{age} [\text{Gyr}])$ coordinate given in each panel. The coloured curves show the distance modulus distribution found when the best fit broken exponential (black) and single exponential (red) density model is run through the effective selection function. In many cases the red and black curves are indistinguishable (only red is seen), or very similar. In cases where the black and red curves are different, the red provides a qualitatively better fit. Bins with less than 30 stars (which we disregard for the majority of the analysis) are hatched out. . . . .	55
1.18 [id=TM]The resulting age- $h_Z$ trend from the monte carlo sampling of a set of mock density distributions. The input density models had $h_Z$ increasing monotonically with age (in bins of $\Delta\text{age} = 2 \text{ Gyr}$ ) from 0.2 to 1.2 kpc (shown by the <i>blue</i> dashed line). After sampling of the density distribution, we applied random errors of 40% to the mock ages, and measured the structural parameters using the exact density fitting method applied to the APOGEE data. The method is able to approximately recover the general shape of the input age- $h_Z$ relation, showing a clear trend with age. The age errors increase the error bar sizes significantly where mixing does occur, but the results are consistent with the input in most cases. . . . .	57
2.1 Two-dimensional histogram of the mass-weighted $[\alpha/\text{Fe}]\text{-}[\text{Fe}/\text{H}]$ distribution of all ‘disc stars’ associated with the 133 galaxies identified as broad analogues of the Milky Way in terms of their stellar mass and morphology (see Section ??) at $z = 0$ in Ref-L100N1504. The overplotted solid line shows the median $[\alpha/\text{Fe}]$ in bins of $\Delta[\text{Fe}/\text{H}] = 0.2$ , dashed lines show the interquartile range. . . . .	71

2.2 The mean mass fraction of the Fe, locked up in the disc stars of present-day Milky Way-like galaxies in Ref-L100N1504, that was synthesised by Type Ia SNe. The fraction is shown as a function of the stellar populations' position in $[\alpha/\text{Fe}]\text{-}[\text{Fe}/\text{H}]$ space. The value in each pixel is weighted by the current mass of the stellar particles within. Overplotted contours reproduce the mass distribution shown in Fig. ???. The Type Ia SNe Fe fraction broadly anti-correlates with $[\alpha/\text{Fe}]$ , and at fixed $[\alpha/\text{Fe}]$ the Fe mass fraction contributed by Type Ia SNe is greatest in Fe-poor stars. . . . .	73
2.3 The mean age of the disc stars of present day Milky Way-like galaxies in Ref-L100N1504, as a function of their position in $[\alpha/\text{Fe}]\text{-}[\text{Fe}/\text{H}]$ space. Pixel values are weighted by the current mass of the stellar particles within, and the overplotted contours reproduce the mass distribution shown in Fig. ???. Age correlates with $[\alpha/\text{Fe}]$ , though at any fixed $[\alpha/\text{Fe}]$ disc stars exhibit a broad range of mean ages, depending on their $[\text{Fe}/\text{H}]$ . At fixed $[\text{Fe}/\text{H}]$ , the most $\alpha$ -rich stellar populations tend to be the oldest. . . . .	75
2.4 The mean gas consumption timescale $t_g$ of the natal gas from which the disc stars of present-day Milky Way-like galaxies in Ref-L100N1504 formed, as a function of their position in $[\alpha/\text{Fe}]\text{-}[\text{Fe}/\text{H}]$ space. Pixel values are weighted by the current mass of the stellar particles within, and the overplotted contours reproduce the mass distribution shown in Fig. ???. At fixed $[\text{Fe}/\text{H}]$ , the most $\alpha$ -rich stellar particles formed from gas with the shortest consumption timescales. . . . .	77

2.5 Examples illustrating the diversity of the  $[\alpha/\text{Fe}]$ - $[\text{Fe}/\text{H}]$  distribution of disc stars from present-day galaxies in Ref-L100N1504. From left to right, the columns correspond to the galaxies labelled A, B and C in the text, for which key properties are quoted in Table ???. The two upper rows show mock images of the galaxies, with a  $50 \times 50$  kpc field of view, in the face-on and edge-on orientations. The images show the stellar light based on the combination of monochromatic  $u$ -,  $g$ - and  $r$ -band SDSS filters. The third row shows the  $[\alpha/\text{Fe}]$ - $[\text{Fe}/\text{H}]$  plane of the disc stars, with the dashed diagonal line positioned to broadly separate the high- and low- $[\alpha/\text{Fe}]$  sequences. This separation enables, in the bottom row, the contribution to the total (*black*) star formation history of the stars comprising the high- (*red*) and low- $[\alpha/\text{Fe}]$  (*blue*) sequences to be shown. Downward arrows denote the epoch by which half of the stellar particles comprising these populations formed. . . . . . . . . .

80





2.9	The mass accretion history, $M_{200}(t)$ , of haloes identified in the DMONLY-L100N1504 simulation. The thick curves corresponds to the median, whilst the shaded regions denote the interquartile range. The blue curve corresponds to the partner haloes of all 133 galaxies in our Milky Way-like sample, whilst the red curve corresponds to the partner haloes of the 6 galaxies exhibiting bimodality in $[\alpha/\text{Fe}]$ at fixed $[\text{Fe}/\text{H}]$ . Dashed curves meeting the two median curves at $z = 0$ show the typical accretion history, as parametrised by (?), of haloes with these $z = 0$ masses. Haloes which host galaxies exhibiting $[\alpha/\text{Fe}]$ bimodality have systematically different dark matter accretion histories . . . . .	95
2.10	The $[\alpha/\text{Fe}]\text{-}[\text{Fe}/\text{H}]$ distribution of Milky Way like galaxies in simulations of the L025N0376 volume. The left panel shows the distribution realised by the Ref-L025N0376 simulation, whilst the four panels on the right show that from simulations in which a parameter governing the number of Type SNIa per unit stellar mass formed, $\nu$ , or the characteristic e-folding timescale of the Type SNIa delay function, $\tau$ , has been varied. On these panels, the overlaid black contours are from the Ref-L025N0376 distribution, highlighting the significant changes to the $[\alpha/\text{Fe}]\text{-}[\text{Fe}/\text{H}]$ distribution induced by these parameter changes.	102
3.1	The $-[\text{Fe}/\text{H}]$ plane in APOGEE DR14, coloured by orbital eccentricity $e$ , as estimated using the method of ?. The points are plotted with the highest $e$ stars overlaying the points at lower $e$ , such that the highest $e$ populations stand out. It is clear that a population extends from $([\text{Fe}/\text{H}],) \sim (-2.0, 0.3)$ to $\sim (-1.0, 0.1)$ that appears to consist mainly of stars on highly eccentric orbits, with a distinct element abundance pattern to that of the Galactic disc (at $[\text{Fe}/\text{H}] > -0.7$ ). The dotted gray line reflects the cut in $[\text{Fe}/\text{H}]$ which is imposed to perform the $k$ -means analysis. . . . .	114

3.2 Eccentricity distributions of stars in three groups identified by performing a $k$ -means detection of structure in the eccentricity-[Fe/H]- -- space. The $k$ -means algorithm cleanly separates the accreted halo component into two groups, one characterised by low eccentricities (in red), and the other with a peak at very high $e$ (in blue). We show the stars assigned to the disc (with $[Fe/H] < -0.7$ ) in black as a comparison sample. . . . .	116
3.3 Distribution of the stars in the different $k$ -means groups in the - plane. High $e$ stars occupy preferentially the low , low region of the plot, a locus which was identified in ? as being common to accreted halo populations. Low $e$ group stars tend to be more distributed at higher and slightly higher . Discdisc stars (in black) are enhanced in Al and, to a lesser extent, Mg, relative to the high and low $e$ groups. . . . .	117
3.4 The raw metallicity distribution functions of the high and low $e$ populations. Unlike their low $e$ counterparts, the high $e$ population shows a strong peak at about $[Fe/H] \sim -1.3$ , resembling MDFs of Local Group dwarfs. The low $e$ group shows peaks at both $[Fe/H] \sim -2.1$ and $\sim -1.4$ , and stars piled up at the imposed upper $[Fe/H]$ limit at $[Fe/H] = -0.7$ . . . . .	120

- 3.5 The Magnesium, Aluminium and Nickel abundances of the  $k$ -means groups. These elements are good representations of  $\alpha$ , odd- $Z$  and Fe peak elements that are measured by APOGEE. The coloured bands show the interquartile range in bins of 50 stars sorted in increasing [Fe/H]. The high and low  $e$  populations are characterised by lower Mg and Al than the high- $\alpha$  stars. The bottom panel shows that the high  $e$  group has slightly lower [Ni/Fe] than the high- $\alpha$  population, whereas the low  $e$  group is essentially consistent with the high- $\alpha$  population in [Ni/Fe]. In all cases, the high  $e$  group median is slightly lower than the low  $e$  group at fixed [Fe/H]. The slightly higher [Fe/H] of the high  $e$  population is also evident here. Again, both groups are depleted in all these elements relative to the discdisc stars at that [Fe/H]. . . . . 122
- 3.6 The best fit models for  $\alpha$  as a function of [Fe/H] for the high and low  $e$   $k$ -means groups (shown top and bottom, respectively). The best fit model is shown by the blue and red lines, with the 95% confidence interval marked by the banded blue and red regions either side of this line (the fit for the other group is shown in each panel for reference). The raw data are shown by the black scatter points. The high  $e$  group is well-fit by a model with a break at  $[Fe/H] = -1.31^{+0.03}_{-0.06}$  and  $= 0.22^{+0.01}_{-0.08}$ , as indicated by the dashed crosshair. The low  $e$  group is better fit by a single linear relation in the same range of [Fe/H]. The position of the models also demonstrates the slightly higher  $\alpha$  of the low  $e$  group. . . . 124

- 3.7 The kinematics of the abundance selected stars from Figure ???. The distribution of azimuthal angular momentum  $L_z$  (*left*), maximum vertical excursion from the disc plane  $z_{\max}$  (*centre*), and the spherical apocentre radius of orbits  $r_{\text{ap}}$  (*right*), is shown for the high and low  $[\alpha/\text{Fe}]$  disc (red and yellow, respectively) and the accreted halo population (blue). The halo stars clearly occupy a very different orbital distribution, having low  $L_z$ , and distributions of  $z_{\max}$  and  $r_{\text{ap}}$  that extend to very large distances. The median  $L_z$  is slightly negative, while the median  $z_{\max}$  and  $r_{\text{ap}}$  are  $\sim 10$  and  $\sim 20$  kpc, respectively. All histograms are normalised such that the summed probability under *each* group is equal to unity. . . . . 125
- 3.8 Distribution of disc and accreted halo populations in spherical polar coordinate planes. On the left panel, the high  $e$  population occupies the same locus in  $v_R - v_\phi$  space (left panel) as the population identified by ?. The low  $e$  population splits into two populations according to  $v_\phi$ , with one prograde and one retrograde component, suggesting that this population may in fact be from a mix of disc contaminants and debris from smaller satellites. . . . . 129
- 3.9 The merger time  $z_{\text{merge}}$  of satellites accreted onto 22 Milky Way mass haloes in EAGLE against the median eccentricity  $e$  of their stellar debris at  $z = 0$ . The points are coloured by the stellar mass of the accreted galaxies at the time of the merger,  $M_*$ . The dashed horizontal line indicates  $e = 0.85$ , which is the median eccentricity of the high  $e$  group characterised in Section ???. Only the latest merged haloes have debris at the highest and lowest  $e$ , whereas early mergers tend to occupy intermediate  $e$ . The most massive mergers also occur later, with early mergers dominated by low mass haloes. . . . . 130

3.10 Median eccentricities at merger time $e_{z_{\text{merge}}}$ against median eccentricity at $z = 0$ $e_{z=0}$ for satellites accreted onto Milky Way mass haloes in EAGLE. The points are coloured by the stellar mass of the accreted galaxies at the time of the merger, $M_*$ . Debris which falls below the dashed unity line has been circularised following accretion, whereas the debris above this line has been radialised after accretion. The majority of debris has a similar $e$ at $z = 0$ to the time at which it was accreted, but a few accreted satellites are circularised/radialised following accretion. High mass satellite debris has undergone the least change in median $e$ .	133
---	-----

# Chapter 1

## APOGEE

### 1.1 Introduction

The understanding of the present day spatial, kinematic and chemical configuration of the stars of the Milky Way disk is a cornerstone of Galactic archaeology, placing key constraints on models of galaxy disk formation and evolution. Much of our understanding of the time evolution of galaxy disks like that of the Milky Way has arisen from studies which match galaxies of a given stellar mass at  $z = 0$  to their progenitors at higher  $z$  (and therefore, lookback time, e.g. ???). However, the Sun’s position in the Milky Way presents a high-fidelity insight into the structure of a Galactic disk on a star by star basis, which has provided a great many insights into the problem (e.g. ???). Data for large numbers of disk stars over a wide range of Galactocentric distances, including positions, chemical abundances and stellar ages are now becoming readily available, due to the advent of modern spectroscopic surveys such as APOGEE (?), Gaia-ESO (?) and GALAH (?), with future instruments aiming to bolster the ESA-*Gaia* data releases (?), such as WEAVE (?) and MOONS (?).

Galaxy disks are commonly considered to have stellar density distributions described by exponential laws of some form (e.g. ???), assumed classically as the result of gas collapse with angular momentum conservation (e.g. ?), and more recently, the

redistribution or ‘scrambling’ of the angular momentum of individual stars (e.g. ???). External disks have relatively well constrained photometric scale lengths (e.g. ?), but estimates of that of the Milky Way vary greatly (see ?, for a review), and seem to be in tension with those in external galaxies which are assumed to be similar to the Milky Way. This suggests a discord between internal and external scale length measurement methods, or that the Milky Way has a structure distinct from the bulk of disk galaxies.

In the Milky Way, the definition of the measured population appears to have a great effect on this estimate, with thicker, geometrically defined populations having generally flatter radial profiles (e.g. ?) than, for example, the populations enhanced in  $\alpha$ -element abundances (e.g. ???). Theoretical results have suggested that these *geometric* thick disks are formed from embedded flaring of co-eval populations (?). The discrepant scale lengths between geometric and abundance selected thick disks was framed most recently by ? as the result of a hitherto unaccounted-for radial age gradient in the disk.

When considered *in toto*, nearby galaxy disks, and the Milky Way disk, are observed to have a two-component vertical spatial structure, commonly referred to as the *geometric* ‘thick’ and ‘thin’ disks (?????). Classically, the ‘thick’ components have been characterised by older, kinematically hotter stellar populations, enriched in  $[\alpha/\text{Fe}]$ , whereas the ‘thin’ populations assume lower, near solar  $[\alpha/\text{Fe}]$  and are kinematically cooler (e.g. ?). It has, however, also been posited that these populations are in fact composed of multiple sub-populations that smoothly span this range of properties (e.g. ?????), thus, in terms of structural parameters, the disk cannot be characterised as the superposition of two distinct structures with different scale heights (?). It has been shown that the total vertical stellar spatial distribution resulting from the overlap of such sub-populations is consistent with a double exponential (see, e.g., Figure 14 of ?). It is difficult to explain the presence of a continuity in structure alongside the discontinuity in chemistry seen in the Milky Way.

The Milky Way’s disk has a complex chemical structure, with a bimodality in  $[\alpha/\text{Fe}]$  seen at fixed  $[\text{Fe}/\text{H}]$  across many of the observable regions of the disk (????). This characteristic is difficult to explain using one-zone Galactic chemical evolution (GCE) models (most recently shown by ?), giving rise to attempts to explain it by means

other than pure chemical evolution. Examples of such models include the heating of the old disk by high redshift mergers (e.g. ????) and the formation of a dual disk by gradual accretion of stars into disk orbits (e.g. ?). More recent work has also framed this bimodality as a consequence of discontinuous radial migration of stars in the disk (?).

However, such chemical structure can be replicated in part by invoking various Galactic chemical evolution models that do not rely on a ‘one-zone’ approximation (e.g. ????). For example, ? showed that a combination of GCE models with varying outflow mass loading parameters and inflow timescales (intended to represent enrichment histories at varying Galactocentric radii) could make a roughly bimodal  $[\alpha/\text{Fe}]$  distribution. The same models were shown to present a good explanation of the APOGEE  $[\alpha/\text{Fe}]\text{-}[\text{Fe}/\text{H}]$  plane by ?. A deeper understanding of the connection between spatial structure in  $[\alpha/\text{Fe}]$  and stellar age selected populations in the Milky Way is necessary to link these results.

In this paper, we present the first dissection of radially extended samples of Milky Way disk stars in age,  $[\text{Fe}/\text{H}]$  and  $[\alpha/\text{Fe}]$ . A strong correlation is observed between stellar age and  $[\alpha/\text{Fe}]$  in the solar vicinity (?). On the other hand, but also in the solar vicinity, no correlation is found between age and  $[\text{Fe}/\text{H}]$  (e.g. ??), which may be explained by the occurrence of radial migrations. Thickening of the Galactic disk has been invoked as a consequence of outward stellar radial migration (e.g. ?). However, ? argue that the effect is small and that such migration in fact only makes disks flare by a small amount. Similarly, ? measured the flaring profile of low  $[\alpha/\text{Fe}]$  stars to only slowly exponentially increase with Galactocentric radius, and suggest that radial migration is likely not a viable mechanism for forming thickened disk components. Flaring has also been shown to arise as a result of satellite infall, which can be a stronger flaring agent than migrations (e.g. ?). The understanding of flaring and its connection to the evolution of the Galactic disk is essential, but as yet incomplete. In this paper, we present new constraints on models of radial migration in the disk by studying its effects on the Milky Way’s mono-age stellar populations.

Many theoretical studies have attempted to understand the observed structure of mono-

abundance populations (MAPs) through the use of hydrodynamics and N-body simulations. Few reproduce the observed bimodality in  $[\alpha/\text{Fe}]$  at fixed  $[\text{Fe}/\text{H}]$ , and so an understanding of this has so far proved difficult. However, certain characteristics of the Milky Way  $[\alpha/\text{Fe}]$  distribution are beginning to emerge in the most recent cosmological simulations (?). Structurally, the mono-age populations of simulated galaxies show good agreement with the Milky Way (e.g. ???). More recent work has brought into question the applicability of MAPs as a proxy for mono-age populations (?), showing that, particularly at low  $[\alpha/\text{Fe}]$ , MAPs may have significant age spreads due to the differential nature of star formation in the disk. We show in this paper that the structures of mono-age and mono-abundance populations in the Milky Way disk differ, but present complementary insights into the temporal and chemical evolution processes in the disk.

Previous work has studied MAPs in the Milky Way by analysing samples of SEGUE G-dwarfs (???) and APOGEE red-clump (RC) giants (?). In this work we map the spatial distribution of mono-age, mono- $[\text{Fe}/\text{H}]$  populations at low and high  $[\alpha/\text{Fe}]$  using a catalogue containing  $[\text{Fe}/\text{H}]$  and  $[\alpha/\text{Fe}]$  from the APOGEE survey (?) and ages from ? for 31,244 red giant stars. We complement earlier work by adapting the method developed by ? for RC stars, to enable its application to the full red giant branch (RGB) sample from APOGEE. Stars in the RGB are better tracers of the underlying stellar population than their RC counterparts because of reduced uncertainties in the stellar evolution models, and because they are generally brighter, and so are observed at greater distances. On the other hand, this means that the method developed by ? must be adapted to account for the spread in absolute magnitude over the RGB (whereas RC stars can be considered as a near-standard candle). On the basis of these measurements, we establish the local mass-weighted age- $[\text{Fe}/\text{H}]$  distribution, showing the contributions from both low and high  $[\alpha/\text{Fe}]$  stellar populations.

In Section 1.2, we discuss the APOGEE data and the distance and age catalogues used for this work. Section 1.3 describes the stellar density fitting method, drawing greatly on work by ?. Specifically, we describe the generalities of the maximum likelihood fitting procedure and the calculation of the effective survey selection function for RGB

stars in Section 1.3.1, the adopted parametric stellar density model in Section 1.3.2, and the method for calculating stellar surface-mass densities in Section 1.3.3. We present the fits in Section 1.4, along with the calculated surface-mass density contributions for each mono-age, mono-[Fe/H] population. In Section 1.5 we compare our findings to those in the literature and discuss possible scenarios for the formation of the Milky Way’s disk in light of our findings. Section 1.6 summarises our results and conclusions.

## 1.2 Data

### 1.2.1 The APOGEE Catalogue

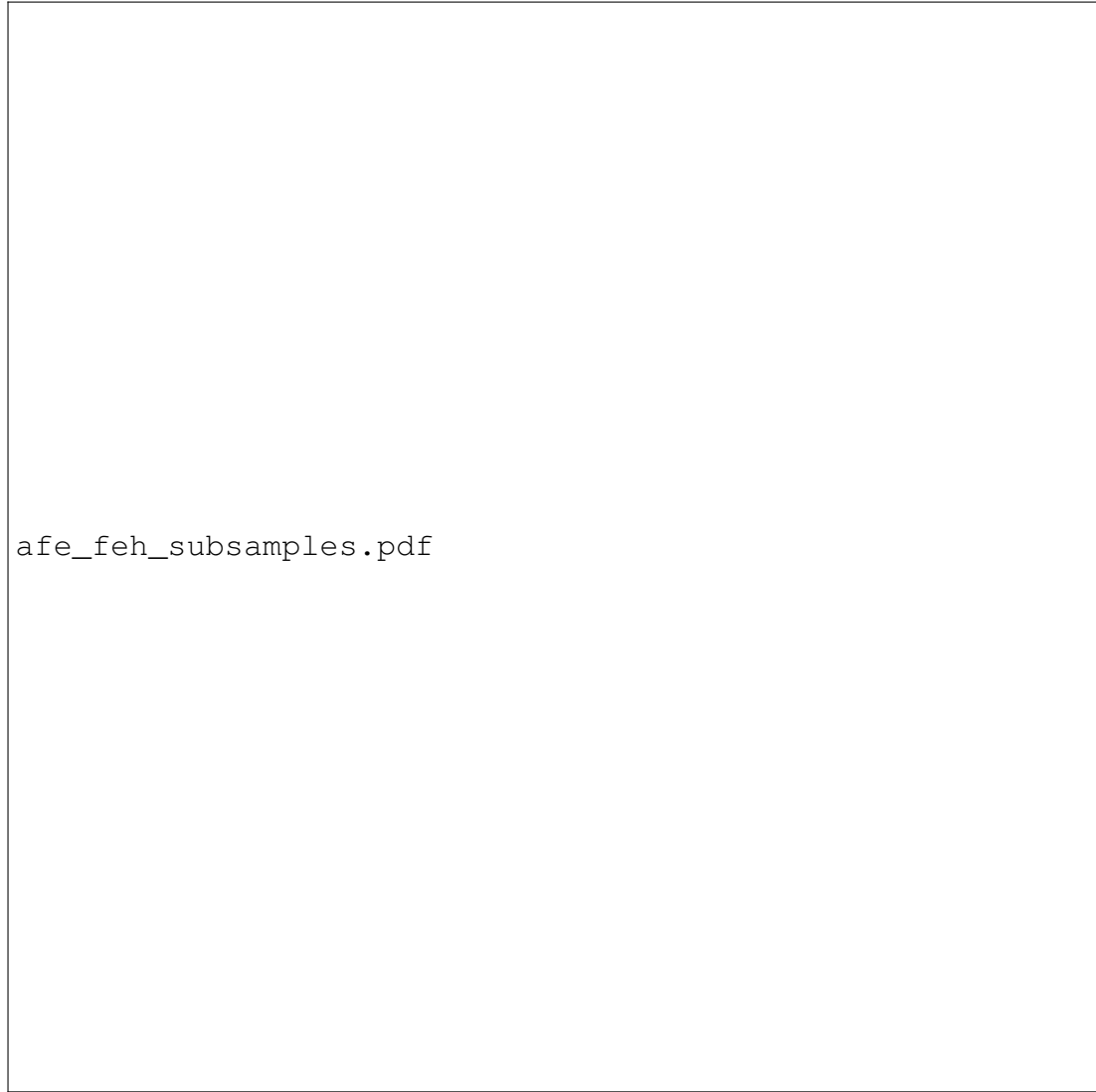
We use data from the twelfth data release (DR12, ?) of the SDSS-III APOGEE survey (?), a high signal-to-noise ratio ( $\text{SNR} > 100 \text{ pixel}^{-1}$ ), high resolution ( $R \sim 22,500$ ), spectroscopic survey of over 150,000 Milky Way stars in the near-infrared  $H$  Band ( $1.5 - 1.7\mu\text{m}$ ). Stars were observed during bright time with the APOGEE spectrograph (?) on the 2.5m Sloan Foundation Telescope (?) at Apache Point Observatory. Targets were selected in general from the 2MASS point-source catalog, employing a dereddened ( $J - K_S)_0 \geq 0.5$  colour cut (in the fields which are of interest here) in up to three apparent  $H$  magnitude bins (for a full description of the APOGEE target selection, see ?). Reddening corrections were determined for the colour cut via the Rayleigh-Jeans Colour Excess method (RJCE, ?). Corrections are found by applying the method to 2MASS (?) and mid-IR data from *Spitzer*-IRAC GLIMPSE-I, -II, and -3D (?) when available and from WISE (?) otherwise. For this work, we use distance moduli (which make use of the aforementioned reddening corrections) from the ? distance catalogue for DR12 (see Section 1.2.2).

All APOGEE data products employed in this paper are those output by the standard data reduction and analysis pipeline used for DR12. The data were processed (?), then fed into the APOGEE Stellar Parameters and Chemical Abundances Pipeline (ASPCAP, ?), which makes use of a specifically computed spectral library (?), calculated using a customised  $H$ -band line-list (?). Outputs from ASPCAP are analysed, cali-

brated and tabulated (?). The output  $[\alpha/\text{Fe}]$  and  $[\text{Fe}/\text{H}]$  abundances for DR12 have been shown to have a high degree of precision (at least between  $4500 \lesssim T_{\text{eff}} \lesssim 5200$  K), such that  $\sigma_{[\text{Fe}/\text{H}]} = 0.05$  dex and  $\sigma_{[\alpha/\text{Fe}]} = 0.02$  dex (?). We apply here the same external calibrations to  $[\alpha/\text{Fe}]$  and  $[\text{Fe}/\text{H}]$  as ?, constant offsets of -0.05 dex and -0.1 dex, respectively. We use the tabulated  $[\text{Fe}/\text{H}]$  value rather than the globally fit  $[\text{M}/\text{H}]$  which is included in the table.

We select stars from the DR12 catalogue which were targeted as part of the main disk survey (i.e. were subject to the  $(J - K_S)_0 \geq 0.5$  cut), have reliably measured abundances (i.e. no warning or error bits set in the ASPCAPFLAG field) and have a well defined distance modulus and age measurement (see Sections 1.2.2 and 1.2.3). We apply a secondary cut at  $1.8 < \log g < 3.0$  to restrict the sample to stars on the red giant branch (RGB), removing most contaminating dwarfs, and very evolved stars near the tip of the RGB. The high end of our  $\log g$  cut is more conservative than other studies in this regime, however we find this gives the best agreement between the data and stellar evolution models, without significantly reducing the sample size or introducing unwanted bias. These cuts give a final sample of 31,244 stars, spanning  $4200 \lesssim T_{\text{eff}} \lesssim 5050$  K for which the effective survey selection function can be reconstructed.

We further divide the sample into low and high  $[\alpha/\text{Fe}]$  sub-samples, as it has been shown in previous work that the two populations have quite different structural parameters (?), and as such it makes sense to fit their mono-age sub-populations separately. We separate visually the low and high  $[\alpha/\text{Fe}]$  populations, leaving a gap between the two samples of 0.05 dex in  $[\alpha/\text{Fe}]$  at each  $[\text{Fe}/\text{H}]$  (our separation is shown in Figure 1.1), to minimise contamination between the subsamples, particularly at the high  $[\text{Fe}/\text{H}]$  end, where the two populations partially overlap. The final density fits are performed on finer bins in age and  $[\text{Fe}/\text{H}]$ , which we define in Section 1.2.3. As the adopted separation in  $[\alpha/\text{Fe}]$  removes 6532 stars from the full count, when calculating the surface-mass density contributions from the stellar number counts in each age- $[\text{Fe}/\text{H}]$  bin, we remove the separation in  $[\alpha/\text{Fe}]$ , using the star counts as if the populations were separated along the midpoint of the division (as shown by the dot-dashed line in Figure 1.1).



afe\_feh\_subsamples.pdf

Figure 1.1: The full RGB sample in  $[\alpha/\text{Fe}]$ - $[\text{Fe}/\text{H}]$  space. The coloured regions show our division between low and high  $[\alpha/\text{Fe}]$  subsamples. At each  $[\text{Fe}/\text{H}]$  the division between the samples is  $[\alpha/\text{Fe}] = 0.05$  dex, roughly twice the mean uncertainty on  $[\alpha/\text{Fe}]$  abundance determinations in APOGEE DR12. The bimodality in  $[\alpha/\text{Fe}]$  at fixed  $[\text{Fe}/\text{H}]$  is visible across many  $[\text{Fe}/\text{H}]$ , and the lower number of stars in the high  $[\alpha/\text{Fe}]$  sample is clear from this plot.

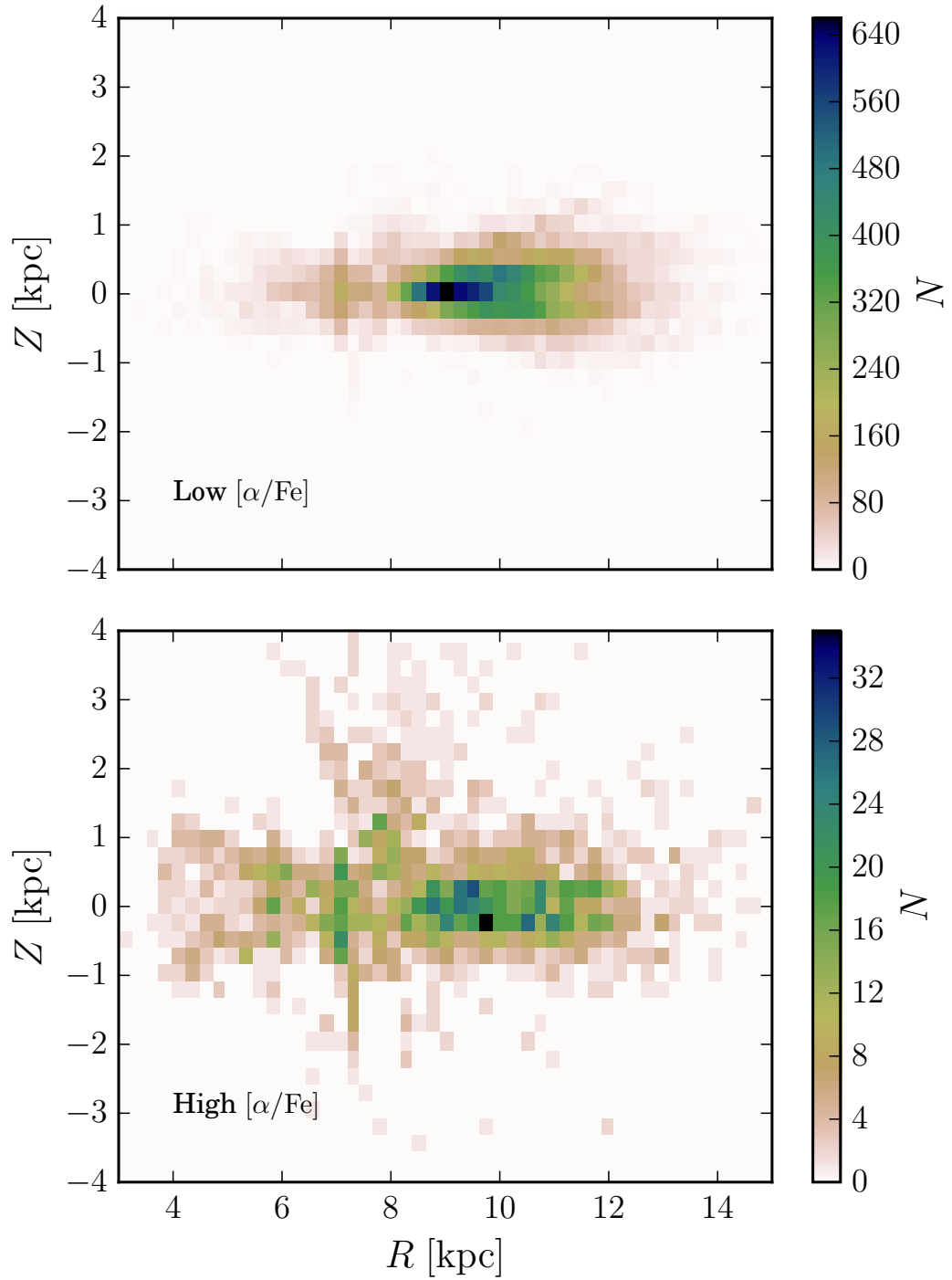


Figure 1.2: 2D histograms of the spatial distribution (in Galactocentric  $R$  and  $Z$ ) of the high and low [ $\alpha$ /Fe] subsamples shown in Figure 1.1. The high [ $\alpha$ /Fe] sample appears more diffuse and extended in height even before selection effects are accounted for. Readers should notice the different colour scale adopted for each panel, due to the much lower number of stars in the high [ $\alpha$ /Fe] sample.

Our method, discussed in Section 1.3, corrects for selection effects induced by interstellar extinction (in addition to the RJCE reddening corrections) using 3D dust maps for the Milky Way derived by ? for the inner disk plane, combined with those for a large majority of the APOGEE footprint by (?), adopting conversions  $A_H/A_{K_S} = 1.48$  and  $A_H/E(B-V) = 0.46$  (??). Fields with no dust data (of which there are  $\sim 10$ ) are removed from the analysis. ? discuss the relative merits and limitations of these dust maps as opposed to others which are available, and determine that this combination of dust maps provides the best density fits.

### 1.2.2 Distance estimates

We use distance estimates from ? (But see also ?, for further description). Distances are estimated by computing the probability distribution function (PDF) of all distance moduli to a given star using a Bayesian method applied to the spectroscopic and photometric parameters from the DR12 catalogue and the PARSEC isochrones (?). The distance estimates are found to have accuracy at the 15 – 20% level, upon comparison with cluster members of well known distance observed by APOGEE.

We use the median of the posterior PDF (which is given in the output catalogue) as the estimate for the distance modulus, and compute the Galactocentric cylindrical coordinates,  $R, \phi$  and  $Z$  for each star using the  $l, b$  coordinates provided in the APOGEE-DR12 catalogue. The spatial distribution of the two  $[\alpha/\text{Fe}]$  sub-samples is shown in Figure 1.2. We perform a simple cross match between our sample and the APOGEE red clump (RC) value added catalogue (VAC) (?) and plot the red-clump derived distance ( $D_{RC}$ ) against the estimate from ? ( $D_{MH}$ ) in Figure 1.3. The red clump catalogue has precise distance estimates, which can be determined due to the red-clump having a near constant absolute magnitude. The majority of the ? distances compare well to the RC distances, but there are notable differences. The ? distances can be underestimated by as much as 50%, and we find that  $\sim 20\%$  of our sample have distances underestimated by more than 10%. Our density fitting method is insensitive to uncertainties on the distances at these scales, as the scale of any variations in the density distribution

can be assumed to be far greater than the distance uncertainties.

Figure 1.3 also shows that there is a systematic offset between the RC and ? distances of the order  $\sim 5\%$  across the full range of distances. We find that adopting this offset as a correction to the distances makes little impact on the final results, merely broadening fitted density profiles slightly, spreading the star counts over a wider Galactocentric distance, meaning that the final stellar surface-mass density estimates are unchanged.

### 1.2.3 Age estimates

We use age estimates for APOGEE DR12 catalogued by ?, who derive an empirical model for the  $[C/N] - M_*$  relation using asteroseismic masses from *Kepler* and abundances from APOGEE for their overlapping samples (APOKASC ?). Masses are predicted for DR12 stars which meet quality and stellar parameter criteria outlined in ?, and ages are estimated from that mass using the PARSEC isochrones with the nearest metallicity to that of the given star. ? use this empirical relation to build a model which predicts mass and age as a function of  $[[M/H], [C/M], [N/M], [(C+N)/M], \log g, T_{\text{eff}}]$ . It is important to note here that ? derive a model and fit for the ages in DR12 using the uncalibrated, raw stellar parameters, found in the FPARAM arrays in the APOGEE catalogue. This is difficult to account for when using the age catalogue alongside the calibrated parameters, and must be borne in mind in future comparisons of this work with models and observational results. [id=TM]In addition to this, ? also mention that care should be taken when applying these ages to regions of the Milky Way where the chemical evolution may have been complex (e.g. the Bulge/Bar region). However, in their Figure 12, they compare the  $[C/N]$  ratio as a function of  $[M/H]$  in a sample of pre-dredge-up giants in the inner and outer disk, showing that the shapes of the distributions are similar. This suggests that differences in chemical evolution do not affect the  $[C/N]$ -age relation within a wide range of galactocentric distances. Therefore, the assumption that it is safe to adopt the ? ages over the extent of the disk covered by our sample is robust, regardless of the fact that they are trained on the *Kepler* sample, which is limited in its spatial extent.

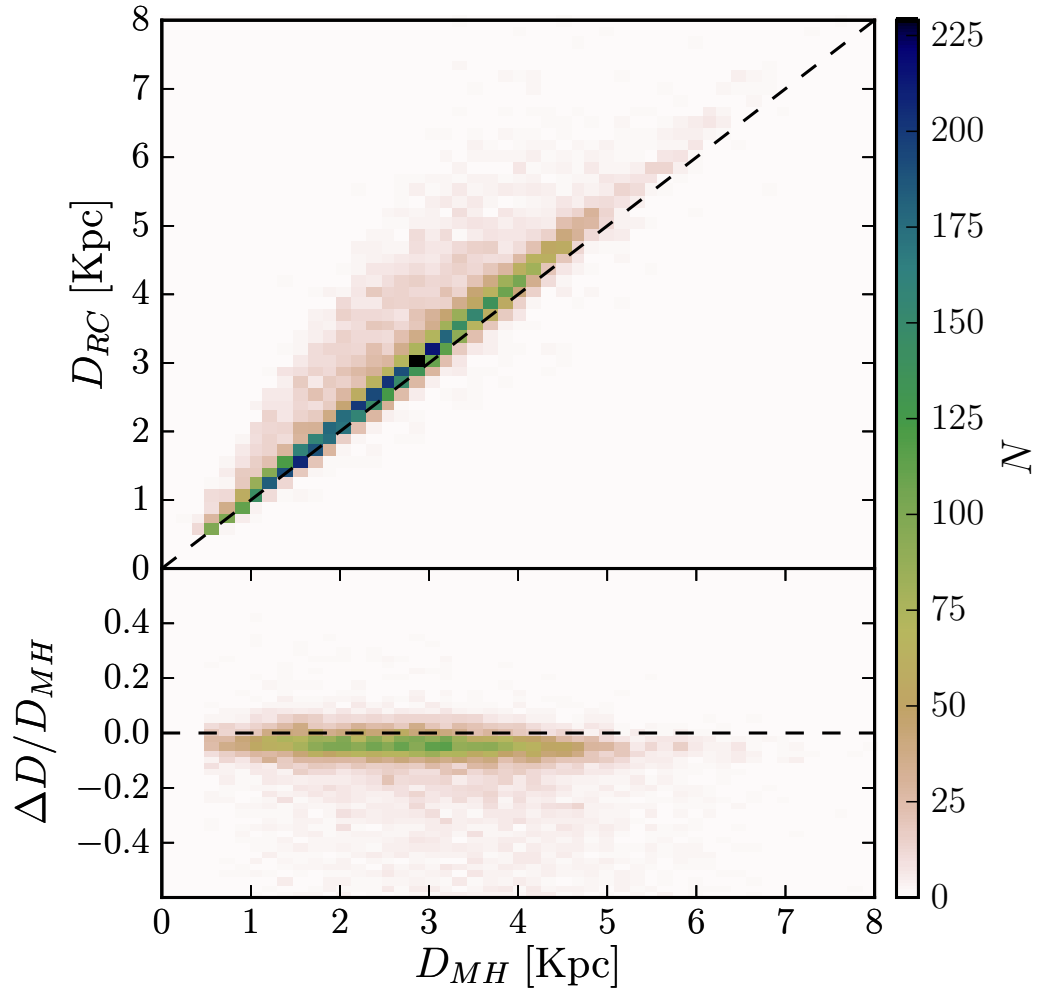


Figure 1.3: Comparison of APOGEE red clump catalogue (APOGEE-RC) distances  $D_{RC}$  with distances derived by ?,  $D_{MH}$ . The top panel directly compares the distances, where the bottom panel shows the difference as a fraction of  $D_{MH}$ , as a function of that distance. There are many stars with good agreement, but a distinct fraction of MH distances are underestimated compared to RC ( $\sim 20\%$  with distances underestimated by more than  $\sim 10\%$ ). As the variations in the density occur on scales which are, in general, far larger than these discrepancies, these are not problematic in our analysis. The two distance scales differ systematically by a factor of  $\sim 5\%$ , but we do not correct for this in the following discussion and it does not impact any of our results.

Although individual uncertainties on ages are not given in the catalogue, ? state that the model predicts ages with r.m.s errors of  $\sim 40\%$ . Although uncertainties are potentially very large at high age, our sample is binned with  $\Delta \text{age} = 2 \text{ Gyr}$  in order to gauge general trends with age. It should be understood that such trends are smoothed by the age uncertainties[id=TM], particularly at high age, and detailed comparisons to models should take the age uncertainty into account. [id=TM]We discuss the effect of these uncertainties on our recovered trends with age in Appendix 1.8, showing that our methodology can still reliably recover such trends, even though mixing between bins may be present in the data.

Figure 11 of ? shows that there is a significant bias in the ages returned by the model, such that ages are underpredicted at high age when compared to the training set. For this reason, we fit for and apply a correction to the catalogued ages before performing the density fitting. Using Table 1 of ?, we perform a non-parametric lowess fit to the predicted age–true age distribution. This fit is then used to derive age corrections as a function of predicted age. We show the fitted correction in Figure 1.4 in both predicted vs. true age space and also in  $\Delta \text{age}$  against the predicted age. The correction as a function of predicted age is then applied to each of the ages in the DR12 catalogue. In all further analysis, we refer only to the corrected ages. [id=TM]The main effect of this correction is to make the high-[ $\alpha/\text{Fe}$ ] stars older. Consequently, our surface-mass density estimates (presented in Section 1.4.3) become more conservative, as the mass contribution per star in older bins is lower (as discussed in Section 1.5.1). ? comment on the bias in the context that the ages returned for high [ $\alpha/\text{Fe}$ ] stars appear younger than previous estimates (from ???). Our correction brings these data more in line with those estimates.

It is also important to account for all other cuts made by ? on the stellar parameters in the APOGEE catalogue, outlined in full at the beginning of their Section 6.2. While we account for cuts in  $T_{\text{eff}}$  and  $\log g$  by applying the same cuts to the isochrone grid when calculating surface-mass density contributions, it is not possible to properly account for cuts made on the stellar abundances in this way. We find that 9,041 stars are removed from the 40,285 star catalogue (those with distances, after the  $\log g_{\text{cut}}$

mentioned above) by these abundance cuts, to give our final catalogue size of 31,244. This means that  $\sim 25\%$  of star counts are missing from the age catalogue, and therefore unaccounted for by our analysis. With no robust method for determining the age distribution of these missing stars, we are forced to make the assumption that these star counts can be added uniformly to each age-[Fe/H] bin. We make this correction by simply increasing the counts in each bin by 25% when calculating the surface-mass density. This correction simply increases the final surface-mass density values systematically by 25%.

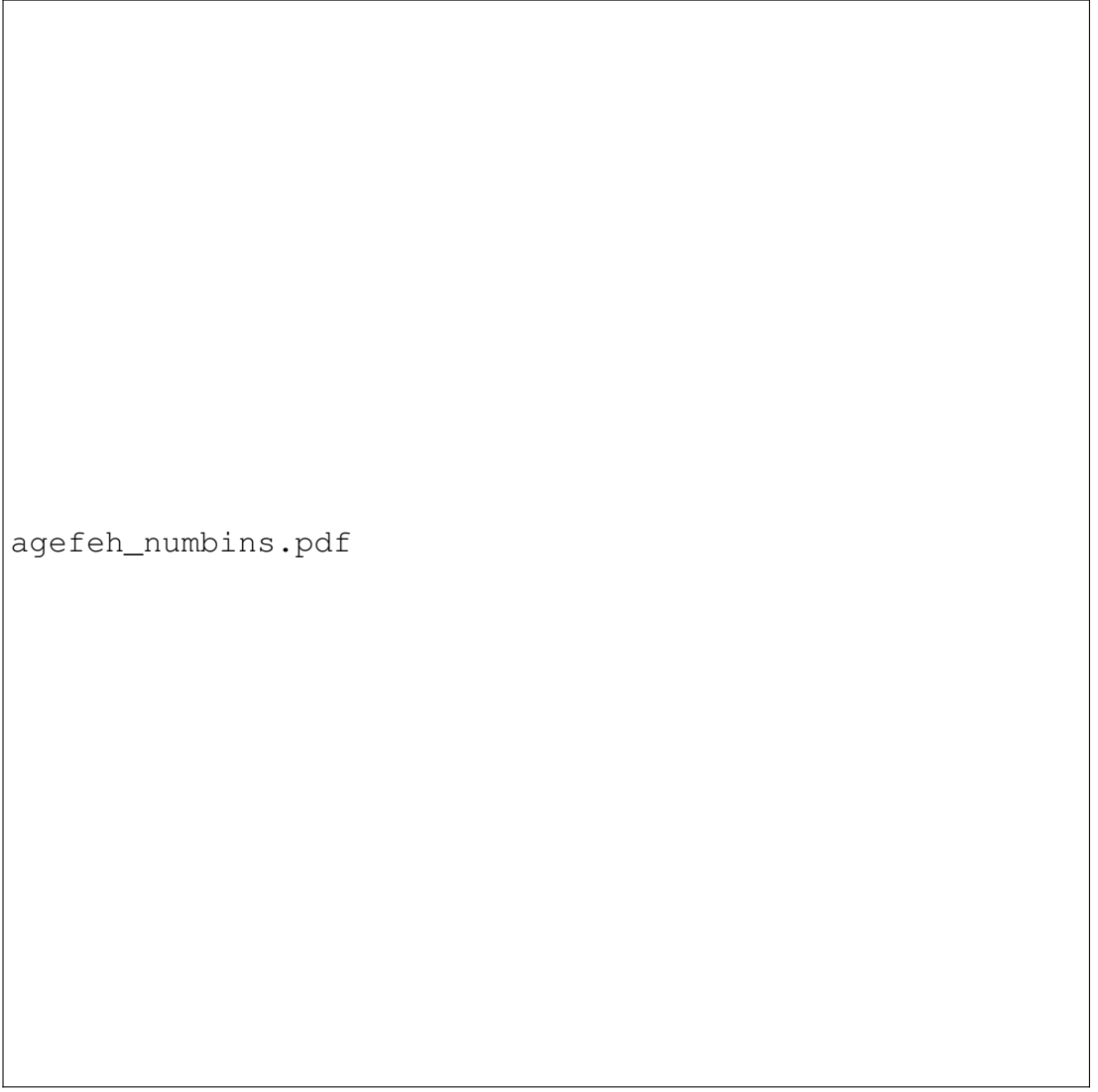
[id=TM]Another important consideration when using this set of ages regards stars whose chemical compositions are such that the ages fit from the model (after making the corrections) would be higher than 13 Gyr and left out of our analysis. As the age estimates are computed based on the surface parameters and abundances of the stars using a fitting function, many stars with strongly outlying abundances and parameters can be assigned ages which are greater than 13 Gyr. We find that the 3020 such stars (in the final sample) have an average [C/Fe] which is lower than the general sample, and an average [N/Fe] which is enhanced with respect to the stars with reliably measured ages. We also find that at fixed [Fe/H] and  $\log g$  these stars have warmer  $T_{\text{eff}}$ . While these properties are expected given their age measurements, we believe that there is a distinct possibility of some peculiarity of these stars. For example, if such stars were early AGB stars (having gone through the second dredge-up, reducing the surface C abundance, e.g. ?), which had been fit as RGB stars, their actual age may be considerably younger, and their counts missed in the younger bins (where mass contribution per star is higher). As the nature of these stars is debatable and a correction cannot be made confidently before carrying out the full analysis, we regard the missing counts from these stars as a contribution to the systematic error budget, which we discuss fully in Section 1.5.1.

We demonstrate the adopted binning in (age,[Fe/H]) space in Figure 1.5, showing also the number of stars which fall in each bin and the general distribution of stars in (age,[Fe/H]) space. There is a notable separation in age between the high and low  $[\alpha/\text{Fe}]$  subsamples.



agebias\_invsout.pdf

Figure 1.4: Asteroseismically determined ages from APOKASC against the [C/M] and [N/M] based ages from ?. The line gives the fitted correction for ages from ?, based on the values for the APOKASC training set, given in their Table 1. We fit the data using a non-parametric lowess fit. Before corrections, older ages are under-predicted, and young ages are overpredicted. The corrections mainly change the scaling of the ages, such that the high  $[\alpha/\text{Fe}]$  sample occupies an age range more in-line with the existing literature (e.g. ??)



agefeh\_numbins.pdf

Figure 1.5: 2D Histograms showing the raw number of stars in each ( $\text{age}, [\text{Fe}/\text{H}]$ ) bin of the low (*left*) and high (*right*)  $[\alpha/\text{Fe}]$  sub-samples. We draw the reader's attention to the difference in amplitude between the two sub-samples (and the associated difference in colour scale normalisation). Although the majority of bins are well sampled ( $\gtrsim 30$  stars), there are some greatly undersampled bins, for which well-defined fits are not possible.

## 1.3 Method

In this section we describe the method for fitting the underlying number density of stars in the Milky Way from APOGEE observations, which we represent here as  $\nu_*(X, Y, Z|\theta)$ , in units of stars kpc<sup>-3</sup>. The calculation of this quantity requires allowances to be made for the survey selection function, which is non-trivial due to the presence of inhomogeneous dust extinction along lines of sight observed by APOGEE, the target selection invoking different  $H$  magnitude limits, and the use of RGB stars as a tracer, which cannot be considered as standard candles. The quantity which we are ultimately interested in is the surface-mass density of stars at the solar radius,  $\Sigma_{R_0}$ , in units of M<sub>⊙</sub> pc<sup>-2</sup>, which we infer from the number of stars in the APOGEE sample as a function of position. We describe the method for this calculation in Section 1.3.3. Our methodology consists of an adaptation of that used by ?, employing a modified version of their publicly available code<sup>1</sup>. Although the general method is identical, we describe again the key components for clarity and completeness.

As some readers may find it unnecessary to read in full the details of the methodology (which are described in the following sections), we summarise the procedure as follows:

- We fit parametric density models to the APOGEE star counts using a maximum likelihood fitting procedure, based on the assumption that star counts are well modelled as an inhomogeneous Poisson point process. The density models which we assume throughout the paper are described by radially broken exponentials, with scale lengths  $h_{R,[\text{in},\text{out}]}$  either side of a break radius  $R_{\text{peak}}$  (where  $h_{R,\text{in}}$  denotes the scale length of the inner profile and vice versa), and a vertical distribution which is a single exponential with scale height  $h_Z$ , which is modified as a function of  $R$  by an exponential flaring term with scale length  $R_{\text{flare}}$ . We show that, in general, if the density is better fit by a single exponential, it is recovered as so by our procedure.

---

<sup>1</sup> Available at <https://github.com/jobovy/apogee-maps>

- We obtain a best fit density model for every bin in age and [Fe/H], at high and low  $[\alpha/\text{Fe}]$ . This best fit model is then used to initiate an MCMC sampling of the posterior PDF. We then use the median and standard deviation of one dimensional projections of the MCMC chain as our adopted parameter values and uncertainties.
- As the fitting procedure does not fit for the normalisation of the density  $N_{R_0}$ , the number surface density of stars at the solar radius in stars pc $^{-2}$ , we calculate this value by comparing the observed number of stars in each bin to that which would be observed in APOGEE for the fitted density model if  $N_{R_0} = 1$  star pc $^{-2}$ . We then convert  $N_{R_0}$  for each bin into the surface-mass density in visible stars at the solar radius  $\Sigma_{R_0}$  by converting the mass in RGB stars observed to the total mass using stellar evolution models.

Readers can then pick up the results in Section 1.4.

### 1.3.1 Density Fitting Procedure

We first fit for the number density of stars for each sub-population as defined by Figure 1.5. The following discussion describes the general procedure used for fitting density models with a generic set of parameters  $\theta$ . The actual stellar number density model adopted is discussed in Section 1.3.2. ??? have shown that the observed rate of stars as a function of position, magnitude, colour and metallicity can be modelled as an inhomogeneous Poisson point process. Stars are distributed in the space defined by  $O = [l, b, D, H, [J - K_S]_0, [\text{Fe}/\text{H}]]$  – position, magnitude, colour and metallicity – with an expected rate  $\lambda(O|\theta)$  (which has units of stars per arbitrary volume in O), parameterised by a set of parameters  $\theta$  (which are, in this particular case, the parameters describing an adopted density profile). This rate function is written fully as

$$\begin{aligned} \lambda(O|\theta) = \nu_*(X, Y, Z|\theta) &\times |J(X, Y, Z; l, b, D)| \\ &\times \rho(H, [J - K_S]_0, [\text{Fe}/\text{H}]|X, Y, Z) \times S(l, b, H) \end{aligned} \quad (1.1)$$

where  $\nu_*(X, Y, Z|\theta)$  is the quantity we aim to estimate, which is defined as the stellar number density in rectangular coordinates, in units of stars  $\text{kpc}^{-3}$ .  $|J(X, Y, Z; l, b, D)|$  is the Jacobian of the transformation from rectangular  $(X, Y, Z)$  to Galactic  $(l, b, D)$  coordinates and  $\rho(H, [J - K_S]_0, [\text{Fe}/\text{H}]|X, Y, Z)$  denotes the density of stars in magnitude, colour and metallicity space given a spatial position  $(X, Y, Z)$ , in units of stars per arbitrary volume in magnitude, colour and metallicity space.  $S(l, b, H)$  is the survey selection function (the fraction of stars observed in the survey) which includes dust extinction effects, which we discuss in the following. When expressed in this way, fitting the density model parameters  $\theta$  becomes a maximum likelihood problem.

The likelihood is a sum over all data-points considered in a given age-[Fe/H] bin, and gives the likelihood of the parameters  $\theta$  given the data. For this application, it is written as

$$\ln \mathcal{L}(\theta) = \sum_i \left[ \ln \nu_*(X_i, Y_i, Z_i|\theta) - \ln \int dO \lambda(O|\theta) \right] \quad (1.2)$$

where second term on the right hand side of the equation,  $\int dO \lambda(O|\theta)$ , describes the effective volume of the survey. We drop the other factors in the rate in Equation (1.1) in the argument of the logarithm, because the other factors do not depend on the model parameters  $\theta$ . The effective volume is independent of the data-point considered, and is an intrinsic property of the survey for a given  $\theta$ . It provides the normalisation for the rate likelihood, and is non-trivial to evaluate due to the presence of patchy dust extinction along lines of sight in the survey.

The effective volume is written generally as

$$\begin{aligned} \int dO \lambda(O|\theta) &= \sum_{\text{fields}} \Omega_f \int dD D^2 \nu_*([X, Y, Z](D, \text{field})|\theta) \\ &\quad \times \mathfrak{S}(\text{field}, D) \end{aligned} \quad (1.3)$$

which is a sum over all APOGEE fields, where  $\Omega_f$  is the solid angle of the field considered. The integrand  $\nu_*([X, Y, Z](D, \text{field})|\theta)$  is the density at each point along a line of sight, assumed to be constant over the angular size of the field.  $\mathfrak{S}(\text{field}, D)$  represents

the effective survey selection function, which is given by the integration of the survey selection function over the area of the field and is written, in this case, as

$$\mathfrak{S}(\text{field}, D) = \sum_k S(\text{field}, k) \int dM_H \frac{\Omega_k(H_{[\min, \max], k}, M_H, A_H[l, b, D], D)}{\Omega_f}. \quad (1.4)$$

This is a sum over the apparent magnitude bins,  $k$ , in the APOGEE target selection, with the integral representing the fractional area of the APOGEE field where stars are observable, given the distance modulus and extinction at a given position. The term describing this area is  $\Omega_k$ , which is the observable area of the field at a given distance and absolute magnitude, written as

$$\Omega_k(H_{[\min, \max], k}, M_H, A_H[l, b, D], D) = \Omega(H_{\min, k} - [M_H - \mu(D)] < A_H(l, b, D) < H_{\max, k} - [M_H - \mu(D)]) \quad (1.5)$$

where  $H_{[\min, \max], k}$  denotes the minimum and maximum  $H$  for an apparent magnitude bin  $k$  in the APOGEE target selection and  $\mu(D)$  is the distance modulus at  $D$ .  $A_H(l, b, D)$  is the  $H$  band extinction at a given position, which we obtain from the 3D dust maps described in Section 1.2.1. This area is integrated (in Equation (1.4)) over the full absolute  $H$ -band magnitude,  $M_H$ , distribution in an (age,[Fe/H]) bin. We find the  $M_H$  distribution for each (age,[Fe/H]) bin using the PARSEC isochrones (?) within that bin, weighted with a ? IMF. We apply the same cuts in  $\log g$  and  $(J - K_S)_0$  colour to the isochrone points as are imposed on the data, and perform a Monte Carlo integration using the resulting  $M_H$  distribution to evaluate the integral in Equation (1.4).  $S(\text{field}, k)$  in Equation (1.4) denotes the 'raw' APOGEE selection function, which gives the fraction of the stars in the photometric catalogue that were observed spectroscopically (see ?, for details). This number is constant within an apparent magnitude bin and within an APOGEE field, which is why  $S$  is cast as a function of field and magnitude bin in Equation (1.4). The values of  $S(\text{field}, k)$  (and  $\mathfrak{S}(\text{field}, D)$ ) are evaluated using

the `apogee` python package<sup>2</sup>.

We evaluate  $\mathfrak{S}(\text{field}, D)$  on a grid of distances for each APOGEE field for simple computation of  $\int dO\lambda(O|\theta)$ . We then optimise the likelihood function in Equation (1.2) for a given density model and data-set using a downhill-simplex algorithm, to obtain the best fitting set of parameters  $\theta$ . A Markov Chain Monte Carlo (MCMC) sampling of the posterior PDF is then initiated using this optimal solution. This is implemented with an affine-invariant ensemble MCMC sampler (??). All parameter values and associated uncertainties for individual (age,[Fe/H]) bins which are reported in the following sections represent the median and standard deviation  $\sigma$ , respectively, of one dimensional projections of the MCMC chain.

### 1.3.2 Adopted stellar number density models

It was shown in ? that density profiles of MAPs are well represented by axisymmetric profiles that can be written as

$$\nu_*(R, \phi, Z) = \Sigma(R)\zeta(Z|R) \quad \text{where } \int dZ\zeta(Z|R) = 1. \quad (1.6)$$

Furthermore, the exact form of the best fitting profile is that of a radially broken exponential, with a vertical profile that is an exponential with a scale height which varies exponentially with  $R$  (a flaring profile), such that

$$\ln \Sigma(R) \propto \begin{cases} -h_{R,\text{in}}^{-1}(R - R_0) & \text{where } R \leq R_{\text{peak}} \\ -h_{R,\text{out}}^{-1}(R - R_0) & \text{where } R > R_{\text{peak}} \end{cases} \quad (1.7)$$

and

$$\ln \zeta(Z|R) \propto h_Z^{-1} \exp(R_{\text{flare}}^{-1}[R - R_0])|Z| - \ln h_Z(R). \quad (1.8)$$

$R_0$  denotes the solar radius, which we assume here to be 8 kpc. This number only sets the radius at which the profiles are normalised, and so does not have any effect

---

<sup>2</sup>Available at <https://github.com/jobovy/apogee>

on the fitting procedure. We use the same general set of density profiles to describe the mono-age, mono-metallicity populations which are studied here. We bin in [Fe/H] to account for the observed [Fe/H] spread at fixed age (e.g. ?, and our Figure 1.5). ? also showed that when mock data were fit using the procedure in Section 1.3.1 and the density profile above, the input parameters were always recovered within acceptable uncertainty ranges. In particular, mock data generated from a single exponential profile was still recovered as such (i.e. with  $R_{\text{peak}} = 0$ ) even when fit assuming a broken exponential profile.

We also note here that our sample is not limited to stars which are members of any specific Galactic component, and as such, may include small numbers of halo stars in the very high  $[\alpha/\text{Fe}]$  and low [Fe/H] regimes. However, our fitting procedure is agnostic to these contaminants, which would only cause the fits to have larger uncertainty (from the MCMC exploration) about the best fit from the dominant population in a given bin.

### 1.3.3 Stellar surface-mass densities

We compute the surface-mass density in visible stars for each of our age and [Fe/H] populations using the method originally outlined in ?. As our fitting procedure does not fit for the normalisation of the density (we normalise to a surface density of 1 at  $R_0$ ), we first compute the normalisation  $N_{R_0}$ , which represents the number density of stars at the solar radius in units of stars pc<sup>-2</sup> in an (age,[Fe/H]) bin.  $N_{R_0}$  is given by the relation

$$N_{R_0} = \frac{N_{*,\text{observed}}}{\int dO\lambda(O|\theta)} \quad (1.9)$$

where  $N_{*,\text{observed}}$  is the number of stars observed in the survey for a given (age,[Fe/H]) and  $\int dO\lambda(O|\theta)$  is the usual definition of the effective volume (given by Equation (1.3)) for a given set of parameters  $\theta$ , found using the method in Section 1.3.1.

We find the contribution to stellar surface-mass density by first multiplying  $N_{R_0}$  by the average mass of a red giant star in the same range of age and [Fe/H], given the selection criteria on  $\log g$  given in Section 1.2.1 (which picks out the RGB) and  $(J - K_S)_0 \geq 0.5$

(given that we only use fields in which this cut was applied). We then correct this value to represent the total stellar population by dividing by the fractional contribution of the red giants to the total underlying population. These values are found using PARSEC isochrones (?), weighted with a Log-normal ? IMF, as described in the calculation of the effective volume in Section 1.3.1. This then leads us to a stellar surface-mass density  $\Sigma_{R_0}$  as a function of age and [Fe/H]. This conversion can be expressed as

$$\Sigma_{R_0}(\text{age}, [\text{Fe}/\text{H}]) = N_{R_0} \frac{\langle M_{\text{RGB}} \rangle(\text{age}, [\text{Fe}/\text{H}])}{\omega(\text{age}, [\text{Fe}/\text{H}])} \quad (1.10)$$

Where  $\langle M_{\text{RGB}} \rangle(\text{age}, [\text{Fe}/\text{H}])$  is the mean stellar mass in an (age,[Fe/H]) bin, and  $\omega(\text{age}, [\text{Fe}/\text{H}])$  is the fraction of stars in the total stellar population in an (age,[Fe/H]) bin which are within the  $\log g$  and  $(J - K_S)_0$  cuts in APOGEE. The stellar surface-mass density contributions of each bin can then be summed to give the total stellar surface-mass density at the solar radius  $\Sigma_{R_0,\text{tot}}$ .

Our final surface-mass density estimate is strongly dependent on the conversion factors in the above equations, the average RGB star mass,  $\langle M_{\text{RGB}} \rangle$ , and the fractional contribution from giants,  $\omega$ . We find that the average giant masses in our range of ages and [Fe/H] span  $0.9 \lesssim \langle M_{\text{RGB}} \rangle \lesssim 2.1 M_\odot$ . The most metal poor and oldest populations have the lowest average mass, and the youngest, most metal rich populations have the highest. The fractional contribution from giants in this regime ranges between  $0.002 \lesssim \omega \lesssim 0.02$ . The oldest and most metal poor populations have the least giants, whereas the youngest, metal rich populations have the most. These values appear to sit well with recent inventories of the solar neighbourhood, which suggest giants should make up of the order of a few percent of the mass (?). We discuss the potential systematics introduced by the use of stellar evolution models in Section 1.5.1.

## 1.4 Results

We now present results from the density fitting procedure, and the subsequent calculation of the surface-mass density contribution of each mono-age, mono-[Fe/H] popula-

tion in fig: numbins. Density fitting is performed on all populations, but we only display the fits for populations with  $> 30$  stars, as data below this level become too noisy to render reliable fits. Although the remaining fits can be noisy when star counts are near this limit, this is reflected in the error analysis arising from the MCMC exploration of the posterior PDF of the fitted parameters. We refer the reader to Appendix 1.7 for a comparison between the data and the fitted models for each mono-age, mono-[Fe/H] bin, and a qualitative discussion regarding the rationale behind the decision to discuss fits to only the broken exponential density profile.

#### 1.4.1 The radial profile of mono-age, mono-[Fe/H] populations

We first show the fits to the surface density in the low and high  $[\alpha/\text{Fe}]$  sub-samples in Figure 1.6. We display fits for all age and [Fe/H] bins with  $> 30$  stars. By shading the profiles by their surface-mass density contribution (as shown in Section 1.4.3), we intend to draw the eye to the profiles which contribute most to the mass of the Milky Way disk. We defer a discussion of the individual mass contributions of each bin to Section 1.4.3, concentrating in this section on trends in the shapes of the density profiles.

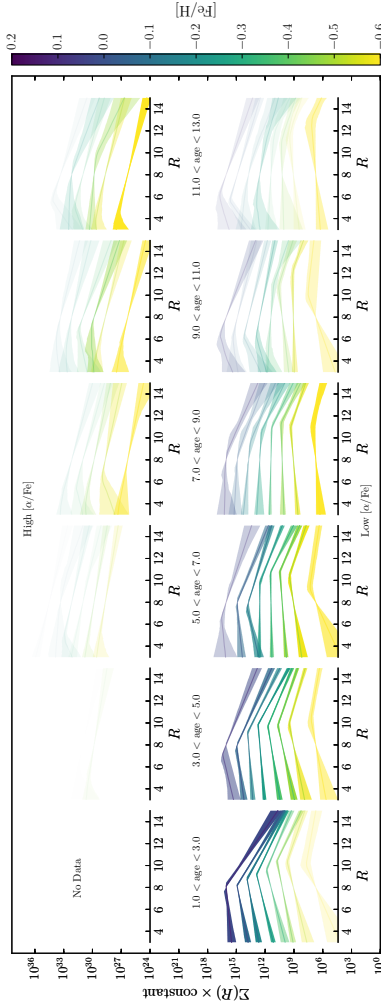


Figure 1.6: The fitted surface density profiles for the high  $[\alpha/\text{Fe}]$  (top) and low  $[\alpha/\text{Fe}]$  (bottom) sub-samples as a function of  $[\text{Fe}/\text{H}]$  (colour) and age (increasing from left to right). The coloured bands represent the 95% uncertainty range. Only profiles for bins containing  $> 30$  stars are shown. The profiles have a transparency according to the surface-mass density calculated for each bin in Section 1.4.3, normalised separately for each row (i.e. in each  $[\text{Fe}/\text{H}]$  bin), to draw the eye to those profiles which contribute most to the Milky Way surface-mass density. High  $[\alpha/\text{Fe}]$  profiles are described well by a single exponential, whereas young, low  $[\alpha/\text{Fe}]$  profiles are broken exponentials with a peak density which varies in radius in the disk.

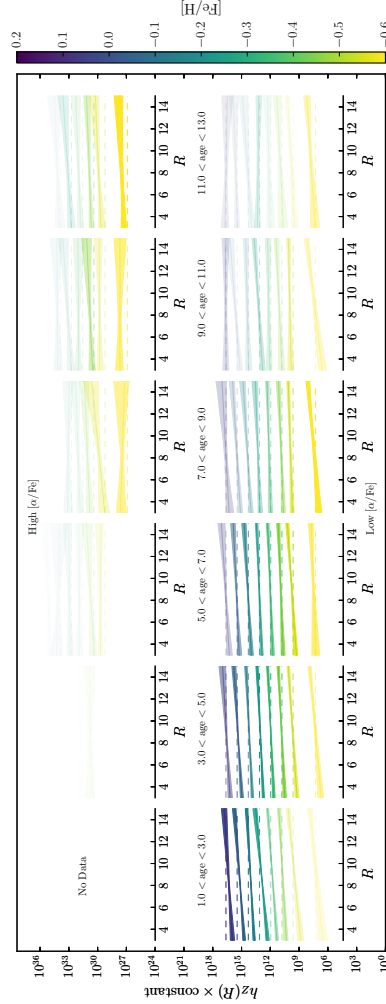


Figure 1.7: Vertical profiles for the high  $[\alpha/\text{Fe}]$  (top) and low  $[\alpha/\text{Fe}]$  (bottom) sub-samples as a function of  $[\text{Fe}/\text{H}]$  (colour) and age (increasing from left to right). The coloured bands represent the 95% uncertainty range. Only profiles for bins with  $> 30$  stars are shown, with profiles shaded according to their surface-mass density contributions (discussed in Section 1.4.3). The dashed lines represent  $h_Z = 0.3$  kpc, for reference.

Although fit with the broken exponential, high  $[\alpha/\text{Fe}]$  profiles are generally better described by near-single exponentials, either showing no break in the radial range, or being fit by a profile with a break at low significance (i.e. a single line could be drawn through the coloured band). Many of the outer profiles (after  $R_{\text{peak}}$ ) in the high  $[\alpha/\text{Fe}]$  sub-sample appear to have a similar slope, suggesting that they may all be represented by the same exponential. The mean outer scale length for the high  $[\alpha/\text{Fe}]$  populations is  $h_{R,\text{out}} = 1.9 \pm 0.1$  kpc. The picture is noticeably different in the low  $[\alpha/\text{Fe}]$  sub-sample, with profiles showing clear breaks, at well defined radii. Any trends in break radius in this regime are determined with high significance. Low  $[\alpha/\text{Fe}]$  profiles have a density which increases with radius out to the break radius, and declines outward of this radius. We do not constrain the fits to behave in this way, and this indicates that mono-age, mono-[Fe/H] populations at low [Fe/H] are shaped approximately as donut-like annuli. The variation of the break radius then represents the moving peak of stellar density as a function of age and [Fe/H]. Concentrating on the bins youngest bin ( $1 < \text{age} < 3$  Gyr), the break radius is a declining function of metallicity, moving between  $R_{\text{peak}} = 10$  kpc at  $-0.6 < [\text{Fe}/\text{H}] < -0.5$  dex down to  $R_{\text{peak}} < 8$  kpc at  $0.1 < [\text{Fe}/\text{H}] < 0.2$  dex. This trend is also present in older bins but with decreased amplitude. In a fixed [Fe/H] bin,  $R_{\text{peak}}$  appears to remain roughly constant (within  $\sim 1$  kpc) at ages between 1 and 6 Gyr. At ages older than this  $R_{\text{peak}}$  varies in unexpected ways, but there is much less mass contribution from these populations, and we attribute much of this behaviour to noise from the narrow age bins.

On the other hand, the low  $[\alpha/\text{Fe}]$  profiles change *shape* (either side of  $R_{\text{peak}}$ ) with age in a fixed [Fe/H] bin. The youngest populations show a sharp peak, with a steep increase and decline either side of  $R_{\text{peak}}$ . As populations grow older, the profile broadens significantly, becoming almost flat in the lowest [Fe/H] bins. We show this behaviour by finding the inverse of the difference between the inverse outer and inner scale length<sup>3</sup>, such that a low value denotes a sharper peak, whereas a broader profile has a higher value. We show how this value changes with age for the low  $[\alpha/\text{Fe}]$

---

<sup>3</sup>Taking a ratio of the sum of the density at fixed  $\Delta R$  either side of  $R_{\text{peak}}$  to that at  $R_{\text{peak}}$  would give some measure of width. Then, assuming  $\Delta R \ll h_{R,[\text{in},\text{out}]}$ , a Taylor expansion of this ratio  $\sim \Delta R(h_{R,\text{out}}^{-1} - h_{R,\text{in}}^{-1})$ . We then plot the inverse of this factor such that it increases for broader profiles.

populations in Figure 1.8. The peak is sharpest in the younger populations, and becomes broader with age. Old populations have artificially sharpened peaks in this diagnostic due to their being better described by single exponentials. Notably also, in Figure 1.6, at low [Fe/H] the inner profiles flatten faster than the outer profile, whereas the higher [Fe/H] populations show the opposite behaviour. For example, in the  $-0.3 < [\text{Fe}/\text{H}] < -0.2$  dex bin, the outer profile appears to remain roughly constant in slope between 1 and 6 Gyr, while the inner profile flattens significantly. The opposite is seen in the  $0.1 < [\text{Fe}/\text{H}] < 0.2$  dex bin, where the outer profile flattens considerably with age.

### 1.4.2 The vertical profile of the disk

We now examine the variation of  $h_Z$  as a function of radius in mono-age, mono-[Fe/H] populations. Because mono-age, mono-[Fe/H] populations are well described by a single scale height, which is modified by a flaring term  $R_{\text{flare}}$ , this means that  $h_Z$  is weakly dependent on  $R$  for profiles which flare. We show vertical profiles for age-[Fe/H] bins with  $> 30$  stars in Figure 1.7, adopting the same shading as Figure 1.6 to draw the eye to the profiles with greater mass contribution, and adding a dashed line representing 0.3 kpc for reference.

Figure 1.7 suggests that the disk is thicker as traced by older populations. All [Fe/H] bins show a thickening as age increases. This is clear in the left panel of Figure 1.9, which shows the surface-mass density weighted mean variation of  $h_Z$  with age. The mean  $h_Z$  spans the range between 0.8 and 0.2 kpc. The high  $[\alpha/\text{Fe}]$  populations show a bump in the mean  $h_Z$  at 8 Gyr, but  $h_Z$  generally increases with age, similarly to the low  $[\alpha/\text{Fe}]$  populations. The shapes of the profiles of the youngest populations in Figure 1.7 in the low  $[\alpha/\text{Fe}]$  subsample show little variation with [Fe/H], and this trend generally continues to older ages. This is also reflected in the low uncertainties associated with the blue points in the left panel of Figure 1.9.

The high  $[\alpha/\text{Fe}]$  profiles are generally flat, indicating that these populations show little flaring. By multiplying together the PDFs of the posterior distribution of fits to  $R_{\text{flare}}$ ,

we determine that the high  $[\alpha/\text{Fe}]$  populations have an average  $R_{\text{flare}}^{-1} = -0.06 \pm 0.02$ . The low alpha populations flare more strongly, with an average  $R_{\text{flare}}^{-1} = -0.12 \pm 0.01$ . There is, however, some variation in the flaring as a function of age, so it may not be sensible to ascribe a single  $R_{\text{flare}}^{-1}$  to all the populations. We show the variation of  $R_{\text{flare}}^{-1}$  with age in the right panel of Figure 1.9, showing  $R_{\text{flare}}^{-1}$  rather than  $R_{\text{flare}}$  so that values close to 0 are represented properly. The surface-mass density weighted mean  $R_{\text{flare}}^{-1}$  of the low  $[\alpha/\text{Fe}]$  populations increases as a function of age, meaning that the most flared populations are the youngest. The behaviour appears opposite for the high  $[\alpha/\text{Fe}]$  populations, whose mean  $R_{\text{flare}}^{-1}$  seems to decrease with age, but this is determined with low significance as  $R_{\text{flare}}^{-1}$  measurements are noisier for these populations.

### 1.4.3 The mass contribution of mono-age, mono-[Fe/H] populations

We now present the results from the calculation of the surface-mass density at the solar radius using the method described in Section 1.3.3. We compute surface-mass density  $\Sigma_{R_0}$  estimates for each age-[Fe/H] bin, for the high and low  $[\alpha/\text{Fe}]$  samples. When quoting the surface-mass densities, we also quote estimates of the systematic uncertainties. We evaluate the sources of these uncertainties in Section 1.5.1.

We combine the mass contributions of the high and low  $[\alpha/\text{Fe}]$  mono-age, mono-[Fe/H] populations, and plot the estimates as a function of age and [Fe/H] in Figure 1.10. This figure essentially represents the *mass-weighted* age-[Fe/H] distribution at the solar radius, that is, the probability distribution for age and [Fe/H] for a randomly selected mass element. The distribution varies smoothly with no sharp peaks, and the surface-mass density increases linearly with both age and [Fe/H], peaking at  $1 < \text{age} < 3$  Gyr,  $0.0 < [\text{Fe}/\text{H}] < 0.1$  dex. The mass increases more smoothly with [Fe/H] than with age, but there is little mass in the highest [Fe/H] bin, creating a ridge in the marginalised distribution. The marginalised distributions as a function of age and [Fe/H] show no sign of bimodality, and there is little sign of a bimodality in age at fixed [Fe/H]. [id=TM]It should be mentioned again here that the age uncertainties

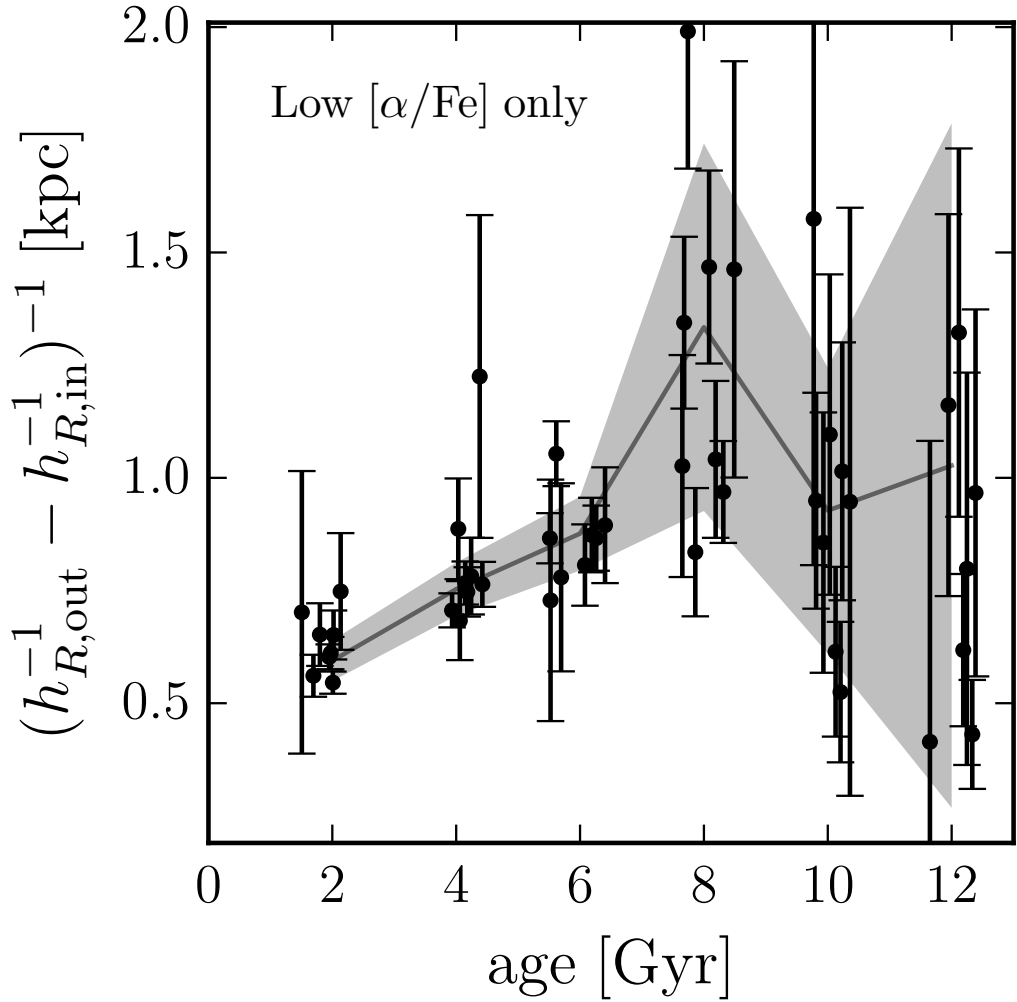


Figure 1.8: The profile width  $(h_{R,\text{out}}^{-1} - h_{R,\text{in}}^{-1})^{-1}$  against age for the low  $[\alpha/\text{Fe}]$  populations (this diagnostic is irrelevant for the high  $[\alpha/\text{Fe}]$  populations, which are generally fit by single exponentials). We add a small random jitter to the central age of each age bin, to make individual points and their uncertainty clearer. The relations and coloured band shows the running surface-mass density weighted mean and standard deviation in the age bins. The profile width increases with age. A higher value of this diagnostic suggests a broader surface density profile, showing that older populations are flatter and broader around the peak density.

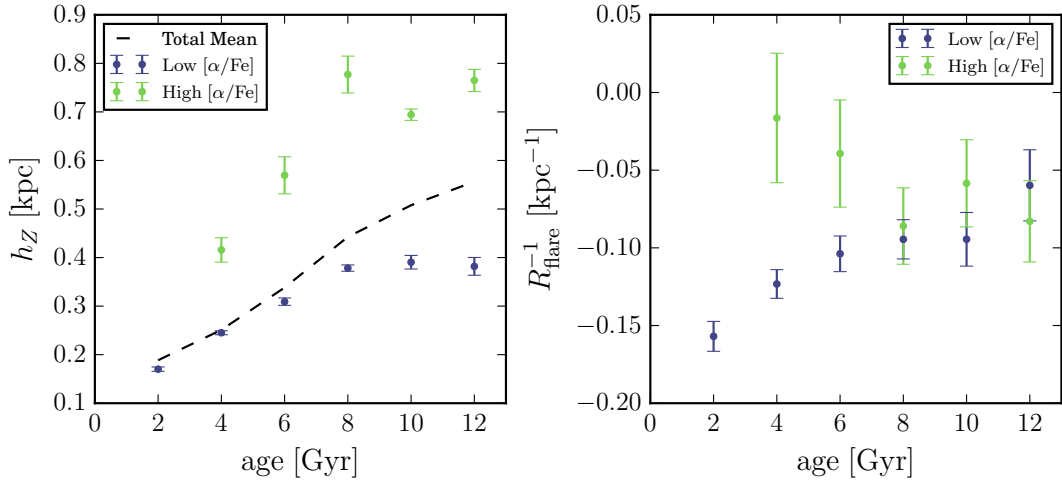


Figure 1.9: Mean  $h_Z$  at  $R_0$  (left) and  $R_{\text{flare}}^{-1}$  (right) against age. The mean value in each age bin is calculated by multiplying together the posterior PDFs of the density fits. The panels show both the low (purple) and high (green)  $[\alpha/\text{Fe}]$  populations. The left panel shows the total surface-mass density weighted mean as a dashed line, which demonstrates that the vertical distribution of the high  $[\alpha/\text{Fe}]$  population is only important at the solar radius at old ages due to its low surface-mass density contribution.  $h_Z$  increases with age for both low and high  $[\alpha/\text{Fe}]$  populations.  $R_{\text{flare}}^{-1}$  behaves similarly for the low  $[\alpha/\text{Fe}]$  population, meaning flaring decreases with age, but the high  $[\alpha/\text{Fe}]$  population shows an opposite behaviour.

may be larger than the bin width, particularly in older bins, which would cause an artificial blurring of a density edge in the distribution along the age axis. Therefore, we cannot presently determine to high significance that there are no discontinuities in this distribution.

An alternative way to look at the surface-mass density distributions is to retain the division in  $[\alpha/\text{Fe}]$ . We find that the high  $[\alpha/\text{Fe}]$  populations contribute  $\Sigma_{R_0, \text{tot}} = 3.0^{+0.4}_{-0.5}(\text{stat.})^{+0.6}_{-0.6}(\text{syst.}) \text{ M}_\odot \text{ pc}^{-2}$  to the total surface-mass density at the solar radius, whereas the low  $[\alpha/\text{Fe}]$  populations contribute  $\Sigma_{R_0, \text{tot}} = 17.1^{+2.0}_{-2.4}(\text{stat.})^{+4.4}_{-1.9}(\text{syst.}) \text{ M}_\odot \text{ pc}^{-2}$ , giving a total surface-mass density in stars at  $R_0$  of  $\Sigma_{R_0, \text{tot}} = 20.0^{+2.4}_{-2.9}(\text{stat.})^{+5.0}_{-2.4}(\text{syst.}) \text{ M}_\odot \text{ pc}^{-2}$ . We plot the individual surface-mass contributions for the separated low and high  $[\alpha/\text{Fe}]$  populations in Figure 1.11, adopting different color scales in each panel, to highlight the behaviour of the high  $[\alpha/\text{Fe}]$  populations, which contribute little mass in comparison to the low  $[\alpha/\text{Fe}]$ . The low  $[\alpha/\text{Fe}]$  mass is mostly concentrated at young age and towards higher  $[\text{Fe}/\text{H}]$ , although there is mass even at the oldest ages. The high  $[\alpha/\text{Fe}]$  mass is concentrated towards older ages, but interestingly the distribution extends to

high [Fe/H], and we detect mass at some [Fe/H] in every age bin, but at much lower levels. The tails of the distributions of the low and high [ $\alpha/\text{Fe}$ ] populations overlap somewhat in age-[Fe/H] space, around 6 Gyr ago, and there is a hint of a sequence extending from old, low [Fe/H] and high [ $\alpha/\text{Fe}$ ] populations, to young, high [Fe/H] and low [ $\alpha/\text{Fe}$ ] populations, which is somewhat visible in the combined histogram. There is no clear bimodality in age at fixed [Fe/H] in the combined histogram, owing to the very low mass contribution of the old, high [ $\alpha/\text{Fe}$ ] populations.

We have established that the vertical spatial distributions of mono-age, mono-[Fe/H] populations are well described by single exponentials with characteristic  $h_Z$ . Next, we use this information to generate the mass-weighted distribution of  $h_Z$ , which is representative of the probability distribution function for  $h_Z$ ,  $p(h_Z)$ . For a random stellar mass element, this function gives the probability density for the  $h_Z$  of the component to which it belongs. We show this relation in Figure 1.12, where coloured points represent the individual density contributions of mono-age, mono-[Fe/H] populations, and the coloured histograms their co-addition within  $\sim 0.1$  kpc wide bins in  $h_Z$  for the low and high [ $\alpha/\text{Fe}$ ] populations (purple and green, respectively). The dashed histogram represents the resulting total  $p(h_Z)$ . Scatter points are coloured by the age of the population they represent. The total distribution is smooth, resulting from the superposition of the low and high [ $\alpha/\text{Fe}$ ] distributions, which overlap significantly. The total  $\Sigma_{R_0}$  (dashed histogram) declines exponentially with  $h_Z$ , and is unimodal with no gaps. The trends of both  $h_Z$  and  $\Sigma_{R_0}$  with age seen in Figures 1.8 and 1.10 are recovered here, although it is surprising that the trend of  $h_Z$  with age at the high  $h_Z$  end does not appear as obvious here.

We can also now mass-weight and combine the fitted density profiles to attain the surface-mass density profile of the Milky Way as a function of age, [Fe/H] and [ $\alpha/\text{Fe}$ ]. The resulting profiles are displayed in Figure 1.13. The different nature of the low and high [ $\alpha/\text{Fe}$ ] populations in terms of spatial structure is clear here, with the low [ $\alpha/\text{Fe}$ ] profile having a clear break between 8 and 10 kpc, and the high [ $\alpha/\text{Fe}$ ] declining exponentially with  $R$ . It is interesting to note that extrapolation by eye of the high and low [ $\alpha/\text{Fe}$ ] profiles to low  $R$  would result in the high [ $\alpha/\text{Fe}$ ] population becoming domi-

nant over the low. The total profile appears roughly flat out to  $\sim 10$  kpc. However, we *strongly* emphasize that this is not determined to high significance, as even when only the uncertainties from the fitting procedure are included, one could describe the profile as exponentially declining with  $R$  within  $R < R_0$ . The inclusion of the other sources of uncertainty on the surface-mass density estimates would further decrease the significance of the apparent flattening. For example, the systematic uncertainties (discussed in Section 1.5.1) act to increase the fraction of surface-mass density contributed by the high  $[\alpha/\text{Fe}]$  populations, which would only *increase* the slope of the inner exponential. Using dynamical tracers, ? find that the surface density should decline exponentially with  $R$ , so it seems logical to assume that the inner profile should not be increasing with  $R$ .

As a function of age, the peak in the surface-mass density visible in the youngest population becomes less prominent, and the profile becomes a roughly single exponential at the oldest ages (i.e., it monotonically decreases with  $R$ ). The behaviour with  $[\text{Fe}/\text{H}]$  is more complex, but the variation of the peak radius with  $[\text{Fe}/\text{H}]$  is obvious, and the turnover in the total profile at  $\sim 10$  kpc appears to be a result of the outermost breaks.

## 1.5 Discussion

In the above analysis, we have, for the first time, determined the detailed structure of the Milky Way's disk as a function of stellar age and  $[\text{Fe}/\text{H}]$ . In our method, we have drawn heavily from previous dissections of the disk into its mono-abundance constituents (MAPs; ??), and so use these previous findings as a benchmark with which to compare these results. We also show that our results are also broadly consistent with other measurements, whilst shedding new light onto the problem of the formation of the Milky Way disk.

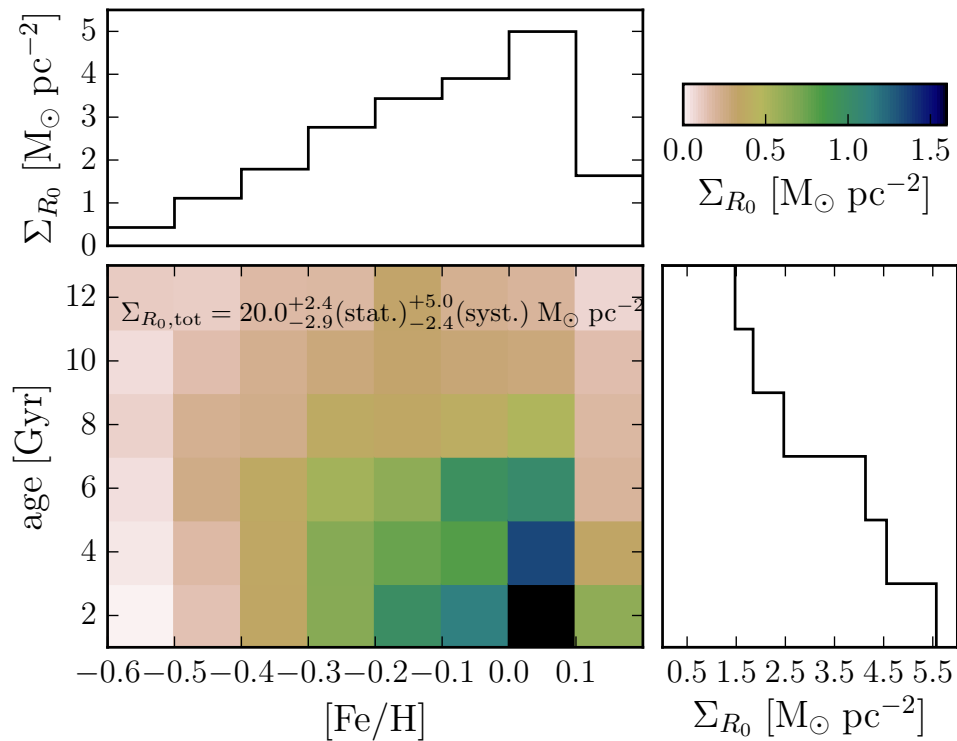


Figure 1.10: The surface-mass density contribution of mono-age, mono-[Fe/H] populations at  $R_0$  (where low and high  $[\alpha/\text{Fe}]$  are combined). The total contribution  $\Sigma_{R_0, \text{tot}}$  is displayed at the top of the main panel. The colour scale is linear and spans the surface-mass density range between  $0 < \Sigma_{R_0} < 1.5 M_\odot \text{ pc}^{-2}$ . The marginalised distributions along each axis are shown above and to the right. The mass at the solar radius increases monotonically with both age and [Fe/H].

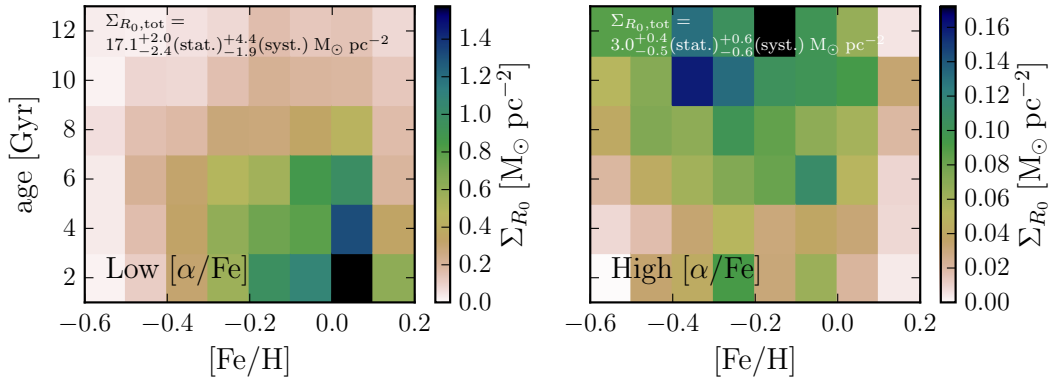


Figure 1.11: The surface-mass density contributions of the low (*left*) and high (*right*)  $[\alpha/\text{Fe}]$  sub-samples. The total contributions  $\Sigma_{R_0, \text{tot}}$  are displayed at the top of each panel. We draw the attention of the reader to the difference in colour scale between the high and low  $[\alpha/\text{Fe}]$  panels, which differs by an order of magnitude, and is adopted to better show the behaviour in the high  $[\alpha/\text{Fe}]$  sample. The low  $[\alpha/\text{Fe}]$  sub-sample has mass at all ages and  $[\text{Fe}/\text{H}]$  but is concentrated mostly at young ages. The high  $[\alpha/\text{Fe}]$  sub-sample contributes far less mass and is concentrated at old age.

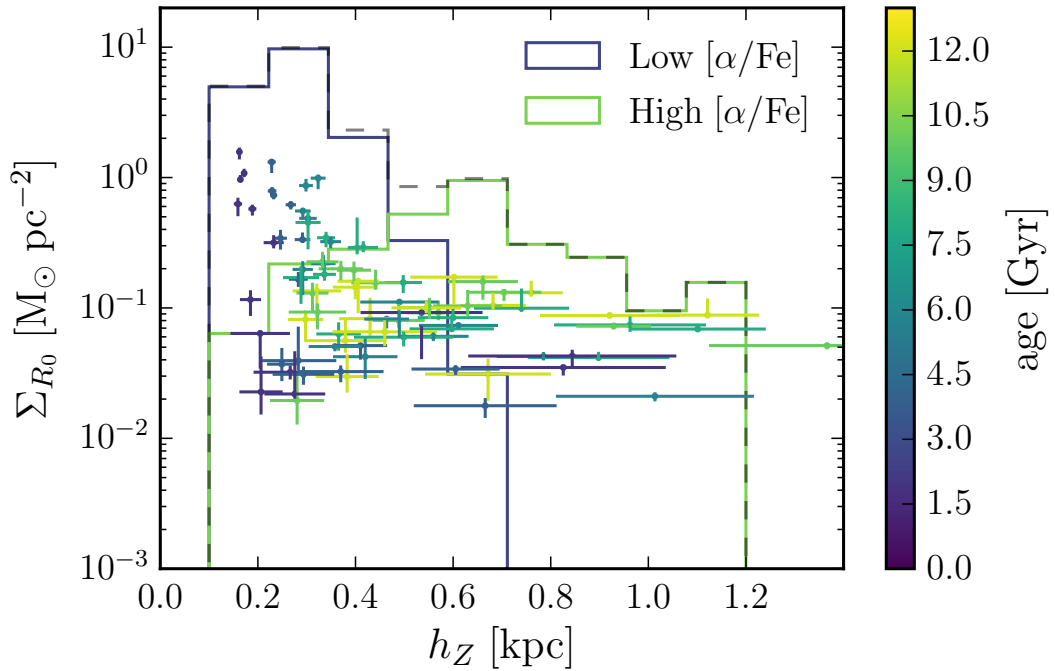


Figure 1.12: The mass weighted vertical scale height  $h_Z$  distribution. The individual points represent the  $h_Z$  and  $\Sigma_{R_0}$  for each mono-age, mono- $[\text{Fe}/\text{H}]$  population. We colour the points, which represent both the low and high  $[\alpha/\text{Fe}]$  populations, by the central age of the mono-age, mono- $[\text{Fe}/\text{H}]$  bin that they represent. The coloured histograms represent the  $h_Z$  distributions for the low and high  $[\alpha/\text{Fe}]$  populations from the sum of the individual contributions. The dashed histogram represents the total distribution. The total distribution smoothly decreases with  $h_Z$ , with no hints of bimodality.

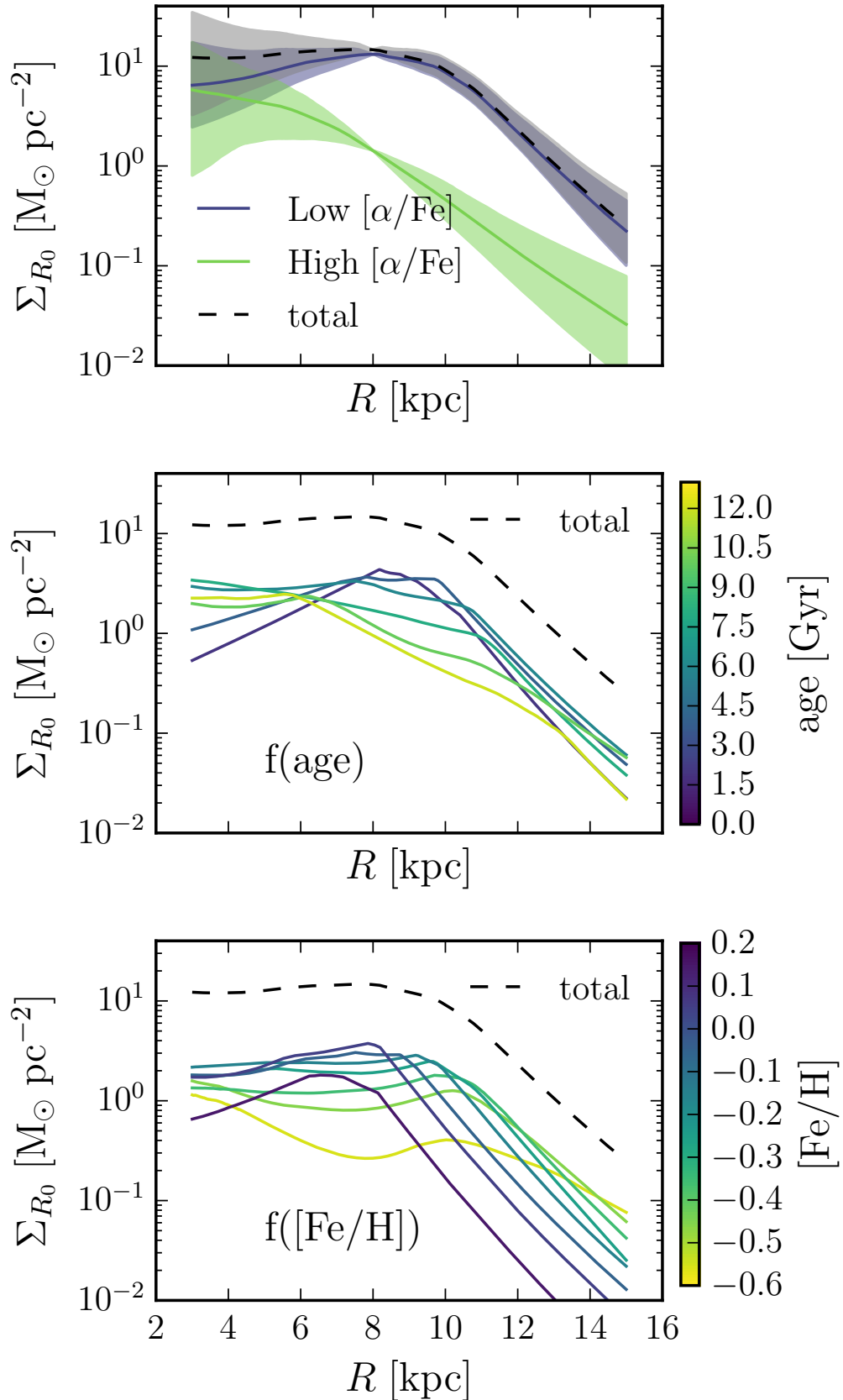


Figure 1.13: The radial surface-mass density profile of the Milky Way, as a function of [α/Fe] (top), age (middle) and [Fe/H] (bottom). The profiles are the result of a mass-weighted combination of the fitted density profiles along different axes in age-[Fe/H] space and (in the top panel) for the combined low and high [α/Fe] populations. We show the combined uncertainties for the total profile, which include both the individual uncertainties and correlations between the different profiles. We also include the individual profiles for the low and high [α/Fe] populations. The radial profile is shown for the innermost 16 kpc of the Galaxy.

### 1.5.1 Surface-mass density systematics

We first address the sources of systematic uncertainty in our surface-mass density estimates, which are pertinent to the following discussions. Our total local surface-mass density, including the correction for stars missing from the age catalogue, but before accounting for any other systematic uncertainties, is  $\Sigma_{R_0,\text{tot}} = 20.0^{+2.4}_{-2.9} \text{ M}_\odot \text{ pc}^{-2}$ . This result is roughly two thirds as large as previous estimates, which are of order  $\Sigma_{R_0,\text{tot}} \sim 30 \text{ M}_\odot \text{ pc}^{-2}$  (e.g. ???). From canonical stellar evolution it is known that giants contribute very little to the total stellar mass in any population. For instance, ? find that giants make up  $\sim 2\%$  of the local stellar mass. By virtue of this fact, conversions of the stellar mass inferred from giant-star counts to that of the total underlying stellar population require a multiplication of the observed counts by a factor of  $\sim 50$ , meaning that any uncertainty in the star counts is amplified in the final surface-mass density estimate. Our quoted statistical error estimates, however, which account for Poisson fluctuations in the stellar counts, cannot fully account for the discrepancy.

We first evaluate whether such a discrepancy may be due to the assumed IMF or stellar evolution model. Tests adopting exponential ? and ? IMFs for the mass calculation resulted in variations of the final  $\Sigma_{R_0,\text{tot}}$  estimate of the order  $\sim 1 \text{ M}_\odot \text{ pc}^{-2}$ , which we incorporate into the systematic error budget. We also re-ran our analysis on the basis of the BaSTI stellar evolution models (?), for which there also exists calculations for  $\alpha$ -enhanced stars (?), which produced comparable estimates to the PARSEC models (after correcting for the fact that the lowest mass in the BaSTI isochrones is  $0.5M_\odot$  as opposed to  $0.1M_\odot$  in the PARSEC models). We also compute the mass using only APOGEE fields away from the plane (with  $|b| \geq 6^\circ$ ), to test for the effects of extinction on the star counts, but attain results within the Poisson uncertainties of the original estimate.

We also apply our analysis procedure to a basic Monte Carlo mock sample, to check the method for converting observed counts to the real number density  $N(R_0)$ . We sample stars on a broken exponential density distribution with exponential flare then select points within APOGEE fields out to an imposed distance cut (which allows a

simple reconstruction of the selection, and calculation of the effective volume). We calculate  $N(R_0)$  analytically, and via our method, and find results which are consistent with the input parameters of the model broken exponential profiles, within the Poisson errors, for a wide variety of input parameters.

[id=TM]As mentioned in Section 1.2.3, we find that, after making corrections to the ages, that the model returns ages greater than 13 Gyr for a sizeable number of stars (? limit ages to 13 Gyr in their table). While these stars make up approximately 10% of the final sample (3020 stars), they are not included in the number counts in each mono-age mono-[Fe/H] bin for calculation of the surface-mass density. Adding an extra 10% of counts to each bin (in the same way as the extra 25% is added in Section 1.2.3) introduces an extra systematic uncertainty of roughly  $1M_\odot \text{ pc}^{-2}$  in each  $[\alpha/\text{Fe}]$  subsample. However, readers should take into account that this simple correction does not account for a scenario where the stars with ages fitted  $> 13$  Gyr might have a specific distribution in age, casting more counts in some bins (which might have more mass contribution per star) than others. For example, if these stars were all old, then the actual surface mass density in older bins would be higher than that found here, which would increase the total surface-mass density estimate.

From the above, we conclude that the majority of the systematic discrepancy is likely not due to the assumed IMF, stellar evolution model, dust extinction, or some peculiarity in the age measurements which affects star counts in the bins used. At this stage, it is difficult to understand what is the possible origin of this discrepancy with other works in the literature. Interestingly, our study is the only one employing giant stars as the stellar population tracer, which may point to possible systematics in the theoretical isochrones, or the APOGEE stellar parameters, or a combination thereof. It has recently been demonstrated by ? that there may be significant issues with the spectroscopic determination of stellar surface gravity, which is dependent on the star's evolutionary state. We find some discrepancy between the  $\log g$  of the red clump between the PARSEC isochrones and the data, of the order  $\sim 0.2$  to  $0.3$  dex (similar to that found by ?, albeit based on APOGEE-DR13 data), which could conceivably lead to problems in our conversion. We test for the effect of systematics in the  $\log g$  scale,

shifting the  $\log g$  cut of the isochrones to lower and higher  $\log g$  by 0.3 dex. We find that shifting the  $\log g$  cut by  $-0.3$  dex increases the surface-mass density estimate by  $5.0 \text{ M}_\odot \text{ pc}^{-2}$ . Increasing the  $\log g$  cut by 0.3dex results in a decrease of  $2.4 \text{ M}_\odot \text{ pc}^{-2}$ . It therefore seems plausible that the discrepancy results from a systematic difference between the  $\log g$  scales of the theoretical isochrones and APOGEE, and so we incorporate these shifts into the systematic error estimate.

Upon inclusion of the systematic uncertainties from IMF variations and differences in the surface gravity scales, we attain a final estimate of the total local surface-mass density in visible stars of  $\Sigma_{R_0,\text{tot}} = 20.0^{+2.4}_{-2.9}(\text{stat.})^{+5.0}_{-2.4}(\text{syst.}) \text{ M}_\odot \text{ pc}^{-2}$ , from the addition of the low  $[\alpha/\text{Fe}]$  surface-mass density of  $\Sigma_{R_0,\text{tot}} = 17.1^{+2.0}_{-2.4}(\text{stat.})^{+4.4}_{-1.9}(\text{syst.}) \text{ M}_\odot \text{ pc}^{-2}$ , and the high  $[\alpha/\text{Fe}]$  value of  $\Sigma_{R_0,\text{tot}} = 3.0^{+0.4}_{-0.5}(\text{stat.})^{+0.6}_{-0.6}(\text{syst.}) \text{ M}_\odot \text{ pc}^{-2}$ . If the  $\log g$  systematics are as large as  $-0.3$  dex, then our result is in agreement with the recent estimate from ?, of  $27 \pm 2.7 \text{ M}_\odot \text{ pc}^{-2}$ .

A recent compilation of measurements of the thick and thin disks found that the thick-thin disk surface density ratio at  $R_0$  is  $f_\Sigma = 15\% \pm 6\%$  (?). Our results find  $f_\Sigma = 18\% \pm 5\%$  for high-low  $[\alpha/\text{Fe}]$  disk surface-mass density ratio, consistent with that estimate. While a better understanding of the possible systematics between the theoretical isochrones and APOGEE is beyond the scope of this paper, we have shown that even a slight difference in the  $\log g$  scale can bring our results in line with existing estimates. This suggests that our surface-mass density measurement discrepancy is indeed systematic, and that the high and low  $[\alpha/\text{Fe}]$  disks may still have some relation to the thick and thin components measured by these studies, which are mainly based on geometric decompositions of the disk.

### 1.5.2 Comparison with MAPs results

We first discuss our density fits in comparison to the MAP measurements of ???. Such a comparison is important because our method is based on an extension of that developed by ? to the case of RGB stars, whose distances are far more uncertain than those of RC stars. ? used the APOGEE RC sample, to find the structure of populations in narrow

bins of  $[\alpha/\text{Fe}]$  and  $[\text{Fe}/\text{H}]$ , or MAPs. These MAPs represent stellar populations with a distribution of ages, but their interpretation assumes a significant relationship between age,  $[\alpha/\text{Fe}]$  and  $[\text{Fe}/\text{H}]$ . We can now compare results when the third parameter, age, is known.

? showed that the radial distribution of low  $[\alpha/\text{Fe}]$  MAPs is well described by a broken exponential, and we confirm this result, showing that each of the low  $[\alpha/\text{Fe}]$ , mono-age, mono-metallicity populations is also described by a radially broken exponential. We also show that the older, high  $[\alpha/\text{Fe}]$  populations are instead described by a single exponential, which is in good agreement with the findings of ?.

The dependence of the radial distribution of mono- $[\text{Fe}/\text{H}]$  populations on age is interesting in this regard. The low  $[\alpha/\text{Fe}]$  population, for which our sample covers a wide range of ages with high signal-to-noise, shows a broadening of the profile around a density peak towards older populations, at all  $[\text{Fe}/\text{H}]$ . This effect does not appear to be present in the high  $[\alpha/\text{Fe}]$  population (although some populations have slight evidence of a break at low significance), which suggests that it was formed and evolved differently. We discuss the implications of these findings in Section 1.5.4.

We also confirm the results of ? which showed that the break radius,  $R_{\text{peak}}$  is a declining function of  $[\text{Fe}/\text{H}]$ . We show that, in the low  $[\alpha/\text{Fe}]$  population, at fixed age,  $R_{\text{peak}}$  moves to smaller radii as  $[\text{Fe}/\text{H}]$  increases. As a function of age, the amplitude of this variation increases. The difference in  $R_{\text{peak}}$  at the highest and lowest  $[\text{Fe}/\text{H}]$  in the 6 Gyr bin is  $\sim 6$  kpc, which is identical with that of the profiles shown in Figure 11 of ?.

? found that low  $[\alpha/\text{Fe}]$  MAPs were fit well with a  $h_Z(R)$  which was slowly exponentially flaring with  $R_{\text{flare}}^{-1} = -0.12 \pm 0.01 \text{ kpc}^{-1}$ . We confirm this result, finding also that low  $[\alpha/\text{Fe}]$  populations have, on average,  $R_{\text{flare}}^{-1} = -0.12 \pm 0.01 \text{ kpc}^{-1}$ , but we also find that  $R_{\text{flare}}^{-1}$  shows considerable variation with age (around this mean) in the low  $[\alpha/\text{Fe}]$  populations. While ? found that high  $[\alpha/\text{Fe}]$  populations were consistent with a having  $R_{\text{flare}}^{-1} = 0.0 \pm 0.02 \text{ kpc}^{-1}$ , we find that these populations have  $R_{\text{flare}}^{-1} = -0.06 \pm 0.02 \text{ kpc}^{-1}$ , showing some evidence of flaring, albeit at a lower level and lower significance than the low  $[\alpha/\text{Fe}]$  populations.

It was also shown by ?? that the  $h_Z([\alpha/\mathrm{Fe}], [\mathrm{Fe}/\mathrm{H}])$  of MAPs smoothly spans the range between 0.2 and 1 kpc. We also confirm and extend this result, showing that  $h_Z(\mathrm{age}, [\alpha/\mathrm{Fe}], [\mathrm{Fe}/\mathrm{H}])$  varies smoothly between a maximum  $h_Z$  of  $\sim 1.2$  kpc in the high  $[\alpha/\mathrm{Fe}]$ , low  $[\mathrm{Fe}/\mathrm{H}]$ , older populations, down to a minimum of  $\sim 0.2$  kpc in the youngest, low  $[\alpha/\mathrm{Fe}]$ ,  $[\mathrm{Fe}/\mathrm{H}]$  rich populations. We can also directly compare our Figure 1.12 with Figure 2 of ?, which showed that the mass-weighted  $h_Z$  distribution is not bimodal but smoothly declines with  $h_Z$ . We confirm that result, showing that for mono-age, mono-metallicity populations, the mass weighted  $h_Z$  distribution shows no sign of bimodality; The low and high  $[\alpha/\mathrm{Fe}]$  populations'  $h_Z$  distributions are distinct but overlap significantly, generating a smooth distribution. This presents an interesting new look at the interplay between spatial and chemical structure in the disk, as there is a clear mixing spatially of the two chemically separated populations. The implications of this finding are intriguing, and we discuss them further in Section 1.5.4.

? also made a measurement of the local surface-mass density, finding (in the original application of the method used here) that SEGUE G-type dwarfs yield an estimate of  $\Sigma_{R_0,\mathrm{tot}} = 30 \pm 1 \mathrm{M}_\odot \mathrm{pc}^{-2}$ , which is in good agreement with other studies based on different samples (e.g. ??). Comparatively, our result is somewhat smaller, even when systematics are taken into account. There are a number of differences between this study and that of ?. For example, the increased radial coverage, adoption of RGB stars as a tracer, and the fits based on mono-age, mono-metallicity (rather than mono-abundance) populations. However, as mentioned above in Section 1.5.1, our results, after accounting for systematic uncertainties, appear in good agreement with other, more recent estimates (?).

### 1.5.3 Comparison with other Milky Way disk studies

We now compare qualitatively the findings of our analysis with the broader body of knowledge regarding the Milky Way disk structure (see, e.g. ??, for recent reviews) . In comparing our results with those from previous studies, we are constrained to making mostly qualitative considerations, as previous work is based on fits of single

exponentials to the radial component of the stellar density distribution.

This work strongly constrains the structure of both the low and high  $[\alpha/\text{Fe}]$  components in the Galactic disk, which are commonly considered to be interchangeable with the thin and thick components (as asserted by, e.g. ???). We have shown that the  $[\alpha/\text{Fe}]$  rich component, while corresponding to a thicker configuration in general, is the product of individual mono-age populations of varying thickness. We find that the  $[\alpha/\text{Fe}]$  rich populations span the range  $0.4 < h_Z < 1 \text{ kpc}$ , with  $h_Z$  increasing with age. Studies of the vertical disk structure which fit a double exponential find a thick disk scale height of  $\sim 1 \text{ kpc}$  (e.g. ??), which is fully consistent with measurements of the thickest high  $[\alpha/\text{Fe}]$ , old, mono-age populations in our analysis. [id=TM]However, we again stress here that the age uncertainties at old ages may be significantly larger than the bin size, which may cause a blurring of these trends, and should be accounted for when comparing these results to models. As an example, in the *worst case* scenario, assuming gaussian errors, the oldest bins (between 7 and 13 Gyr) may be contaminated by up to 50% of the stars which should be assigned to neighbouring bins, at the oldest end, with the fraction dropping off quickly at younger ages. We briefly discuss the implications of the worst case blurring on our interpretation of these trends in Appendix 1.8

Regarding the radial scale length of the thick component, we find an obvious discrepancy with literature values, whereby our thick, high  $[\alpha/\text{Fe}]$ , populations have an average  $h_{R,\text{out}} = 1.9 \pm 0.1 \text{ kpc}$ , while the aforementioned studies, who define the thick disk geometrically, find values of the order  $\sim 4 \text{ kpc}$  (??). This discrepancy appears to arise in the choice of definition of the measured population between a geometric or chemical abundance selection, with many studies finding a scale length for the abundance-selected  $\alpha$ -rich disk in the range  $h_R = 2.0 \pm 0.2 \text{ kpc}$  (????). It should be noted here that our  $h_{R,\text{out}}$  would likely be in even better agreement with this value, had we accounted for the 5% systematic discrepancy in the distances (shown in Figure 1.3). ? recently showed evidence for a radial age gradient in the Milky Way, suggesting this as a source of disagreement between abundance-selected and geometric studies of the thick disk components, where the geometric selected studies see an extended thick

disk which is made up of flared low  $[\alpha/\text{Fe}]$  populations.

We also examine claims of a sharp decline in the stellar density at  $R \sim 13.5$  kpc (e.g. ??) in light of our results. ? fit a single exponential density profile with scale-length  $\sim 3$  kpc to A stars (which preferentially selects stars younger than  $\sim 100$  Myr old) and found that after  $R \sim 13$  kpc, a model with shorter scale-length was necessary to explain the increased rate of decline in stellar density. Our total profile in Figure 1.13 begins to decline after  $R \sim 10$  kpc. The uncertainties in the measurement of the mass contribution of each profile may cause some discrepancy here, as implying a higher mass on older or more metal poor populations would shift this turn-over to higher radii. We also fit older populations than ?, which, under the inside-out formation paradigm, might suggest another reason for such a discrepancy, as older populations would be more centrally concentrated. We confirm the assertion of ? that this break, clearly visible in the total stellar distribution, is attributable to the outermost break of the mono-[Fe/H] profiles - which are shown in the bottom panel of Figure 1.13. External disk galaxies are also observed to have such a truncation in their stellar density profiles (e.g. ?).

#### 1.5.4 Implications for the formation of the Galactic disk

In light of the above discussion, we now present the implications of our results for the formation of the Galactic disk. In this paper, we present a detailed dissection of the disk by age, [Fe/H], and  $[\alpha/\text{Fe}]$ , and as such, present a previously unseen picture of the dominant structure of the Milky Way. In studying mono-age populations, we can perform a more direct comparison than previously possible with numerical simulations of Milky Way type galaxies, which tend to use age information in the absence of detailed chemical modelling.

### Disk flaring, profile broadening and radial migration

By estimating the density profiles of mono-age populations, we place novel constraints on radial migration and its effects on the structure and evolution of the disk. We have two key observables which provide this insight: the flaring of the disk, which has been considered as an effect of vertical action conserving radial migration (where stars have greater vertical excursions as they migrate outward, e.g. ?), and the broadening of the density profiles around the peak with time, which we discuss as a potential new indicator of radial migration. The right panel of Figure 1.9 shows a clear trend of increasing  $R_{\text{flare}}^{-1}$  with age such that the youngest populations flare most. This behaviour is distinct from the results of ?, which found that low  $[\alpha/\text{Fe}]$  populations were described by a single  $R_{\text{flare}}^{-1}$ . It is, however, conceivable that if low  $[\alpha/\text{Fe}]$  populations of all ages are combined, the resulting population may have a similar behaviour as that in ?. Indeed, we find an average  $R_{\text{flare}}^{-1} = -0.12 \pm 0.01 \text{ kpc}^{-1}$ , which is in good agreement with the value from ?. If populations become more flared as radial migration proceeds, then it becomes difficult to reconcile our result with that of a disk whose stars continually underwent radial migration, largely unperturbed by any mergers that might cause structural discontinuity (e.g. ?), especially under suggestions that mergers actually reduce flaring from radial migration (e.g. ?). In this context, this result is indicative of an old population in the Milky Way which has undergone some mergers, reducing the flaring in the oldest populations. It should be noted here, however, that the age uncertainties (which can be as large as 40%) could effectively artificially increase the age bin size, super-imposing populations with different scale heights and flare, and reducing the overall flaring profile.

We showed in Figures 1.8 and 1.6 that the radial surface density profiles of low  $[\alpha/\text{Fe}]$  populations become smoother with age. Interestingly, the position of the break radius does not vary monotonically with age. Assuming that the peak radius is at the equilibrium point of chemical evolution for a given population (where the consumption of gas and its dilution are balanced, as discussed in ?), then one might consider that such a broadening would occur if stars that formed near the equilibrium point migrated inwards and outwards over time. If these assumptions are correct, then the

specific surface density profile shapes might provide insights into how radial migration has proceeded in the disk. For example, if the slope of the inner or outer profile change slope differently, this might suggest that migration has been asymmetric (i.e. more mass has moved in than out or vice versa). Comparing the  $-0.2 < [\text{Fe}/\text{H}] < -0.1$  dex and  $0.0 < [\text{Fe}/\text{H}] < 0.1$  dex bins in Figure 1.6, it seems that the *inner* slope of the former profile decreases more with age, whereas the *outer* slope of the latter decreases more strongly, suggesting that the former population has preferentially migrated in, whereas the latter migrated out. It is important to point out that under the interpretation that the increasing profile width is due to migration efficiency, we make an assumption that stars of a given  $[\text{Fe}/\text{H}]$  and  $[\alpha/\text{Fe}]$  must have been born with the same width throughout cosmic time (as discussed by, e.g. ?).

This picture is also consistent with the suggestion by, e.g. ??, that the changing skew in the MDF as a function of Galactocentric radius is caused by such a mechanism. We show the mass-weighted  $[\text{Fe}/\text{H}]$  distribution for the low  $[\alpha/\text{Fe}]$  fits at different Galactocentric radii in Figure 1.14, showing that our results both find a radial metallicity gradient, and qualitatively reproduce the skew found by ?. Unlike ?, our analysis fully corrects for sample-selection and stellar-population biases in reconstructing the MDF. ? also found similar behaviour in a simulated galaxy, finding that spiral structure induces different migration patterns, dependent on birth radius.

Interestingly, we detect the possible flaring of old, high  $[\alpha/\text{Fe}]$  populations, with average  $R_{\text{flare}}^{-1} = -0.06 \pm 0.02 \text{ kpc}^{-1}$ . However, the right panel of Figure 1.9 shows that the flaring of the high  $[\alpha/\text{Fe}]$  populations does not vary as strongly with age as the low  $[\alpha/\text{Fe}]$  populations (although it should be noted that most of the mass in the high  $[\alpha/\text{Fe}]$  populations is concentrated at older age anyway). The detection of even a slight flare in these populations is surprising, as ? found that the high  $[\alpha/\text{Fe}]$  MAPs did not have flare. Again, this may be an effect of the superposition of multiple mono-age populations within the MAPs. ?, for example, found that co-eval populations in simulated galaxies always flare, and suggested that the superposition of such flares might be an explanation for thickened disk components. ? showed that the superposition of mono-age populations within MAPs can introduce decreased flaring in high  $[\alpha/\text{Fe}]$

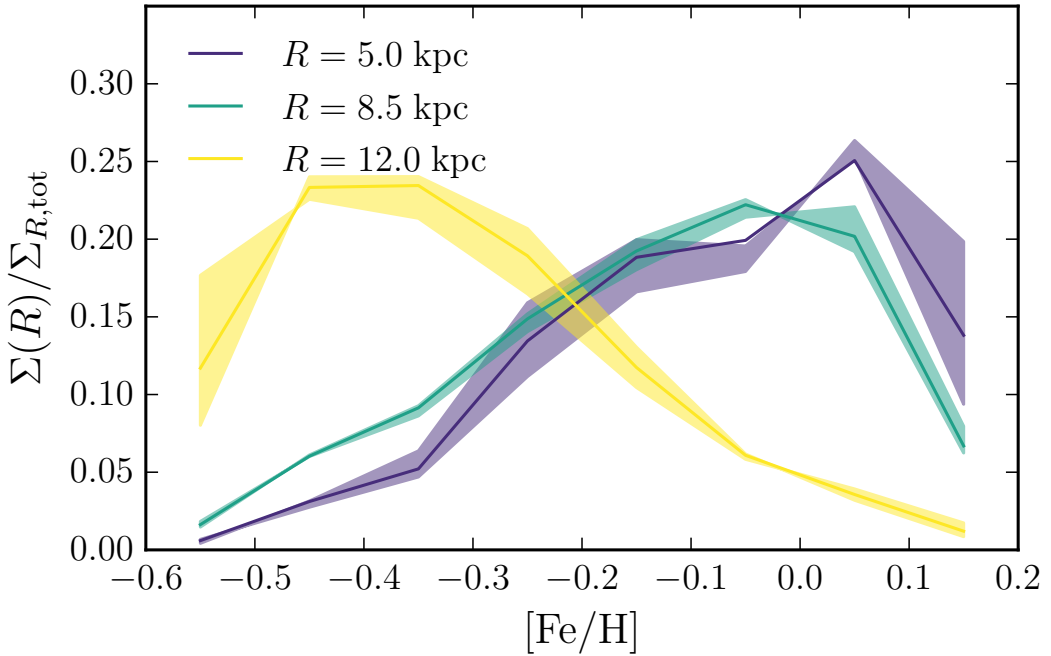


Figure 1.14: The surface-mass density weighted  $[{\rm Fe}/{\rm H}]$  distribution (MDF) at 3 radii for profiles fit to the low  $[\alpha/{\rm Fe}]$  populations. The distribution shown is marginalised in age across all our age bins. The coloured bands give the 95% uncertainty ranges, where uncertainties are dominated by those on the fitted density profiles. The mean  $[{\rm Fe}/{\rm H}]$  is lower at greater  $R$ . Qualitatively, the skew of the MDF’s changes with  $R$ , such that the innermost  $R$  has a tail going to low  $[{\rm Fe}/{\rm H}]$ , and the outermost  $R$  has a tail going to high  $[{\rm Fe}/{\rm H}]$

populations, whilst the mono-age populations themselves still flare. Comparison of these results with ? seems to present a consistent scenario. It should be noted here however, that ? found that MAPs in their simulation were coeval in general.

Our results show that the oldest populations are thicker, centrally concentrated, and display the least flaring, whilst the youngest populations, which show the most flaring, have the thinnest vertical distribution (smallest  $h_Z$ ). Between these extremes, consecutive populations in age form a continuum, when the combined low and high  $[\alpha/{\rm Fe}]$  structure is considered (see Figure 1.9). It is clearly conceivable then, that the *geometrically* defined thick disk, found to have large scale-length (e.g., ??), may be the superposition of these flared (young) and naturally thick (old) components. An obvious consequence of this scenario would be an age-gradient at high  $Z$  above the disk plane, which has been recently shown to be present in the APOGEE data by ?. It was also recently shown that in the Gaia-ESO survey data, the mean structural characteristics of

the abundance selected thick and thin disks appear to overlap at  $[M/H] \sim -0.25$  dex and  $[\alpha/Fe] \sim 0.1$  dex (?), further presenting a scenario where the thick and thin disk components are not necessarily separable from one another, or at least not in abundance space.

### Inside out formation, and the overall vertical disk structure

The formation of the Galactic disk is commonly framed in the paradigm of inside-out formation (e.g., ???). More recently, the effects of radial migration (e.g. ?) were added, in order to produce models that agree better with the observations (e.g. ???). Our measurements of the peak radius of mono-age populations place strong empirical constraints on the evolution of the Milky Way disk over time. The behaviour of  $R_{\text{peak}}$  with age and  $[\text{Fe}/\text{H}]$  is shown in Figure 1.15. We find that the surface-mass density weighted mean  $R_{\text{peak}}$  of low  $[\alpha/\text{Fe}]$  populations remains roughly constant with age, whilst the dispersion about the mean increases with age. This finding is qualitatively consistent with that of e.g. ?, who show that the radial metallicity gradient decreases with the age of the population considered. Our results show that the density peaks of mono- $[\text{Fe}/\text{H}]$  populations become more separated with age. As the mean  $[\text{Fe}/\text{H}]$  at a given  $R$  is dictated by the dominant population in stellar density at that radius, this indicates that we also see a shallowing gradient in  $[\text{Fe}/\text{H}]$  with age. This is reinforced by our finding (also shown in Figure 1.15) that the mean  $R_{\text{peak}}$  decreases with  $[\text{Fe}/\text{H}]$ .

Our results also place strong constraints on models for the formation of the vertical disk structure. We have already discussed that the vertical structure of the disk is commonly framed as having two geometrically distinct (but overlapping) vertical components (e.g. ?). Our results confirm previous work (e.g. ?) that shows that this picture, while providing an acceptable description of the data when analysing the whole population, is not complete when individual populations, either abundance- or age-selected, are considered. We have shown (in Figure 1.12) that for a random mass element, the probability that it belongs to a population of a given  $h_Z$  exponentially declines as  $h_Z$  increases. There are no apparent breaks in this relation at the resolution which we mea-

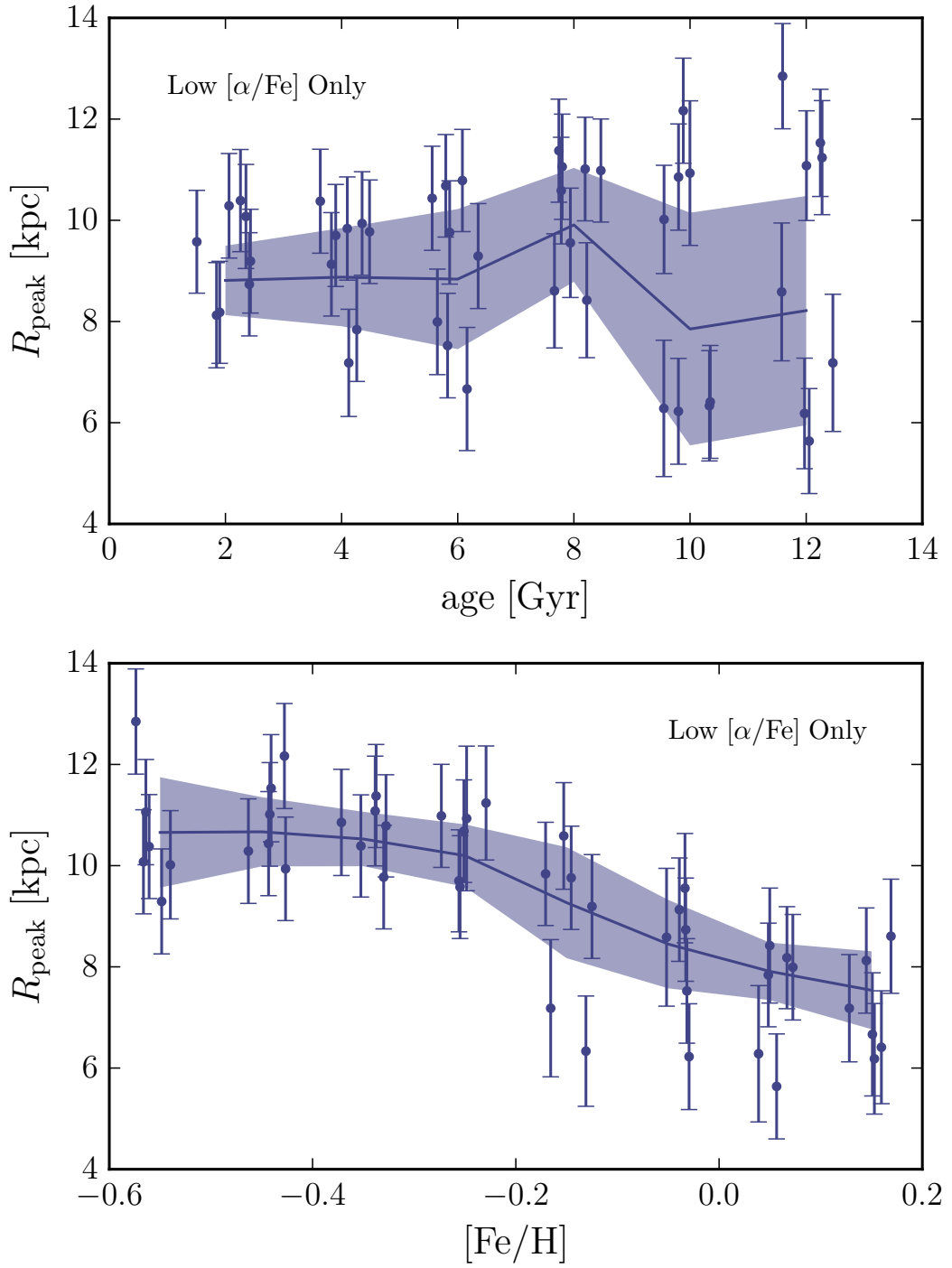


Figure 1.15: The behaviour of  $R_{\text{peak}}$  with age and  $[\text{Fe}/\text{H}]$  for the low  $[\alpha/\text{Fe}]$  populations. The high  $[\alpha/\text{Fe}]$  populations are better fit by single exponentials, and so  $R_{\text{peak}}$  is not an informative diagnostic of these populations. The coloured lines and bands give the surface-mass density weighted mean and standard deviation within an age or  $[\text{Fe}/\text{H}]$  bin. The mean  $R_{\text{peak}}$  does not vary significantly with age, whereas it shows a clear decrease with  $[\text{Fe}/\text{H}]$ . However, the dispersion in  $R_{\text{peak}}$  does increase with age for low  $[\alpha/\text{Fe}]$  populations. High  $[\alpha/\text{Fe}]$  populations show a slight increasing trend for increasing age and  $[\text{Fe}/\text{H}]$ , albeit at low significance.

sure it, strongly suggesting that the spatial vertical disk structure is continuous. This finding, in stark contrast to the distinct discontinuities seen in the chemical structure of the entire disk (e.g. ??), presents an interesting conundrum for galaxy formation theory. How is it possible that the *spatial* structure of the disk be smooth and continuous, whilst the *chemical* structure portrays a clear discontinuity?

Theoretical studies have, thus far, presented some clues as to how galaxy disks such as that of the Milky Way might form. As most studies fit single exponential radial profiles to simulated disks, quantitative comparisons are difficult, yet qualitative considerations can be made. ? used a maximum likelihood method similar to ? to fit density profiles to MAPs in a simulated galaxy and found a continuous distribution of scale heights, but also found that their simulation showed a strongly geometrically distinct thick disk component. ? made detailed measurements of the mono-age populations in a high-resolution hydrodynamic Milky Way-like galaxy simulation, and found, similarly to our results, that their scale heights gradually decreased with time, while the scale lengths increased, with populations forming thick and retaining that thickness in an 'upside-down and inside-out' disk formation. Our results also find evidence of flaring in the thick components (as discussed in Section 1.5.2), which may point towards some structural evolution (via a process such as radial migration) after their formation. However, work on simulations by ? suggests early, turbulent gas as the origin for thicker disk components. A flare in the gas disk of the Milky Way, associated with the stellar component, is also observed in numerous studies (e.g. ???), suggesting a formation of the disk with structural parameters similar to its progenitor gas disk.

### **The age-[Fe/H] distribution and the evolution of the disk**

We now discuss how the present day structural parameters, in combination with the emergent picture of the mass distribution in age-[Fe/H] space at the solar radius, might offer deeper insights into the formation and evolution of the disk.

We find, as may be expected, that the high  $[\alpha/\text{Fe}]$  populations contribute the majority of their mass at the solar radius at ages older than  $\sim 6$  Gyr, although the mass contri-

bution by old stars is extremely low compared to the younger populations. The middle panel of Figure 1.13 shows that, if the populations follow the density models that we fit, then the older stars become more dominant closer to the Galactic centre, which is suggestive of a weak mean radial age gradient, in qualitative agreement with theoretical predictions (e.g. ?) and observations of the thick disk (e.g. ?). It is therefore not surprising that the bottom panel of Figure 1.13 shows a clear variation in mean metallicity, in agreement with findings in other works (e.g. ???). Only with high resolution hydrodynamical simulations, which accurately reproduce the stellar populations in galaxies, will it be possible to reconstruct the right combination of star formation history and radial mixing that led to these age and metallicity gradients, to gain a better understanding of the details of their formation.

In Figure 1.11, an overlap in age-[Fe/H] space is visible between the high and low  $[\alpha/\text{Fe}]$  populations. While there appears to be mass at many [Fe/H] bins in the old populations, the overlap in age occurs at intermediate [Fe/H] at the solar radius. Previous studies have found that the youngest stars in the high  $[\alpha/\text{Fe}]$  sequence overlap in age with the oldest and most [Fe/H] poor stars in the low  $[\alpha/\text{Fe}]$  population (e.g. ?), and our findings appear to be consistent with that result. It should however, be noted, that at least some of this overlap is likely caused by the age uncertainties, which can be as high as 40%. If the low  $[\alpha/\text{Fe}]$  population emerged from the remnants of the high  $[\alpha/\text{Fe}]$ , then it is likely that some sort of infall event must have occurred to return the ISM to low [Fe/H] and low  $[\alpha/\text{Fe}]$  before forming those stars (as expressed by, e.g., ?). These scenarios are also discussed in the context of the APOGEE results by ?. To fully understand this, however, we will likely require a chemodynamical model which reproduces the bimodality in  $[\alpha/\text{Fe}]$  at fixed [Fe/H].

## 1.6 Conclusions

We have performed the first detailed dissection of the stellar populations of the Milky Way disk in age, [Fe/H] and  $[\alpha/\text{Fe}]$  space, bridging the gap between the detailed observational understanding of mono-abundance populations (e.g. ??) and the plethora of

studies of co-eval stellar populations in simulated galaxies (e.g ???). We have placed novel constraints on models for the formation of the Milky Way disk by combining detailed density models fit to the mono-age, mono-[Fe/H] populations of the low and high  $[\alpha/\text{Fe}]$  disk, with surface mass density contributions calculated on the basis of these density fits and stellar evolution models. We summarise our key results as follows:

- **Radial and vertical profiles** The mono-age, mono-[Fe/H] populations of the  $[\alpha/\text{Fe}]$  poor disk are well fit by a radially broken exponential, with a peak radius,  $R_{\text{peak}}$ , that varies as a function of age and [Fe/H]. We find that the distance between  $R_{\text{peak}}$ 's of the low and high [Fe/H] populations increases with age, which we interpret as evidence for a decreasing [Fe/H] gradient with time (e.g ?). The radial variation of the stellar surface density of the high  $[\alpha/\text{Fe}]$  mono-age populations is found to have insignificant breaks, and they are better fit by a single exponential in this disk region. As these populations are the oldest, this may be a sign of the disk evolution washing out the density peak over time, or may point to a different formation scenario for high  $[\alpha/\text{Fe}]$  stars, where no density peak ever existed. These findings are in good agreement with earlier studies of MAPs (?). We measure an average high  $[\alpha/\text{Fe}]$  population scale length of  $h_{R,\text{in}} = 1.9 \pm 0.1$  kpc, and find scale heights between 600 and 1000 pc, in good agreement with current measures of the  $[\alpha/\text{Fe}]$  rich disk scale length and height (e.g. those outlined in ?).
- **Profile Broadening** We show that the radial surface density profile of the low  $[\alpha/\text{Fe}]$  populations broadens with age in a given [Fe/H] bin, which we interpret as evidence of the gradual dispersal of mono-[Fe/H] populations, presumably due to radial migration and radial heating. The variation in shape of the broken exponential profile changes differently depending on the population [Fe/H], with *low* [Fe/H] populations *inner* profiles flattening faster, whereas the *high* [Fe/H] *outer* profiles flatten faster. We interpret this effect as tentative evidence for [Fe/H] dependent radial migration arising from pre-existing [Fe/H] gradients in the star forming disk. We showed that our results qualitatively reproduce those

of ?, finding a skewed MDF that varies as a function of R.

- **Flaring** We find that flaring seems to be present in almost all mono-age populations, at differing levels. We have shown that the inverse flaring scale length  $R_{\text{flare}}^{-1}$  increases with age, meaning that the youngest populations flare most strongly. This finding appears inconsistent with that above, under the assumption that flaring is the result of radial migration. However, these results may be reconciled by invoking a more active accretion history in the early life of the disk, which could have suppressed flaring (e.g. ?).
- **The surface-mass density at  $R_0$**  We have measured the surface mass-density at the solar radius for each mono-age, mono-[Fe/H] population, finding a total surface mass density of  $\Sigma_{R_0,\text{tot}} = 20.0^{+2.4}_{-2.9}(\text{stat.})^{+5.0}_{-2.4}(\text{syst.}) \text{ M}_\odot \text{ pc}^{-2}$ . Before allowing for systematics, this value is less than current estimates (e.g. ???), however, the systematic uncertainties are large, mainly due to a mismatch between the log  $g$  scales in APOGEE and the PARSEC models, and as such, we find our value to be consistent within the uncertainties. The relative contribution of high to low  $[\alpha/\text{Fe}]$  populations,  $f_\Sigma$ , is  $18\% \pm 5\%$ , which is consistent with existing measurements (e.g. ?).
- **The  $h_Z$  distribution at  $R_0$**  The shape of the mass-weighted  $h_Z$  distribution found by this study is in good agreement with that of ?, calling into question the existence of a vertical structural discontinuity in the Milky Way disk. The reconciliation of this finding with the discontinuity in chemical space (e.g. the bimodality in  $[\alpha/\text{Fe}]$  at fixed [Fe/H]: ??) may shed new light on our understanding of the formation of the Galactic disk.
- **The surface-mass density profile of the Milky Way** We have found the combined (from mono-age, mono-[Fe/H] populations at low and high  $[\alpha/\text{Fe}]$ ) surface-mass density weighted profiles of the Milky Way disk as a function of  $[\alpha/\text{Fe}]$ , age and [Fe/H], and found that the total surface density is also described by a broken exponential. We find that our results fail to determine the sign of the inner exponential to high significance out to  $\sim 10$  kpc, but detect a turnover to a

declining exponential, at high significance, thereafter. We find evidence of a radial mean age and [Fe/H] gradient driven by the changing dominant population as a function of radius. A detailed comparison of these findings with numerical simulations is necessary for a proper interpretation. Our finding of a decline in stellar density may be consistent with that found in other studies (e.g. ??), albeit at shorter radii.

These findings are strongly constraining to future theoretical work. With the recent (?) and future releases of *Gaia* data, and the ongoing APOGEE-2 survey (?), which will include an updated APOKASC sample (?), access to improved positions, abundances and age estimates is within reach. [id=TM]We again stress here that the age uncertainties in this data set can be as large as 40%, and so until more precise ages are attained for similarly sized samples, our conclusions must be considered under the caveat that the mono-age populations at old age are likely mixed to some extent. It will be possible to investigate this issue better once better ages for a larger sample are released by APOGEE and APOKASC (?).

Future studies of simulations which accurately track chemical evolution, gas and stellar dynamics, and the feedback processes which are dominant in galaxies will no doubt lead to a deeper insight into the physical processes leading to the present day structure of the Milky Way. The understanding of discontinuity in chemical space, namely the bimodality in  $[\alpha/\text{Fe}]$  at fixed [Fe/H], and how this can be reconciled with the apparent structural continuity which we find here poses an interesting challenge to models of the formation of the Milky Way disk. By performing a first mapping of the 3D distribution of stellar populations as a function of age, metallicity, and [a/Fe], we hope that this work provides the kind of data needed for a comparison with numerical simulations that is unencumbered by the complexities associated with corrections for the survey selection function.

## 1.7 Density Fits

For completeness, we briefly discuss the quality of the fits performed with the method outlined in section 1.3. Figures 1.16 and 1.17 show the distance modulus distribution of the APOGEE data in each of our mono-age and mono-[Fe/H] bins (grey histograms) and the resulting distance modulus distribution when the best fit density model for each bin is run through the calculated effective selection function (which is the space in which models are fit in our procedure). The red line represents a single-exponential fit to the radial and vertical spatial distribution and the black lines give the best fit broken-exponential density model (upon which we base our results). We show the single-exponential fit in order to demonstrate that, in most cases, this does not provide a good fit to the data, and that when a single exponential is a better fit, the broken-exponential density fit matches it.

Regarding Figure 1.16, which shows the low  $[\alpha/\text{Fe}]$  sub-populations, it is clear that the black curve (broken exponential) represents a far better model for the data than the red curve (single exponential), in all mono-age, mono-[Fe/H] bins. While the black curve is not perfect in all cases, the peak of the distribution tends to lie at the correct  $\mu$ , whereas the red curve finds a peak at higher  $\mu$  in most cases (due to the higher than necessary density at low Galactocentric radius in this model).

Figure 1.17 demonstrates the fits for the high  $[\alpha/\text{Fe}]$  sub-populations. The greyed out panels reflect those with less than 30 stars, which we deem too noisy to render reliable fits. In many of the remaining panels, the red curve is similar or identical to the black, due to the fact that many of the high  $[\alpha/\text{Fe}]$  populations are better described by single exponentials, and the broken exponential generally recovers this result. In most of the cases where the curves differ greatly, the red curve recovers the peak of the distribution better than the black - suggesting that breaks which were fit in the radial range we consider are artificial, and due to the noisy data in this regime. We discuss the broken exponential fits in the main text in order to make proper comparison with the low  $[\alpha/\text{Fe}]$  sample, although it seems plausible that the single exponential model provides a better explanation of the data.

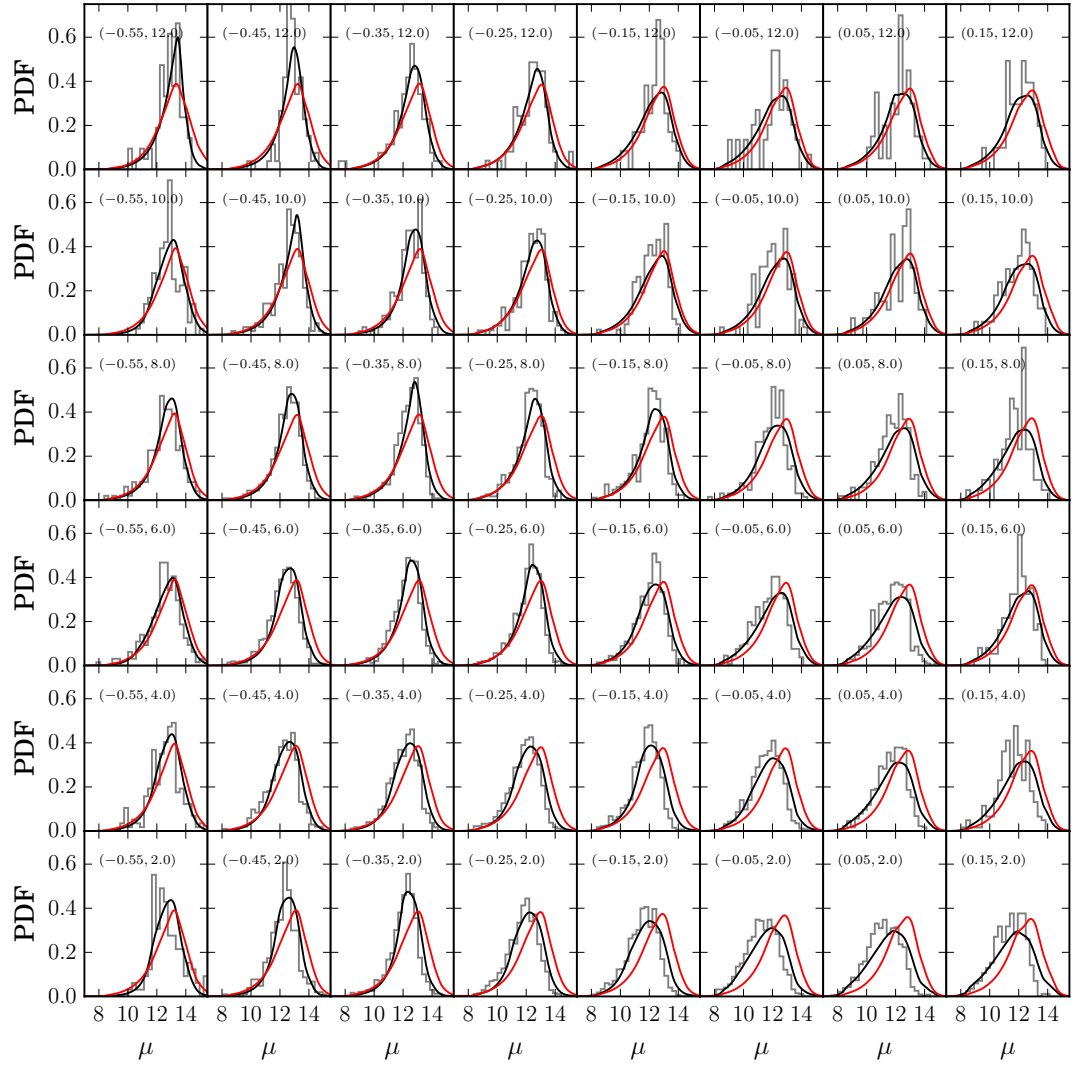


Figure 1.16: Comparison between the best fit models and the APOGEE data for mono-age, mono-[Fe/H] populations in the low  $[\alpha/\text{Fe}]$  sub-sample. The grey histogram shows the distance modulus distribution of the APOGEE data for the mono-age, mono-[Fe/H] bin indicated by the  $([\text{Fe}/\text{H}] \text{ [dex]}, \text{age} [\text{Gyr}])$  coordinate given in each panel. The coloured curves show the distance modulus distribution found when the best fit broken exponential (black) and single exponential (red) density model is run through the effective selection function. It is clear that the broken exponential density model provides a qualitatively better fit to the data in all cases.

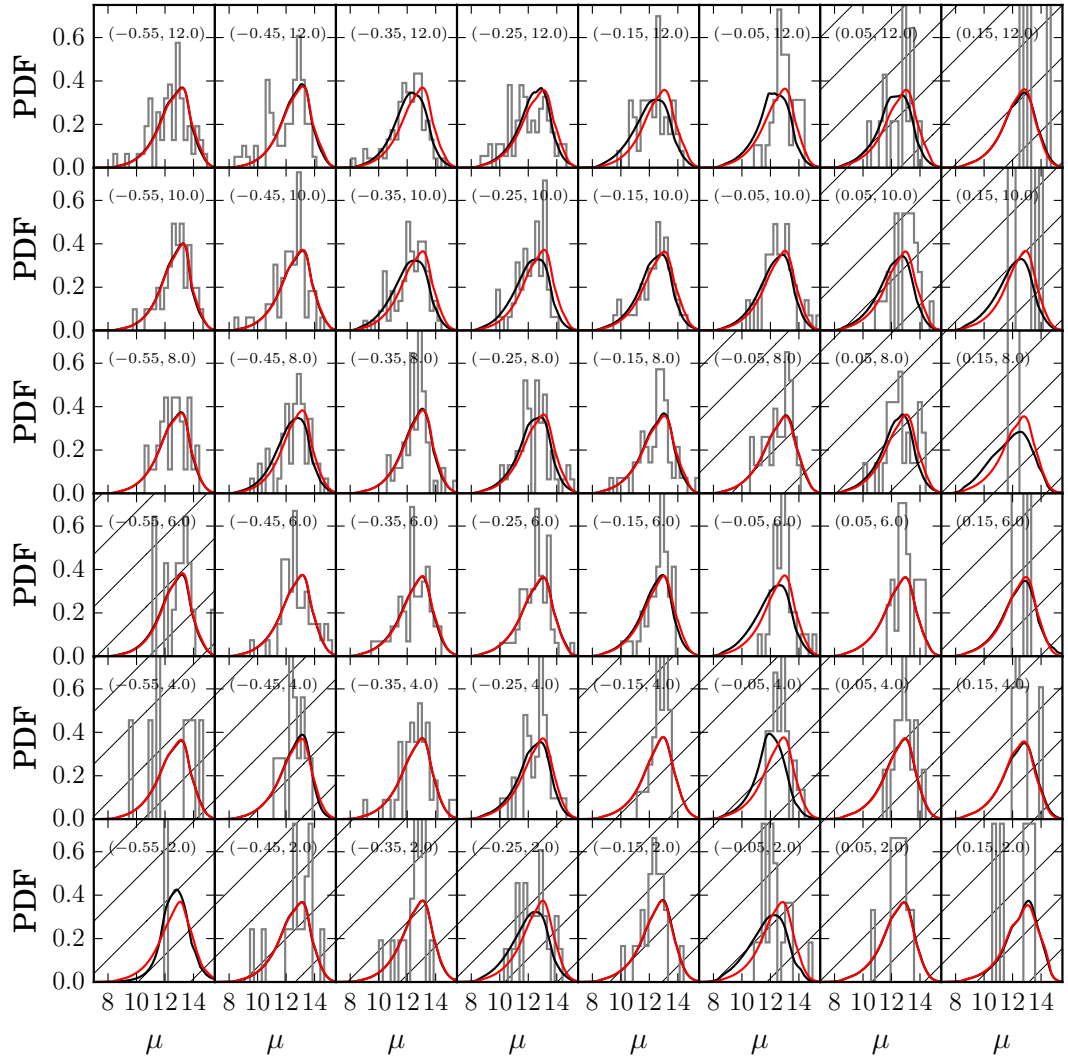


Figure 1.17: Comparison between the best fit models and the APOGEE data for mono-age, mono-[Fe/H] populations in the high  $[\alpha/\text{Fe}]$  sub-sample. The grey histogram shows the distance modulus distribution of the APOGEE data for the mono-age, mono-[Fe/H] bin indicated by the ( $[\text{Fe}/\text{H}]$  [dex], age [Gyr]) coordinate given in each panel. The coloured curves show the distance modulus distribution found when the best fit broken exponential (black) and single exponential (red) density model is run through the effective selection function. In many cases the red and black curves are indistinguishable (only red is seen), or very similar. In cases where the black and red curves are different, the red provides a qualitatively better fit. Bins with less than 30 stars (which we disregard for the majority of the analysis) are hatched out.

## 1.8 The effect of uncertainties on trends with age

[id=TM]In order to demonstrate and characterise the effect that the age errors have on our interpretation of the trends between structural parameters and age, we created a mock data set from a set of randomly sampled density distributions. We created a mock data set with an input trend of  $h_Z$  with age which increased monotonically with age from 0.2 to 1.2 kpc. Ages were assigned to each  $h_Z$  population, sampling uniformly in bins of width 2 Gyr, to which we then added a random gaussian error of 40%, replicating the shifting of stars with different  $h_Z$  into each age bin. In each bin, we sample a single exponential (a broken exponential with  $R_{\text{peak}} = 0$ ) with scale length 8 kpc. This higher scale length is required to make the test computationally efficient, to produce realistic numbers of stars when selecting stars in APOGEE fields and does not impact on the results of this test. We assume no error on the stellar positions, in order to isolate the effect of the age errors.

[id=TM]While this test is a somewhat simplistic representation of the underlying processes, it serves as a good example of the effect of the age uncertainties which are expected in the present data. One example of its simplicity is the assignment of a single  $h_Z$  to relatively wide bins in age. It seems logical to assume that if there is an age- $h_Z$  relation, then the change in  $h_Z$  should be somewhat continuous with age. Our test assigns the same  $h_Z$  to stars at bin edges (which should have  $h_Z$  close to that of the bin-edge stars in the neighbouring bin). This may artificially increase the amount of blurring of the age- $h_Z$  trend. We also simplify the test by assuming that the only changing parameter is the scale height. Realistic structural parameters would change the relative number of stars within each bin observed by APOGEE (and considered in our test), and may change the level of contamination between bins. However, we assume that our simple approximation represents a ‘worst case’ scenario, where the mixing between bins is maximal.

[id=TM]We restrict the mock data to the APOGEE fields, simplifying the selection to a distance cut (assuming the selection fraction is 1 out to a distance which corresponds to  $M_H = -1.5$ , assuming no extinction). We apply the method described in Section 1.3

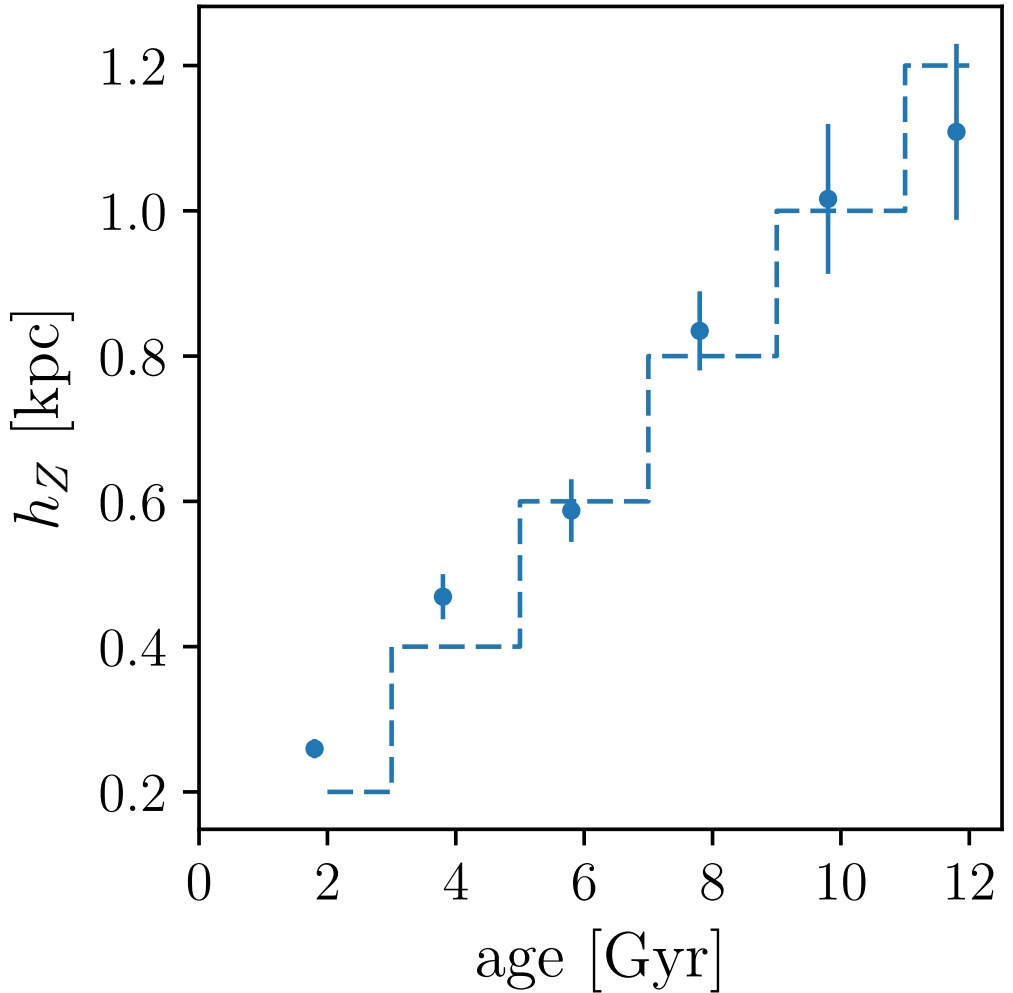


Figure 1.18: [id=TM]The resulting age- $h_Z$  trend from the monte carlo sampling of a set of mock density distributions. The input density models had  $h_Z$  increasing monotonically with age (in bins of  $\Delta\text{age} = 2$  Gyr) from 0.2 to 1.2 kpc (shown by the *blue dashed line*). After sampling of the density distribution, we applied random errors of 40% to the mock ages, and measured the structural parameters using the exact density fitting method applied to the APOGEE data. The method is able to approximately recover the general shape of the input age- $h_Z$  relation, showing a clear trend with age. The age errors increase the error bar sizes significantly where mixing does occur, but the results are consistent with the input in most cases.

to our mock data, fitting a broken exponential profile, and using the best fit solution to initiate an MCMC sampling of the posterior probability distribution. As in the main body of the paper, the reported parameter values reflect the median and  $\sigma$  of one dimensional projections of the MCMC chain. The resulting age- $h_Z$  relation is shown in Figure 1.18. A clear trend is recovered between age and  $h_Z$ . The trend is still recovered at high age, regardless of the high level of mixing between bins, which increases the size of the error bars. The higher-scale height components are recovered by the analysis, but results are scattered around the input values, with large error bars. This serves to show that even in the face of large age uncertainties causing mixing between the adopted bins, our method is still able to recover the underlying trends of parameters with age.

# Chapter 2

## EAGLE

### 2.1 Introduction

The elemental abundances of long-lived stars are a rich fossil record of the formation history of their host galaxy. Spectroscopic surveys of the Galaxy’s stars have therefore long held the promise of elucidating its origin (see, e.g. ???, and references therein). The recent advent of surveys that measure the elemental abundances of tens to hundreds of thousands of Milky Way stars (e.g., RAVE, ??; SEGUE, ??; Gaia-ESO, ??; GALAH, ?? and ??; APOGEE, ??) heralds a significant step towards realisation of the potential of what has come to be known as ‘galactic archaeology’.

One of the primary diagnostics employed by such surveys is the relationship between the abundance ratio of  $\alpha$ -elements and iron,  $[\alpha/\text{Fe}]$ , and the iron abundance,  $[\text{Fe}/\text{H}]$ . The distribution of Galactic *disc* stars in the  $[\alpha/\text{Fe}]-[\text{Fe}/\text{H}]$  plane exhibits striking trends, with observations generally revealing a spread or even bimodality in  $[\alpha/\text{Fe}]$  at fixed  $[\text{Fe}/\text{H}]$ , both in the solar neighborhood (e.g. ????????) and throughout the Galactic disc (???). These differing relative values of  $[\alpha/\text{Fe}]$  are often interpreted as evidence that the populations are distinct. The population with supersolar  $[\alpha/\text{Fe}]$  is generally thought to have formed rapidly, early in the history of the Galaxy, such that its progenitor gas was enriched primarily with  $\alpha$ -elements synthesised and promptly

released by Type II supernovae (SNe), whilst incorporating relatively little iron synthesised by Type Ia SNe (e.g., ??), whose contribution to the enrichment of the interstellar medium only becomes important on timescales longer than  $\sim 10^9$  yr after the onset of star formation.

These two components of the Galactic disc, defined purely on the basis of their abundances, are commonly associated with the structural entities referred to as the thin and thick discs (e.g. ???). However, when mono-abundance and mono-age populations (i.e. stars whose elemental abundances and/or ages are similar within some tolerance) are considered separately, it becomes clear that there is not a direct correlation between a star's association with the Galaxy's thick or thin disc components, and its  $\alpha$ -enhancement (e.g. ??), or its age (?). Recent studies also suggest that there may be a link between the moderately metal-poor  $\alpha$ -enhanced populations in the inner Galaxy and the high-[ $\alpha$ /Fe] disc (e.g. ?), motivated by the fact that metal-poor, high-[ $\alpha$ /Fe] stars in the Galactic centre exhibit ‘hotter’ kinematics (e.g. ????) than their low- $\alpha$ , more metal-rich, counterparts. Although sample sizes are limited, the  $\alpha$ -element abundances of the bulge high-[ $\alpha$ /Fe] population are similar to those of high-[ $\alpha$ /Fe] stars in the local disc, at least as far as Mg and Si are concerned (e.g. ??). The similarities in abundances and coincident structure and kinematics between  $\alpha$ -enhanced bulge populations and the high-[ $\alpha$ /Fe] disc may indicate a common origin of these populations (e.g. ?).

Since disc populations with markedly different [ $\alpha$ /Fe] at fixed [Fe/H] very likely result from different star formation histories, it is challenging to reconcile their co-spatiality in the Galactic disc with the predictions of one-zone chemical evolution models (e.g., ??). While such simple models essentially inaugurated the field of quantitative chemical evolution modeling, they had important limitations. Chief amongst those is their failure to reproduce the metallicity distribution function (MDF) of stars in the solar neighbourhood (known as the ‘G-dwarf problem’, ??). This motivated the development of more detailed chemical evolution models, for example, allowing for the consideration of gas inflow (??), radial gas flow (e.g. ?), and eventually the decomposition of the Galactic disc into concentric evolution zones to capture the effects of ‘inside

out’ formation (e.g. ???).

Over the past two decades, two classes of analytic models in particular have attracted attention, owing to their ability to reproduce broadly the observed elemental abundance trends in the solar neighbourhood, and abundance gradients throughout the disc. These are i) models in which the high- and low-[ $\alpha$ /Fe] components of the discs form in response to distinct episodes of gas accretion, during which gas is consumed at different rates (??); and ii) models in which the two components represent the equilibrium star formation conditions in different parts of the disc, but later become co-incident as a consequence of the radial mixing of stars (??).

The ‘two-infall model’ of ??, invokes an intense initial phase of star formation whose brevity precludes enrichment of the interstellar medium (ISM) by Type Ia SNe, thus resulting in the formation of the high-[ $\alpha$ /Fe] sequence. A hiatus in star formation is then invoked, during which the unconsumed fraction of the gas delivered by the first infall (which is assumed to remain in place without consumption by star formation or ejection by feedback) is enriched by Type Ia SNe, reducing its [ $\alpha$ /Fe]. A second, more prolonged episode of gas infall then triggers the steady formation of the stars comprising the low-[ $\alpha$ /Fe] sequence. The ‘radial migration’ model of ? assumes a continuous, smoothly-varying delivery of gas to the disc, but allows for the exchange of star-forming gas and stars between adjacent radial bins. This allows for the present-day co-location of disc stars whose formation conditions (and hence their location in [ $\alpha$ /Fe]-[Fe/H] space) differed significantly. Bimodality of [ $\alpha$ /Fe] at fixed [Fe/H] therefore stems from such a superposition of populations, fostered by the outward migration of high-[ $\alpha$ /Fe] stars that formed rapidly close to the Galactic centre, and the inward migration of low-[ $\alpha$ /Fe] stars formed farther out in the Galactic disc.

Recently, ? used their flexible analytic chemical evolution model FLEXCE, to scrutinise the viability of these scenarios and assess their sensitivity to the variation of free parameters. They concluded that both models are able to produce high- and low-[ $\alpha$ /Fe] sequences, but identified potential shortcomings in both: the two-infall model requires fine-tuning of the duration of the hiatus and may be incapable of yielding the bimodality in [ $\alpha$ /Fe] over an extended range of [Fe/H] seen by APOGEE (see, e.g. ??).

Their implementation of the radial migration scenario produces a weaker bimodality than that revealed by APOGEE.

Analytic galaxy chemical evolution models such as those described above are an instructive means of assessing the impact of physical processes on the element abundance evolution of stellar populations. However, the scope and predictive power of such models is limited by their recourse to restrictive simplifications and approximations, such as the adoption of arbitrary inflow rates, simplistic gas distributions, and the assumption of complete and instantaneous mixing. Hydrodynamical simulations starting from cosmological initial conditions offer a complementary means of studying the origin of features such as the Galaxy’s  $[\alpha/\text{Fe}]\text{-}[\text{Fe}/\text{H}]$  distribution, since they are unencumbered by the most restrictive of these simplifications. The chief drawback of this approach has been the lack, to date, of realistic simulations capable of reproducing the key physical properties of the galaxy population, including the element abundance patterns of their disc stars.

Simulations of individual galaxies have successfully produced galaxies with old, thick stellar components with disc-like kinematics and, in cases where elemental abundances were tracked, enhanced  $\alpha$  abundances (e.g. ?????). Examination of the ages of disc stars (for which  $[\alpha/\text{Fe}]$  is often considered a proxy) in simulations has proven instructive, suggesting that the old, thick discs of Milky Way-like galaxies appear to form ‘upside-down’ and ‘inside-out’, such that discs are born thick, and gradually become thinner (e.g.????), likely in response to the decline of the gas accretion rate onto the galaxy and the concomitant decline of energy injection into the interstellar medium (ISM) from feedback. It has also been posited that ‘upside down’ formation of a thick disc component may instead be a consequence of mergers between gas-rich clumps at early epochs (e.g. ???). Models in which elemental abundances are ‘painted’ onto particles in N-body simulations successfully reproduce the geometry of mono-age and mono-abundance populations, (e.g. ???). Such models provide a means of understanding the presence of age gradients in the *geometric* thick disc of the Milky Way (e.g. ??), as well as the appearance of radially extended thick disc components in external galaxies (e.g. ?).

? recently reported the formation of disc star populations exhibiting both high- and low-[ $\alpha$ /Fe] components in several hydrodynamical simulations of individual  $\sim L^*$  galaxies. Those authors studied 6 high-resolution ‘zoom’ simulations from the Auriga suite (?), and concluded that bimodal populations can form via two pathways. Bimodality in the inner disc is the result of a two-phase star formation history (SFH), characterized by a short but intense episode of star formation in the first Gyr or so, followed by a more prolonged and gentle SFH. In the outer disc, bimodality results from a brief cessation of star formation, associated with a phase of contraction of the early  $\alpha$ -rich gas disc, followed by star formation reignition. The latter may be caused by accretion of fresh gas, predominantly associated with the merger of gas-rich satellites. Those authors remark that the formation of bimodal [ $\alpha$ /Fe] sequences is not a universal outcome of their galaxy formation simulations, raising the questions of which haloes it arises in, and in response to which physical processes.

In this paper we present an analysis of the distribution on the [ $\alpha$ /Fe]-[Fe/H] plane of the disc stars of Milky Way-like galaxies in the EAGLE cosmological simulations of galaxy formation (??). The galaxy population formed by EAGLE has been shown to reproduce a broad range of observed galaxy properties and scaling relations, both at the present-day and at early cosmic epochs, such as the colour-magnitude relation (???), the Tully-Fisher relation (?), and the evolution of galaxy sizes (?). EAGLE has also been shown to reproduce the observed  $\alpha$ -enhancement of massive galaxies (?). The largest-volume EAGLE simulation follows the evolution of a periodic, cubic cosmic volume of  $L = 100$  cMpc on a side, yielding a large population of galaxies, with diverse formation histories and present-day environments. Our objective is to examine whether galaxies with bimodal [ $\alpha$ /Fe] at fixed [Fe/H] form within EAGLE and, if so, to establish the physical drivers underpinning their emergence. In the process, we exploit the statistics afforded by the EAGLE simulations to assess whether one should expect that the distribution of elemental abundance patterns exhibited by the Galactic disc is common amongst late-type galaxies of a similar mass, thus enabling us to interpret the findings of surveys such as APOGEE in the broader context of galaxy formation theory.

The paper is organised as follows. In Section 2.2, we briefly summarise the EAGLE simulations and present our numerical methods. In Section 2.3 we explore the  $[\alpha/\text{Fe}]$ - $[\text{Fe}/\text{H}]$  distribution of present-day Milky Way-like galaxies in EAGLE, examining correlations with the birth properties of stellar populations, the diversity of the distributions, and the frequency with which galaxies exhibit distinct  $[\alpha/\text{Fe}]$ - $[\text{Fe}/\text{H}]$  sequences. In Section 2.4, we explore the origin of  $[\alpha/\text{Fe}]$  bimodality by studying the gas infall and enrichment histories of EAGLE galaxies. In Section 2.5 we examine the connection between bimodal  $[\alpha/\text{Fe}]$  distributions in galaxy discs, and the accretion history of their host dark matter haloes. We summarise our findings and discuss their broader implications in Section 2.6. Throughout, we adopt the convention of prefixing units of length with ‘c’ and ‘p’ to denote, respectively, comoving and proper scales, e.g. cMpc for comoving megaparsecs.

## 2.2 Numerical Simulations & methods

This section provides a brief overview of the simulations (Section 2.2.1) and their subgrid physics routines (Section 2.2.1). We focus in particular on the aspects of the implemented physics most relevant for this study, and direct the reader to the reference and methods papers of the EAGLE simulations for a more comprehensive description. Section 2.2.2 describes our methods for identifying and characterising galaxies.

### 2.2.1 The EAGLE simulations

The simulations analysed here are drawn from the EAGLE suite of cosmological, hydrodynamical simulations (??), which model the formation and evolution of galaxies in a  $\Lambda$ CDM cosmogony described by the parameters advocated by the ?, namely  $\Omega_0 = 0.307$ ,  $\Omega_b = 0.04825$ ,  $\Omega_\Lambda = 0.693$ ,  $\sigma_8 = 0.8288$ ,  $n_s = 0.9611$ ,  $h = 0.6777$ ,  $Y = 0.248$ . The simulations were performed using a modified version of the smoothed particle hydrodynamics (SPH) and TreePM gravity solver GADGET 3, most recently described by ?. Modifications include the implementation of the pressure-entropy for-

mulation of SPH presented by ?, the time-step limiter of ?, and switches for artificial viscosity and artificial conduction of the forms proposed by, respectively, ? and ?.

We examine several simulations from the EAGLE suite, primarily the simulation with the largest volume, Ref-L100N1504, which adopts the ‘Reference’ model parameters (see ?) and follows a periodic cube of side  $L = 100$  cMpc with  $1504^3$  collisionless dark matter particles of mass  $9.70 \times 10^6 M_\odot$  and an (initially) equal number of SPH particles of mass  $1.81 \times 10^6 M_\odot$ . The simulations conducted at this ‘intermediate’ resolution adopt a Plummer-equivalent gravitational softening length of  $\epsilon_{\text{com}} = 2.66$  ckpc, limited to a maximum proper length of  $\epsilon_{\text{prop}} = 0.7$  pkpc. To explore the enrichment history of galaxies at high temporal resolution, we also examine a realisation of Ref-L025N0376, (which has the same resolution as Ref-L100N1504, but follows a smaller  $L = 25$  cMpc volume), for which 1000 full snapshots were recorded, rather than the usual 28, at an approximate spacing of 12 Myr.

### Subgrid physics

The simulations adopt a metallicity-dependent density threshold for star formation (?). Gas particles denser than this threshold are eligible for stochastic conversion into stellar particles, with a probability that is dependent on their pressure (?). Supermassive black holes (BHs) are seeded in haloes identified by a friends-of-friends (FoF) algorithm run periodically during the simulation, and grow by gas accretion and mergers with other black holes (see, e.g. ???). The rate of gas accretion onto BHs is influenced by the angular momentum of gas close to the BH (see ?) and does not exceed the Eddington limit.

Feedback associated with the evolution of massive stars (‘stellar feedback’) and the growth of BHs (‘AGN feedback’) is implemented as stochastic heating following ?. Outflows develop without the need to specify an initial mass loading or velocity, and do not require that radiative cooling or hydrodynamic forces are temporarily disabled. The efficiency of stellar feedback is dependent upon the local density and metallicity of each newly-formed stellar particle to account, respectively, for residual spurious

resolution-dependent radiative losses, and increased thermal losses in metal-rich gas. The dependence on these properties was calibrated to ensure that the simulations reproduce the present-day galaxy stellar mass function, whilst also yielding disc galaxies with realistic sizes (?). The efficiency of AGN feedback was calibrated to ensure that the simulations reproduce the present day scaling between the stellar masses of galaxies and the mass of their central BH.

The mass of stellar particles is  $\sim 10^6 M_\odot$ , so each represents a population of stars and can be considered as a simple stellar population (SSP). We assume the initial distribution of stellar masses to be described by the ? initial mass function (IMF) in the range  $0.1 - 100 M_\odot$ . The return of mass and nucleosynthesised metals from stars to interstellar gas is implemented as per ?. The scheme follows the abundances of the 11 elements most important for radiative cooling and photoheating (H, He, C, N, O, Ne, Mg, Si, S, Ca and Fe), using nucleosynthetic yields for massive stars, Type Ia SNe, Type II SNe and the AGB phase from ? and ?. We use the metallicity-dependent stellar lifetimes advocated by ?. The ‘lifetimes’ of Type Ia SNe are described by an empirically-motivated exponential delay time distribution, such that their rate per unit initial stellar mass is:

$$\dot{N}_{\text{SNIa}}(t) = \nu \frac{e^{-t/\tau}}{\tau}, \quad (2.1)$$

where  $\nu = 2 \times 10^{-3} M_\odot^{-1}$  is the total number of Type Ia SNe per unit initial mass, and  $\tau = 2 \text{ Gyr}$  is the e-folding timescale. These parameters were calibrated to ensure that the simulations broadly reproduce the observed evolution of the cosmic Type Ia SNe rate density (?).

At each timestep, the mass and metals released from evolving stellar populations are transferred from stellar particles to their SPH neighbours according to the SPH kernel (for which we use the  $C^2$  kernel of Wendland 1995), with weights calculated using the initial, rather than current, mass of the particle (see Section 4.4 of ?). The transferred mass is ‘fixed’ to SPH particles and does not diffuse. Whilst the implementation of a subgrid metal diffusion scheme can increase the degree of mixing (??), such a scheme was not implemented in EAGLE because the appropriate diffusion coefficients

are not known *a priori*. To alleviate the symptoms of this suppressed mixing, gas particles also carry a kernel-smoothed measurement of each element abundance, which is updated at each active timestep (for a detailed discussion, see ?). Following the implementation of ?, smoothed abundances are used to compute, element-by-element, the rates of radiative cooling and heating of gas in the presence of the cosmic microwave background and the metagalactic UV background due to the galaxies and quasars, as modelled by ?. For the purposes of this calculation, the gas is assumed to be optically thin and in ionisation equilibrium. Stellar particles inherit the elemental abundances of their parent gas particle. Throughout, we present measurements using the smoothed abundances mentioned above. Despite the absence of element diffusion between particles, the mixing of particles with differing abundances is a form of diffusion that is modelled by our simulations, accessed via the use of smoothed abundances.

The simulations do not explicitly model the cold, dense phase of the ISM, and thus impose a temperature floor,  $T_{\text{eos}}(\rho)$ , to prevent spurious fragmentation within star-forming gas. The floor takes the form of an equation of state  $P_{\text{eos}} \propto \rho^{4/3}$  normalised so  $T_{\text{eos}} = 8000\text{K}$  at  $n_{\text{H}} = 0.1\text{cm}^{-3}$ . The temperature of star-forming gas therefore reflects the effective pressure of the ISM, rather than its actual temperature. Since the Jeans length of gas on the temperature floor is  $\sim 1\text{pkpc}$ , a drawback of its use is that it suppresses the formation of gaseous discs with vertical scale heights much shorter than this scale. However, as recently shown by ?, the vertical scale height of non-self-gravitating discs in EAGLE is primarily determined by turbulent pressure induced by gas accretion and energetic feedback. We comment further on the consequences of this limitation in Section 2.2.2.

### 2.2.2 Identification and characterisation of galaxies

Galaxies and their host haloes are defined by a two-step process. Haloes are identified by applying the FoF algorithm to the dark matter particle distribution, with a linking length of 0.2 times the mean interparticle separation. Gas, stars and BHs are assigned to the FoF group, if any, of their nearest dark matter particle. Bound substructure

within haloes, comprised of any particle type, is then identified using the SUBFIND algorithm (??). For each FoF halo, the subhalo comprising the most-bound particle is defined as the central subhalo, all other subhaloes are defined as satellites.

In general, unless stated otherwise, the properties of the ‘galaxy’ associated to a given subhalo are defined by aggregating the properties of the particles that are bound to the subhalo and also reside within a spherical aperture of radius  $r = 30\text{pkpc}$ , centred on the subhalo’s most-bound particle. For galaxies of the mass we examine here, this aperture mimics the 2-dimensional Petrosian aperture widely used in observational studies (see ?).

To characterise the morphology of EAGLE galaxies, we follow ? and compute the fraction of the kinetic energy of a galaxy’s stellar particles invested in ordered co-rotation with the disc:

$$\kappa_{\text{co}} = \frac{K_{\text{rot}}}{K} = \frac{1}{K} \sum_i^{r<30\text{pkpc}} \frac{1}{2} m_i \left( \frac{L_{Z,i}}{m_i R_i} \right)^2, \quad (2.2)$$

where  $m_i$  is the mass of the  $i^{\text{th}}$  particle,  $L_Z$  is the z-component of its angular momentum , and  $R$  is the cylindrical radius in the disc plane of the particle position with respect to the galaxy centre. ? show that a threshold of  $\kappa_{\text{co}} = 0.4$  broadly separates morphologically disc-like galaxies with blue intrinsic  $u-r$  colour, from redder, more elliptical galaxies.

Following ?, we use [O/Fe] as a proxy for [ $\alpha$ /Fe], since oxygen dominates the mass budget of  $\alpha$  elements. We use the common definition of abundance ratios [x/y] relative to solar values,

$$\left[ \frac{x}{y} \right] = \log_{10} \left( \frac{X^x}{X^y} \right) - \log_{10} \left( \frac{X_\odot^x}{X_\odot^y} \right), \quad (2.3)$$

where  $(x, y)$  each represent an element and  $X^x$  = denotes the galaxy stellar mass fraction comprised by element x. We adopt the solar mass fractions of ?, who report  $X_\odot^{\text{O}}/X_\odot^{\text{Fe}} = 4.76$  and  $X_\odot^{\text{Fe}}/X_\odot^{\text{H}} = 0.0011$ .

### Defining the stellar populations of galaxy discs

To facilitate a like-for-like comparison of elemental abundances inferred from Galactic surveys with those of simulated galaxies broadly similar to the Milky Way, we construct samples of galaxies with present day stellar mass in the interval  $M_\star = (5 - 7) \times 10^{10} M_\odot$ , broadly similar to the value of  $\simeq 6 \times 10^{10} M_\odot$  estimated for the Galaxy (e.g. ??), that are also disc-dominated ( $\kappa_{co} > 0.4$ ). These criteria are satisfied by 133 galaxies in Ref-L100N1504, and 5 in Ref-L025N0376. The mean stellar half mass radius of galaxies comprising this ‘Milky Way-like’ sample in Ref-L100N1504 is  $R_{1/2} \simeq 7.5 \text{ pkpc}$ , consistent with the average  $r$ -band scale length of external disc galaxies in SDSS,  $R_{1/2} = 5.7 \pm 1.9 \text{ kpc}$ , reported by ?.

We mimic, crudely, the selection function of Galactic surveys such as Gaia-ESO and APOGEE by considering only those stellar particles within a cylindrical annulus, centred on the most-bound particle of the galaxy, with inner and outer radii equal to half and twice the stellar half mass radius (of the individual galaxy), respectively, and upper and lower vertical bounds of  $\pm$  one quarter of the stellar half mass radius. This selects roughly  $10^4$  particles per galaxy. Throughout, unless otherwise stated, we define ‘disc stars’ as the stellar particles bound to ‘Milky Way-like’ galaxies, satisfying this geometric constraint. No kinematic constraints are applied to the stellar particles. We do not dissect the  $[\alpha/\text{Fe}]\text{-}[\text{Fe}/\text{H}]$  distribution into radial and vertical bins since, for reasons articulated in Section 2.2.1, the scale heights of the young and old disc stellar populations are necessarily more similar in the simulations than is observed by Galactic surveys.

## 2.3 The elemental abundances of disc stars in Milky Way-like galaxies

In this section, we examine the distribution, in the  $[\alpha/\text{Fe}]\text{-}[\text{Fe}/\text{H}]$  plane, of the disc stars of Milky Way-like galaxies, and explore the relationship between this distribution

and the underlying properties of the stellar population. We refrain from performing a detailed comparison of the  $[\alpha/\text{Fe}]\text{-}[\text{Fe}/\text{H}]$  distribution with those recovered from surveys of the Galaxy's stellar populations, since our aim is to understand the origin of the trends in the distribution, rather than to reproduce the observed distribution precisely. Predictions from models, and inferences from observations, of absolute (as opposed to relative) abundances are subject to systematic uncertainties of a factor  $\gtrsim 2$ . The uncertainties stem primarily from theoretical uncertainties in nucleosynthetic yield calculations (see e.g. Appendix A of ?, and references therein), the calibration of observational abundance indicators (e.g. ?), statistical and systematic uncertainties in the measurement of the volumetric Type Ia SNe rate (e.g. ???), and an incomplete understanding of the nature of Type Ia SNe progenitors and their delay-time distribution (see, e.g. ?). In Appendix 2.7, we show the effect on the  $[\alpha/\text{Fe}]\text{-}[\text{Fe}/\text{H}]$  distribution of varying the subgrid parameters governing the number of Type Ia SNe per unit stellar mass formed, and their e-folding timescale. There, we show that the distribution can change significantly in response to reasonable variation of these parameters.

### 2.3.1 The distribution of disc stars on the $[\alpha/\text{Fe}]\text{-}[\text{Fe}/\text{H}]$ plane

Fig. 2.1 shows the  $[\alpha/\text{Fe}]\text{-}[\text{Fe}/\text{H}]$  distribution of the 1.5 million stellar particles comprising the disc populations (see Section 2.2.2) of the 133 present-day Milky Way-like galaxies in Ref-L100N1504 as a 2-dimensional histogram. The pixels of the histogram represent bins of 0.05 in  $\Delta[\alpha/\text{Fe}]$  and  $\Delta[\text{Fe}/\text{H}]$ , and the value of each pixel is weighted by the current (rather than initial) mass of the stellar particles within. The overplotted filled line represents the median  $[\alpha/\text{Fe}]$  calculated in bins of  $\Delta[\text{Fe}/\text{H}] = 0.2$ , and the dashed lines show the interquartile range. As has been observed by Galactic surveys, and is commonly predicted by analytic and numerical Galactic chemical evolution models, the primary trend is that of a sequence with declining  $[\alpha/\text{Fe}]$  as a function of  $[\text{Fe}/\text{H}]$ , with a relatively shallow negative gradient at low  $[\text{Fe}/\text{H}]$  and steeper gradient at higher  $[\text{Fe}/\text{H}]$ . The distribution of  $[\alpha/\text{Fe}]$  at fixed  $[\text{Fe}/\text{H}]$  is unimodal, with a broad dispersion. The median  $[\alpha/\text{Fe}]$  declines gradually from 0.57 at  $[\text{Fe}/\text{H}] = -1.0$  to  $\simeq 0.47$  at  $[\text{Fe}/\text{H}] = -0.5$ , then declines more rapidly to  $[\alpha/\text{Fe}] \simeq 0.07$  at  $[\text{Fe}/\text{H}] = 0.5$ .

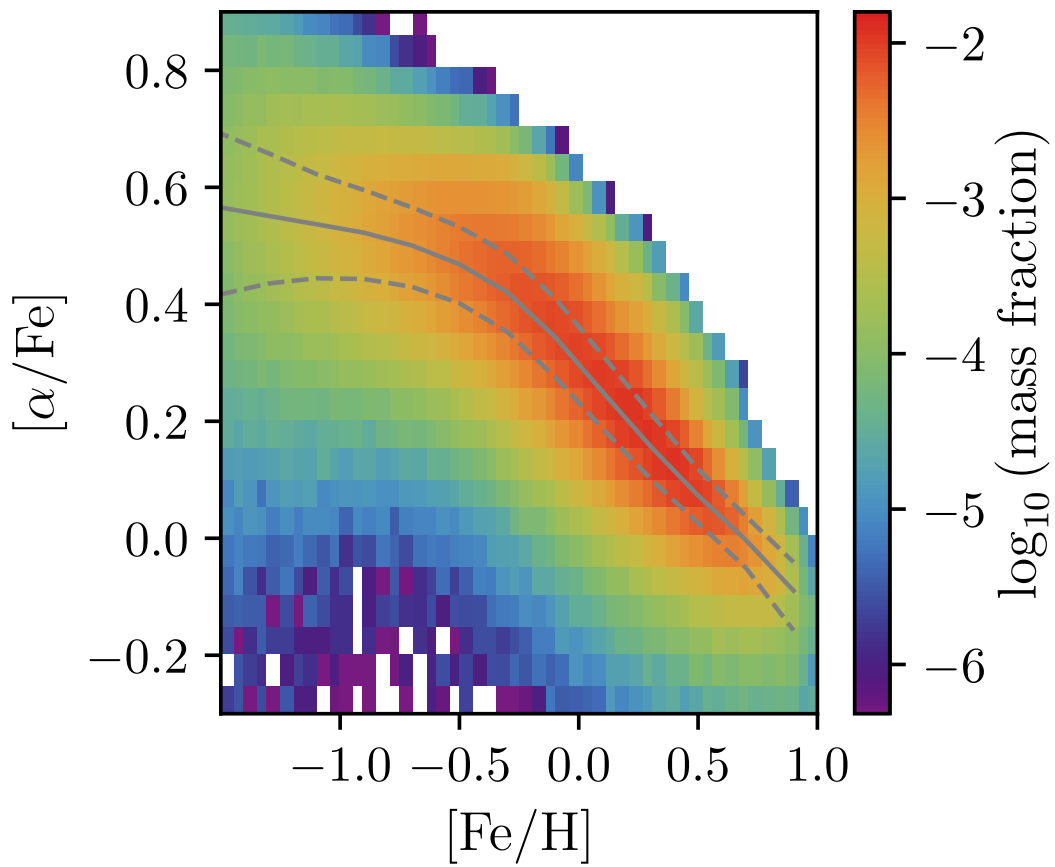


Figure 2.1: Two-dimensional histogram of the mass-weighted  $[\alpha/\text{Fe}]$ - $[\text{Fe}/\text{H}]$  distribution of all ‘disc stars’ associated with the 133 galaxies identified as broad analogues of the Milky Way in terms of their stellar mass and morphology (see Section 2.2.2) at  $z = 0$  in Ref-L100N1504. The overplotted solid line shows the median  $[\alpha/\text{Fe}]$  in bins of  $\Delta[\text{Fe}/\text{H}] = 0.2$ , dashed lines show the interquartile range.

The  $1\sigma$  scatter in  $[\alpha/\text{Fe}]$  is approximately 0.41 at  $[\text{Fe}/\text{H}] = -1.0$ , and narrows to 0.14 at  $[\text{Fe}/\text{H}] = 0.5$ . The increased scatter at low  $[\text{Fe}/\text{H}]$  is likely a consequence of poor sampling of the enrichment process.

We next turn to an examination of the underlying properties of the disc stars, to elucidate the origin of the distribution shown in Fig. 2.1. The common interpretation for the diversity of  $[\alpha/\text{Fe}]$  in the Galaxy's disc stars is a varying relative contribution of Type Ia and Type II SNe ejecta to the Fe abundance of each star. This fraction is tracked explicitly by the simulations, enabling this hypothesis to be tested directly. We examine the same sample of stellar particles shown in Fig. 2.1, and show in Fig. 2.2 the mean mass fraction of their Fe that was synthesised by Type Ia SNe,  $f_{\text{Fe,SNIa}}$ , as a function of their position in  $[\alpha/\text{Fe}]\text{-}[\text{Fe}/\text{H}]$  space. The mean fraction of each pixel is computed weighting by the current mass of its contributing stellar particles. The mass distribution shown in Fig. 2.1 is illustrated here with overlaid contours, the outer and inner contours corresponding to  $\log_{10}$  (mass fraction) =  $-3.5$  and  $-2.5 \text{ pixel}^{-1}$ , respectively. Only well sampled pixels, with  $\log_{10}$  (mass fraction)  $> -4.5 \text{ pixel}^{-1}$ , corresponding to approximately 50 stellar particles, are shown.

As one might expect, there is a broad anti-correlation between  $[\alpha/\text{Fe}]$  and  $f_{\text{Fe,SNIa}}$ . According to our simulations the majority of the Fe locked into disc stars with  $[\alpha/\text{Fe}] \gtrsim 0.5$  was synthesised by Type II SNe, with the mass fraction synthesised in Type Ia SNe being typically  $< 0.2$ . Conversely, in stars with subsolar  $[\alpha/\text{Fe}]$ , which typically exhibit supersolar  $[\text{Fe}/\text{H}]$ , the mass fraction of Fe synthesised by Type Ia SNe can be  $\simeq 0.8$ . There is also a weaker, but significant trend at fixed  $[\alpha/\text{Fe}]$  ( $\lesssim 0.2$ ), such that stars with higher  $[\text{Fe}/\text{H}]$  have a smaller Fe contribution from Type Ia SNe. Enrichment of gas by Type II SNe increases  $[\text{Fe}/\text{H}]$  at broadly fixed  $[\alpha/\text{Fe}]$  (a shift to the right in the  $[\alpha/\text{Fe}]\text{-}[\text{Fe}/\text{H}]$  plane) if enrichment by Type Ia is negligible, or whilst increasing  $[\alpha/\text{Fe}]$  (a shift up and to the right) if Type Ia enrichment is significant. Enrichment of Type Ia SNe tends to increase  $[\text{Fe}/\text{H}]$  whilst decreasing  $[\alpha/\text{Fe}]$  (a shift down and to the right). Therefore, greater  $[\text{Fe}/\text{H}]$  at fixed  $[\alpha/\text{Fe}]$  is typically due to the more Fe-rich stars sourcing a greater fraction of their Fe from Type II SNe relative to Type Ia SNe.

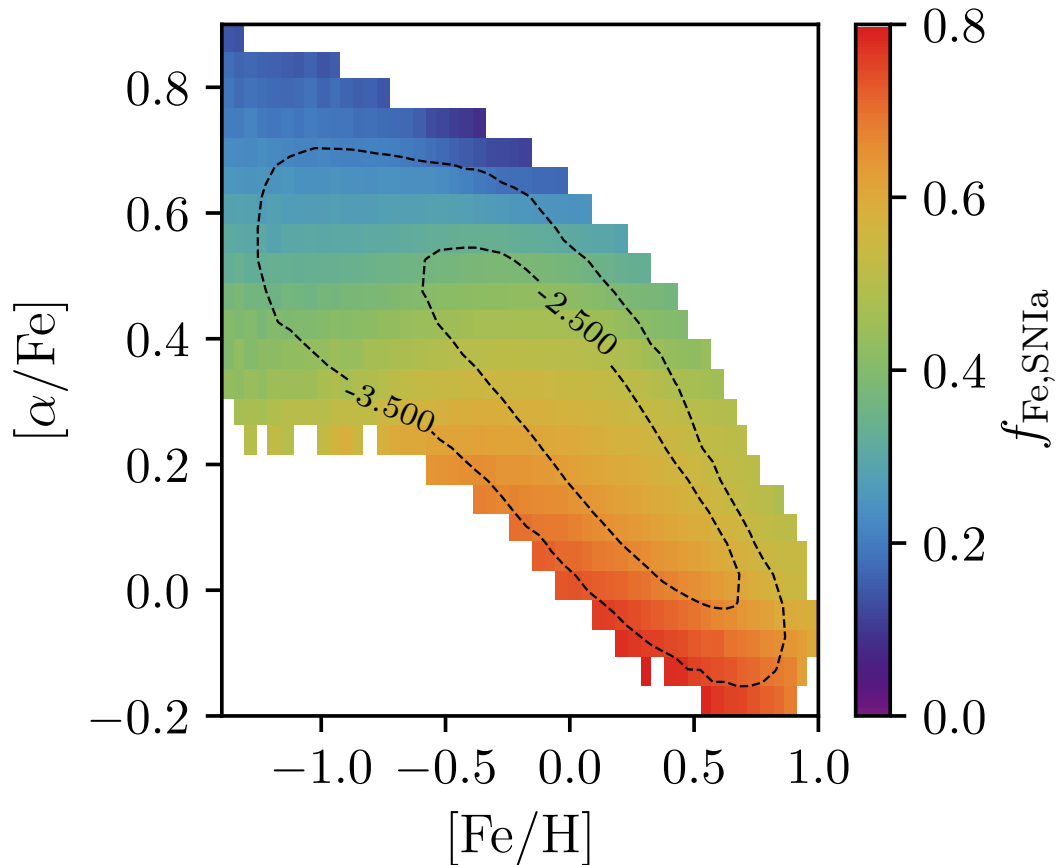


Figure 2.2: The mean mass fraction of the Fe, locked up in the disc stars of present-day Milky Way-like galaxies in Ref-L100N1504, that was synthesised by Type Ia SNe. The fraction is shown as a function of the stellar populations’ position in  $[\alpha/\text{Fe}]$ - $[\text{Fe}/\text{H}]$  space. The value in each pixel is weighted by the current mass of the stellar particles within. Overplotted contours reproduce the mass distribution shown in Fig. 2.1. The Type Ia SNe Fe fraction broadly anti-correlates with  $[\alpha/\text{Fe}]$ , and at fixed  $[\alpha/\text{Fe}]$  the Fe mass fraction contributed by Type Ia SNe is greatest in Fe-poor stars.

Analytic models posit that high-[ $\alpha$ /Fe] stellar populations form in the early life of a galaxy, and do so rapidly, such that there is little opportunity for the enrichment of star-forming gas by the delayed release of Type Ia SNe ejecta. ? show that this is the case for the galaxy-averaged  $\alpha$ -enhancement of massive EAGLE galaxies, whose stars form rapidly at early times prior to quenching by AGN feedback. To examine whether the same applies in Milky Way-like galaxies, we plot in Fig. 2.3 the mean age of stellar particles as a function of their position in [ $\alpha$ /Fe]-[Fe/H] space, and in Fig. 2.4 the mean consumption timescale<sup>1</sup> of the natal gas,  $t_g = \Sigma_g / \dot{\Sigma}_*$ , where  $\Sigma_g$  is the gas surface density and  $\dot{\Sigma}_*$  is the star formation rate (SFR) per unit area. As in previous plots, the pixel values are weighted by the current mass of the stellar particles within, and overlaid contours represent the mass distribution shown in Fig. 2.1.

The consumption timescale provides an estimate of the period of time a parcel of star-forming gas resides in the ISM, during which it can be enriched by the ejecta of neighbouring stellar populations. It is likely that  $t_g$  overestimates the time spent in the ISM by a star-forming particle, since it only considers the regulation of the gas surface density by star formation, thus neglecting the influence of feedback. On average,  $\langle N_{\text{heat}} \rangle \simeq 1$  SPH particle is stochastically heated by the stellar feedback accompanying the formation of each stellar particle, and these particles can entrain neighboring particles in outflows. Outflows can also be driven by AGN feedback, so the accuracy of this estimate is likely poorer than a factor of  $\simeq 2$ . Nonetheless,  $t_g$  remains an instructive diagnostic for our purposes. To compute it, we follow ? and assume that the scale height of star-forming gas discs is comparable to the local Jeans length,  $L_J$ , such that  $\Sigma_g \simeq \rho_g L_J$ , and then relate the consumption timescale of star-forming gas to its pressure:

$$t_g = A^{-1} (1 \text{ M}_\odot \text{ pc}^{-2})^n \left( \frac{\gamma}{G} f_g P_* \right)^{(1-n)/2}. \quad (2.4)$$

Here,  $\gamma = 5/3$  is the ratio of specific heats for an ideal gas, and  $f_g$  is the local gas fraction, which we assume to be unity. The parameters  $A$  and  $n$  are specified by observations, i.e. the Kennicutt-Schmidt scaling relation. We use  $A = 1.515 \times$

---

<sup>1</sup>The inverse of the consumption timescale is often referred to as the ‘star formation efficiency’ in the chemical evolution modelling literature.

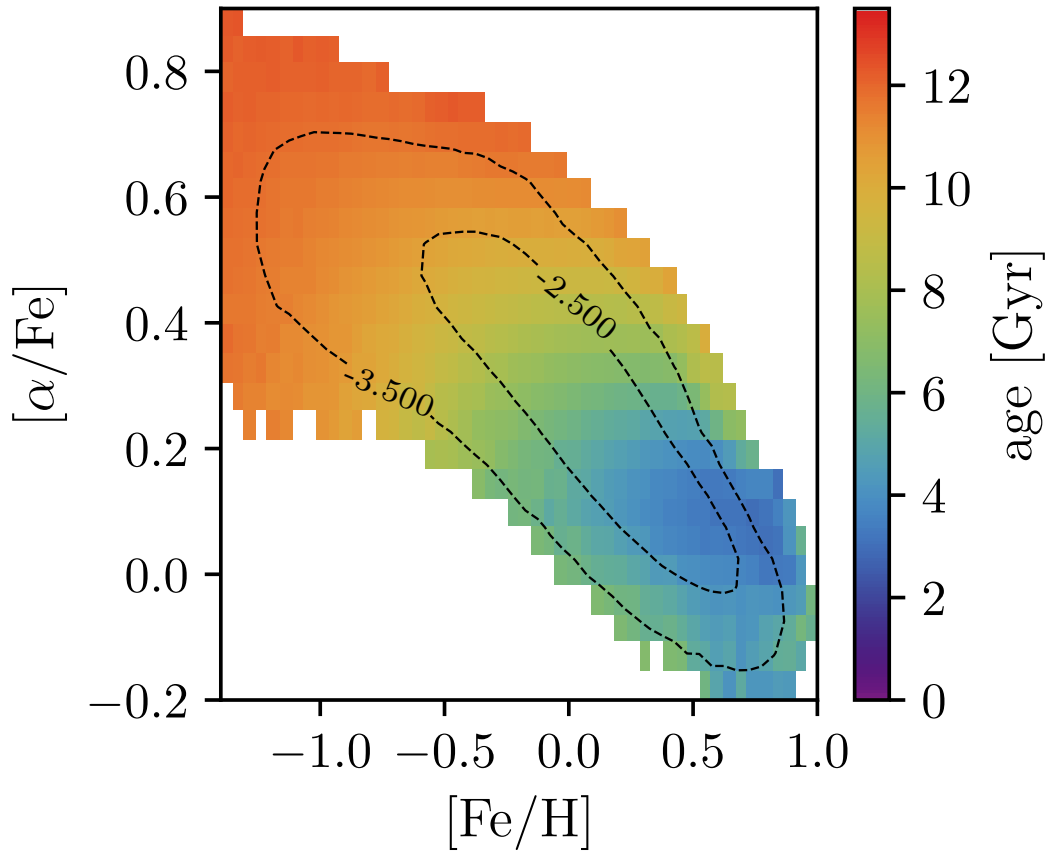


Figure 2.3: The mean age of the disc stars of present day Milky Way-like galaxies in Ref-L100N1504, as a function of their position in  $[\alpha/\text{Fe}]$ - $[\text{Fe}/\text{H}]$  space. Pixel values are weighted by the current mass of the stellar particles within, and the overplotted contours reproduce the mass distribution shown in Fig. 2.1. Age correlates with  $[\alpha/\text{Fe}]$ , though at any fixed  $[\alpha/\text{Fe}]$  disc stars exhibit a broad range of mean ages, depending on their  $[\text{Fe}/\text{H}]$ . At fixed  $[\text{Fe}/\text{H}]$ , the most  $\alpha$ -rich stellar populations tend to be the oldest.

$10^{-4} M_{\odot} \text{ yr}^{-1} \text{ kpc}^{-2}$  and  $n = 1.4$ , with the former being a factor of 1.65 lower than the value specified by ?, since we assume a Chabrier, rather than Salpeter, IMF. For the purposes of the calculation, the pressure of the natal gas,  $P_*$ , is assumed to be that specified by the temperature floor described in Section 2.2.1, i.e.  $P_* = P_{\text{eos}}(\rho_*)$ , where  $\rho_*$  is the density of the natal gas at the instant it is converted into a stellar particle.

Fig. 2.3 shows that, as expected, there is a strong correlation between the present-day age of stellar populations, and their position in  $[\alpha/\text{Fe}]$ - $[\text{Fe}/\text{H}]$  space. The characteristic age of Fe-poor ( $[\text{Fe}/\text{H}] \lesssim -0.5$ ),  $\alpha$ -rich ( $[\alpha/\text{Fe}] \gtrsim 0.4$ ) stars is greater than 10 Gyr, corresponding to a formation redshift of  $z \gtrsim 1.7$ , whilst those with solar or supersolar iron abundance, for which  $[\alpha/\text{Fe}] \lesssim 0.2$ , are typically younger than 5 Gyr ( $z_{\text{form}} \lesssim 0.5$ ). There is a clear preference for  $\alpha$ -rich stars to be old, but disc stars can exhibit a broad range of ages at fixed  $[\alpha/\text{Fe}]$ , such that there is not a direct mapping between age and  $f_{\text{Fe,SNIa}}$ . This notwithstanding, at any fixed value of  $[\text{Fe}/\text{H}]$ , the stars richest in  $\alpha$  elements generally tend to be the oldest.

Fig. 2.4 reveals a striking trend, clearly highlighting that at fixed  $[\text{Fe}/\text{H}]$  the most  $\alpha$ -rich populations form from gas that exhibits the shortest consumption timescales. As the dynamic range is narrow for  $t_g \gtrsim 1$  Gyr, we adopt a linear scaling of colour with  $t_g$ . The plot illustrates clearly that the reason the release of ejecta from Type Ia SNe is able to influence the  $[\alpha/\text{Fe}]$  of stellar populations at fixed  $[\text{Fe}/\text{H}]$  is the fact that the gas consumption timescales are of the same order as the characteristic e-folding timescale of the Type Ia SNe delay time distribution. Although gas can be enriched at densities below the star formation density threshold (whence  $t_g$  is infinite), the clear connection between  $t_g$  and (in particular)  $[\alpha/\text{Fe}]$  highlights that, for most stellar particles, the bulk of their enrichment must take place whilst they comprise the star-forming ISM. The e-folding timescale of  $\tau = 2$  Gyr adopted by the Reference model corresponds to a ‘halflife’ of  $t_{1/2} = \tau \ln(2) = 1.4$  Gyr. The adoption of a shorter (longer) e-folding timescale results in the advancement (delay) of the release of Fe synthesised by Type Ia SNe, thus inhibiting (promoting) the formation of disc stars with high  $[\alpha/\text{Fe}]$ .

The majority ( $\gtrsim 85$  percent) of stellar particles formed from gas with consumption times  $\gtrsim 1$  Gyr, but those that formed more rapidly were largely precluded from en-

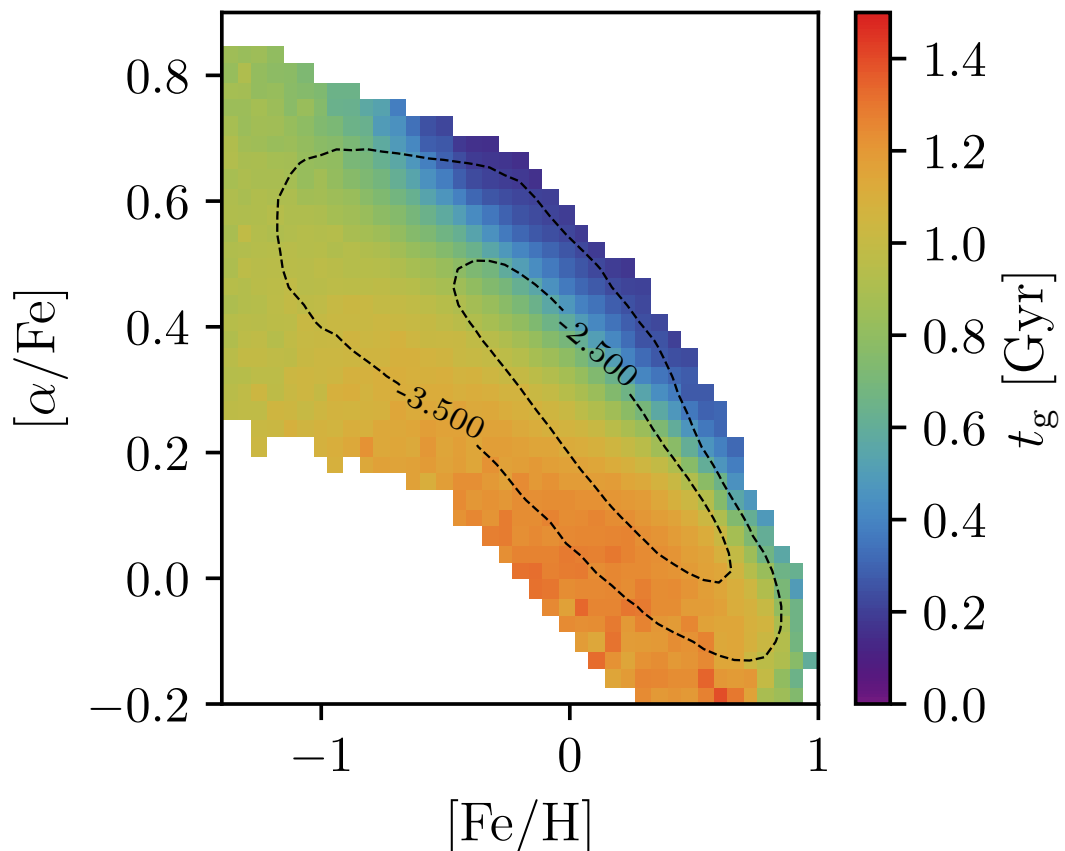


Figure 2.4: The mean gas consumption timescale  $t_g$  of the natal gas from which the disc stars of present-day Milky Way-like galaxies in Ref-L100N1504 formed, as a function of their position in  $[\alpha/\text{Fe}]\text{-}[\text{Fe}/\text{H}]$  space. Pixel values are weighted by the current mass of the stellar particles within, and the overplotted contours reproduce the mass distribution shown in Fig. 2.1. At fixed  $[\text{Fe}/\text{H}]$ , the most  $\alpha$ -rich stellar particles formed from gas with the shortest consumption timescales.

Table 2.1: Basic properties of the three present-day galaxies shown in Figure 2.5. The rows correspond to, respectively: the labels applied to each galaxy in the text, their Galaxy ID and FOF ID in public EAGLE galaxy catalogues, their stellar mass, halo mass, their specific star formation rate (sSFR), their  $\kappa_{\text{co}}$  value, and their half-mass radius.

Label	A	B	C
Galaxy ID	16850421	16925427	16921468
FOF ID	507	527	526
$M_*$	5.18	5.80	6.52
$M_{200}$	2.32	2.92	3.41
sSFR	4.74	5.14	1.85
$\kappa_{\text{co}}$	0.67	0.45	0.46
$r_{1/2}$	8.83	9.49	3.00
			[kpc]

richment by the Type Ia SNe of recently-formed, nearby stellar populations. We note that the  $t_g$  distribution on the  $[\alpha/\text{Fe}]\text{-}[\text{Fe}/\text{H}]$  plane does not map directly onto that of the distribution of  $f_{\text{Fe,SNIa}}$  shown in Fig. 2.2. This is because short consumption timescales are realised within gas-rich overdensities at early epochs, and also within massive, metal-rich galaxies at later times.

### 2.3.2 Galaxy-to-galaxy diversity of $\alpha$ -enrichment

Having examined the distribution of stars in  $[\alpha/\text{Fe}]\text{-}[\text{Fe}/\text{H}]$  space, in a collective sense, for the present-day Milky Way analogues identified in Ref-L100N1504, we now examine the galaxy-to-galaxy diversity of the  $[\alpha/\text{Fe}]\text{-}[\text{Fe}/\text{H}]$  distribution. This exercise enables a first assessment of how common among other present-day disc galaxies is the observed distribution in the  $[\alpha/\text{Fe}]\text{-}[\text{Fe}/\text{H}]$  plane of the Milky Way’s disc stars.

The present-day  $[\alpha/\text{Fe}]\text{-}[\text{Fe}/\text{H}]$  distributions of the sample of 133 EAGLE galaxies exhibit significant diversity. Based on visual inspection, we have broadly classified the galaxies into the following categories, with the occupancy of each category in parentheses: unimodal with low- $[\alpha/\text{Fe}]$  (82), unimodal with high- $[\alpha/\text{Fe}]$  (19), broad  $[\alpha/\text{Fe}]$  at fixed  $[\text{Fe}/\text{H}]$  (10), ambiguous (22). The sample is therefore dominated by galaxies that exhibit a single, broadly continuous ‘sequence’ that is (unsurprisingly) similar to the overall trend revealed in Fig. 2.1. A handful of single-sequence galaxies track the upper envelope of the stacked distribution and might reasonably be considered

analogous to the stellar populations comprising the high-[ $\alpha$ /Fe] sequence observed in the Galaxy. Six of the 10 galaxies categorised as having broad [ $\alpha$ /Fe] at fixed [Fe/H] in fact exhibit a clear bimodality in [ $\alpha$ /Fe] at fixed [Fe/H], and might be considered, somewhat subjectively, as qualitatively similar to the Galaxy. The sample also includes systems with complex abundance distributions that in some cases are indicative of a recent merger with a gas-rich companion, for example where [ $\alpha$ /Fe] exhibits a positive correlation with [Fe/H] over a narrow range.

To illustrate the diversity of the [ $\alpha$ /Fe]-[Fe/H] distributions, we identify three representative examples: a galaxy exhibiting a single low-[ $\alpha$ /Fe] sequence, a galaxy exhibiting bimodality in [ $\alpha$ /Fe] at fixed [Fe/H], and a galaxy exhibiting a single, high-[ $\alpha$ /Fe] sequence. Key properties of these galaxies, labelled A, B and C, respectively, are given in Table 2.1. From top to bottom these are, respectively, the FOF halo identifier of the galaxy in the EAGLE public database<sup>2</sup> (?); its stellar mass,  $M_*$ ; its virial mass,  $M_{200}$ , defined as the total mass (in gas, stars, BHs and dark matter) enclosed by a sphere of radius  $R_{200}$ , centred on the galaxy's most bound particle, within which the mean enclosed density is 200 times the critical density,  $\rho_c \equiv 3H^2/8\pi G$ ; the specific star formation rate of the galaxy,  $\dot{M}_*/M_*$ ; its median kinetic energy in ordered rotation,  $\langle \kappa \rangle$ ; and its stellar half-mass radius,  $R_{1/2}$ .

The columns of Fig. 2.5, from left to right respectively, show further properties of A, B and C. The two upper rows show images of the galaxies at  $z = 0$  with a  $50 \times 50$  kpc field of view, in face-on and edge-on orientation, defined such that the disc plane is orthogonal to the angular momentum axis of the stellar particles within 30 kpc of the most-bound particle. The images were extracted from the EAGLE public database, and were created using the techniques described by ?. The third row presents the [ $\alpha$ /Fe]-[Fe/H] distribution of the disc stars, shown as a mass-weighted 2-dimensional histogram. The dashed diagonal line is an arbitrary threshold chosen to separate the high- and low-[ $\alpha$ /Fe] sequences, which enables the contribution to the star formation history of the particles comprising each sequence to be shown separately in the bottom row. The downward arrows denote the epoch by which half of the stellar particles

---

<sup>2</sup><http://galaxy-catalogue.dur.ac.uk>

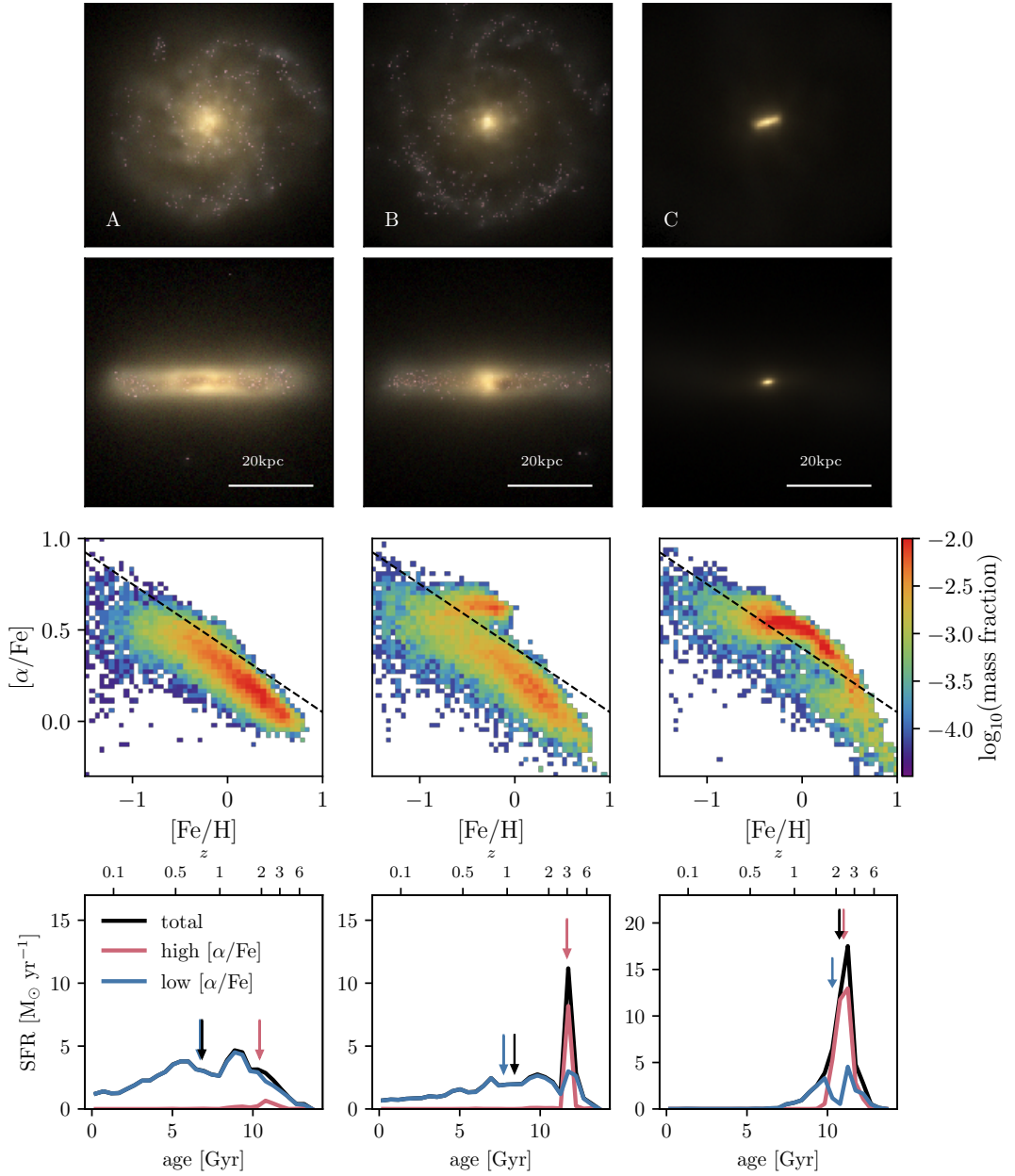


Figure 2.5: Examples illustrating the diversity of the  $[\alpha/\text{Fe}]$ -[Fe/H] distribution of disc stars from present-day galaxies in Ref-L100N1504. From left to right, the columns correspond to the galaxies labelled A, B and C in the text, for which key properties are quoted in Table 2.1. The two upper rows show mock images of the galaxies, with a  $50 \times 50$  kpc field of view, in the face-on and edge-on orientations. The images show the stellar light based on the combination of monochromatic  $u$ -,  $g$ - and  $r$ -band SDSS filters. The third row shows the  $[\alpha/\text{Fe}]$ -[Fe/H] plane of the disc stars, with the dashed diagonal line positioned to broadly separate the high- and low- $[\alpha/\text{Fe}]$  sequences. This separation enables, in the bottom row, the contribution to the total (black) star formation history of the stars comprising the high- (red) and low- $[\alpha/\text{Fe}]$  (blue) sequences to be shown. Downward arrows denote the epoch by which half of the stellar particles comprising these populations formed.

comprising the populations formed.

Galaxies A and B exhibit a classical structure, with a central red spheroid surrounded by an extended blue disc. The spheroid of galaxy A is relatively diffuse, whilst that of galaxy B is more massive and more compact. Galaxy C is dominated by a central, rapidly-rotating elongated spheroid, and is an example of the relatively rare cases for which a high value of  $\langle \kappa \rangle$  does not correspond to a morphologically-extended disc (see ?). The bulk of galaxy A's disc stars form a continuous sequence in  $[\alpha/\text{Fe}]\text{-}[\text{Fe}/\text{H}]$  space, at a relatively low value of  $[\alpha/\text{Fe}]$ , extending to  $[\text{Fe}/\text{H}] \simeq 0.8$ . A similar sequence is visible in the case of galaxy B, extending almost to  $[\text{Fe}/\text{H}] \simeq 1$ . This low- $[\alpha/\text{Fe}]$  sequence is supplemented by an  $\alpha$ -rich ( $[\alpha/\text{Fe}] \simeq 0.65$ ) sequence that extends to  $[\text{Fe}/\text{H}] \simeq 0$ . Galaxy C is dominated by a high- $[\alpha/\text{Fe}]$  sequence that is approximately constant at  $[\alpha/\text{Fe}] \simeq 0.6$  until  $[\text{Fe}/\text{H}] \simeq 0$ , and gradually declines as a function of increasing  $[\text{Fe}/\text{H}]$ . A small fraction of galaxy C's disc stars populate a region of  $[\alpha/\text{Fe}]\text{-}[\text{Fe}/\text{H}]$  space similar to galaxy B's low- $[\alpha/\text{Fe}]$  sequence at the highest values of  $[\text{Fe}/\text{H}]$ .

The formation histories of the stars comprising the sequences offer clues to the latter's origin. Galaxy A exhibits an extended star formation history that evolves smoothly between values of  $1 - 5 M_{\odot} \text{ yr}^{-1}$ . This history is consistent with relatively long consumption timescales ( $\gtrsim 1$  Gyr), and yields a relatively young stellar disc (an initial mass-weighted mean age of 7 Gyr). The low- $[\alpha/\text{Fe}]$  component of galaxy B behaves similarly, albeit at a slightly lower SFR than galaxy A. The formation of galaxy B's high- $\alpha$  component dominates the early stages of its disc formation, and during this period of rapid star formation the SFR peaks at  $\dot{M}_{\star} > 10 M_{\odot} \text{ yr}^{-1}$ . The stars comprising this sequence therefore formed with an initial mass-weighted mean consumption time of  $t_g \simeq 200$  Myr. Nearly all of the stellar particles comprising the high- $[\alpha/\text{Fe}]$  sequence are formed during this episode. The formation of galaxy C is similar to the early behaviour of galaxy B, albeit more extreme. The massive, concentrated spheroid forms in a single, extended episode of rapid star formation during which the SFR peaks at  $\dot{M}_{\star} \simeq 17 M_{\odot} \text{ yr}^{-1}$ , yielding a initial mass-weighted mean consumption time of  $t_g \simeq 180$  Myr.

The star formation histories of these examples therefore corroborate the broad picture inferred from inspection of Figs. 2.2, 2.3 and 2.4: high values of  $[\alpha/\text{Fe}]$  are realised by stellar populations with only a small fraction of their Fe mass synthesised by Type Ia SNe. Such populations are typically formed at early cosmic epochs, from gas with  $t_g < \tau$ . This close connection between the star formation history and the distribution of stars in the  $[\alpha/\text{Fe}]$ - $[\text{Fe}/\text{H}]$  plane highlights that the former could be ‘reverse engineered’ by applying analytic chemical evolution models to measurements of the latter, but the conclusions drawn from such an exercise might not be generally applicable to the broader population of galaxies with similar mass and morphology.

## 2.4 The origin of the $[\alpha/\text{Fe}]$ - $[\text{Fe}/\text{H}]$ distribution of disc stars

In this section we examine the evolution of the gas from which the stellar populations occupying specific regions of the  $[\alpha/\text{Fe}]$ - $[\text{Fe}/\text{H}]$  plane formed. We also examine the subsequent radial migration of these populations within the disk. We begin by analysing a single galaxy, and generalise the analysis to the broader population in Section 2.4.1.

The Lagrangian nature of the EAGLE simulations enables us to reconstruct the full enrichment history of the gas from which disc stars formed. It is therefore instructive to examine the evolution of the elemental abundances of the ‘natal’ gas of the stars occupying key positions in the  $[\alpha/\text{Fe}]$ - $[\text{Fe}/\text{H}]$  plane at  $z = 0$ . Although, as discussed in Section 2.2.1, the mass and metals donated by stellar particles to SPH particles are ‘fixed’ to particles and do not diffuse between them, any dilution of elemental abundances resulting from the inflow of low-metallicity gas can nonetheless be captured, since we examine kernel-smoothed abundances. In order to examine enrichment histories with superior temporal resolution to that afforded by the standard set of EAGLE snapshots, we focus here on the Ref-L025N0376 simulation, for which 1000 snapshots were recorded. One of the galaxies that forms in this simulation is, at  $z = 0$ , a disc-

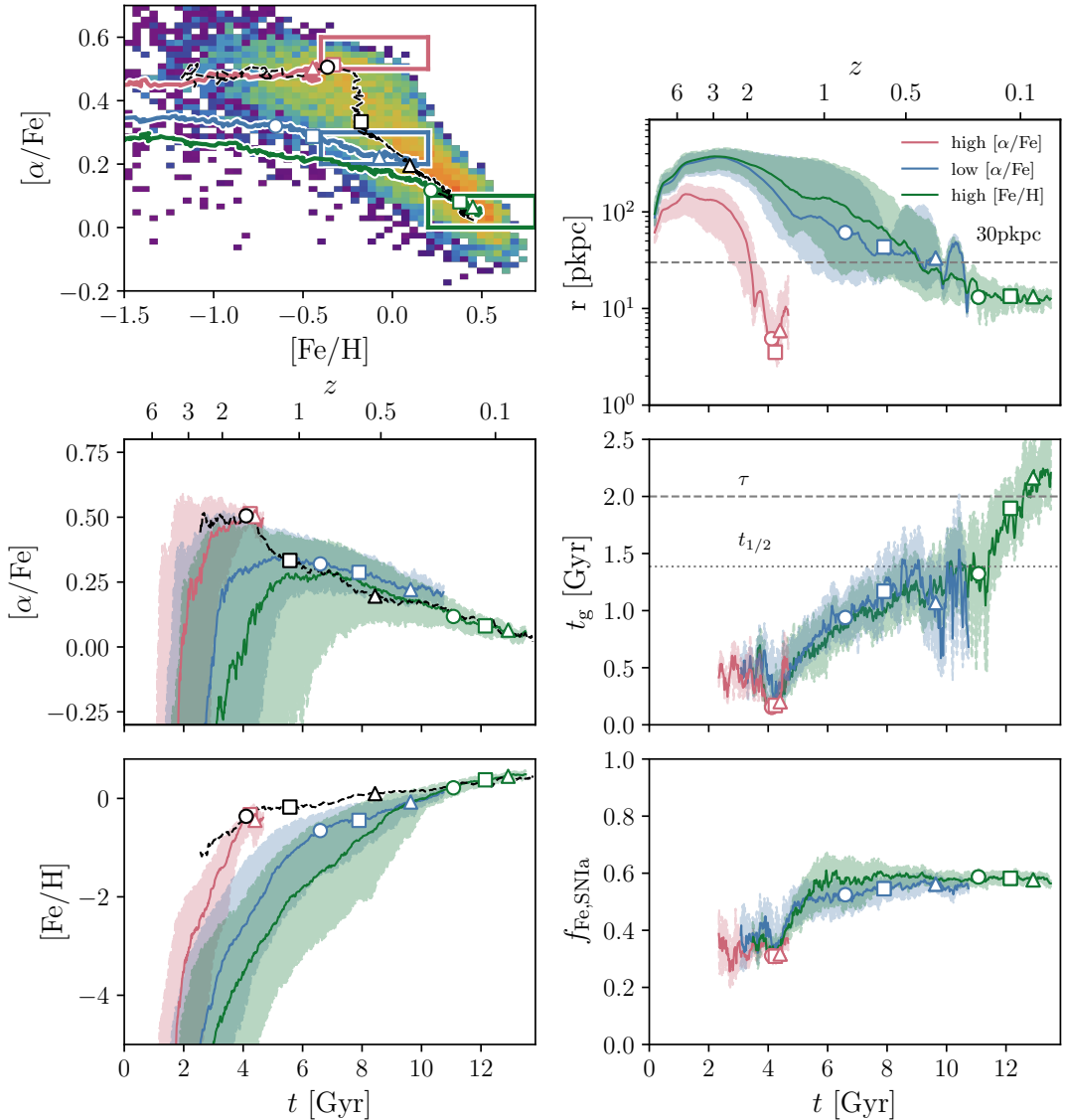


Figure 2.6: The enrichment history of the natal gas of disc stars occupying selected regions of the  $z = 0$   $[\alpha/\text{Fe}]$ - $[\text{Fe}/\text{H}]$  plane, for the galaxy discussed in Section 2.4. The upper-left panel shows the mass distribution of stars in the  $[\alpha/\text{Fe}]$ - $[\text{Fe}/\text{H}]$  plane. Particle selections corresponding to "high- $[\alpha/\text{Fe}]$ ", "low- $[\alpha/\text{Fe}]$ " and "high- $[\text{Fe}/\text{H}]$ " are denoted by the overlaid red, blue and green boxes, respectively. Overlaid coloured tracks denote the evolution of the median abundances of the natal gas of these populations, with circle, square and triangle symbols corresponding to the epochs at which 25, 50 and 75 percent of the gas has been consumed, respectively. The evolution of the median  $[\alpha/\text{Fe}]$  and  $[\text{Fe}/\text{H}]$  is plotted as a function of cosmic time in the centre-left and lower-left panels, respectively. Shaded regions on these panels denote the interquartile range. Dashed black tracks on the panels of the left-hand column denotes the SFR-weighted median gas-phase abundances. The upper-right panel shows the evolving median and interquartile range of the galactocentric radii (in proper coordinates) of the natal gas of each population. The centre-right panel shows the SFR-weighted mean consumption time of the natal gas, and the bottom-right panel shows the SFR-weighted mean of the natal gas mass fraction of Fe that was synthesised by Type Ia SNe. For these two panels, the shaded regions denote the  $1\sigma$  scatter about the mean.

dominated ( $\kappa_{\text{co}} = 0.58$ ,  $r_{1/2} = 8.8$  kpc) central galaxy that exhibits  $[\alpha/\text{Fe}]$  bimodality at fixed  $[\text{Fe}/\text{H}]$ . Its stellar mass is  $M_* = 4.58 \times 10^{10}\text{M}_\odot$ , slightly below the lower bound of the mass interval used in Section 2.2.2 to define the Ref-L100N1504 sample, but this galaxy is a useful example owing to the similarity of its star formation history and elemental abundances with those of galaxy B. Its present-day halo mass is  $M_{200} = 2.54 \times 10^{12}\text{M}_\odot$ .

Fig. 2.6 summarises the enrichment history of this galaxy. The upper-left panel shows the  $[\alpha/\text{Fe}]\text{-}[\text{Fe}/\text{H}]$  distribution of the galaxy's present-day disc stars as a 2-dimensional histogram. The overlaid boxes define three populations of stellar particles, for which we reconstruct the enrichment history of their natal gas particles. The boxes span  $\Delta[\text{Fe}/\text{H}] = 0.6$  and  $\Delta[\alpha/\text{Fe}] = 0.1$ , and the red and blue cases, respectively, correspond to high- $[\alpha/\text{Fe}]$  and low- $[\alpha/\text{Fe}]$  at the intermediate values of  $[\text{Fe}/\text{H}]$  for which the bimodality is most pronounced. The green case corresponds to the greatest values of  $[\text{Fe}/\text{H}]$ . The three samples comprise between approximately 400 and 900 stellar particles. The overlaid tracks of the same colour show the evolution, for each population, of the median  $[\alpha/\text{Fe}]$  and  $[\text{Fe}/\text{H}]$  abundances of the gas particles that remain unconsumed by star formation. To avoid poor sampling of the measurement, the tracks truncate when only 30 gas particles remain unconsumed, and the evolution of the consumed fraction is shown via the symbols overlaid on each track, which denote the epochs at which 25 percent (circle), 50 percent (square) and 75 percent (triangle) of the gas particles have been consumed (these conditions apply to all tracks presented in this figure). Star formation does not uniformly sample the natal gas, so the elemental abundances of stars formed at a given epoch are not represented by the corresponding position on the median tracks; the dashed black track therefore shows the evolution of the SFR-weighted mean coordinate in  $[\alpha/\text{Fe}]\text{-}[\text{Fe}/\text{H}]$  space. The tracks begin when at least 30 particles have a non-zero SFR. We stress that this track does not represent the enrichment history of any particular gas population, but rather the characteristic elemental abundances with which stars are being formed at the corresponding epoch.

It is immediately apparent that the enrichment histories of the natal gas of the high- and low- $[\alpha/\text{Fe}]$  populations are markedly different. They differ in  $[\alpha/\text{Fe}]$  already at

very low  $[\text{Fe}/\text{H}]$ , and the difference grows as the populations become more metal rich. The high- $[\text{Fe}/\text{H}]$  population exhibits a similar enrichment history to the low- $[\alpha/\text{Fe}]$  population, but is offset to lower  $[\alpha/\text{Fe}]$ ; it is accreted at late times (as we shall discuss shortly, much of it is delivered by a gas-rich satellite) and enriches to high- $[\text{Fe}/\text{H}]$  as it mixes with the interstellar gas of the evolved galaxy. The dashed black track shows that at early times, the  $z = 0$  disc stars of this galaxy initially form with elevated  $\alpha$ -elemental abundances and an increasing  $[\text{Fe}/\text{H}]$ , resulting in the formation of the high- $[\alpha/\text{Fe}]$  sequence. Once a little over 25 percent of all present day disc stars have formed, the formation of high- $[\alpha/\text{Fe}]$  stars begins to subside and the low- $[\alpha/\text{Fe}]$  sequence also begins to emerge. At this epoch the SFR-weighted mean track necessarily declines (and does so at roughly fixed  $[\text{Fe}/\text{H}]$ ), and subsequently converges with the low- $[\alpha/\text{Fe}]$  sequence.

The clear and persistent separation of the median abundances of the natal gas of the high- and low- $[\alpha/\text{Fe}]$  populations signals that they never mixed. In contrast to a central assumption of the two-infall model, at no stage of its evolution does the natal gas of the low- $[\alpha/\text{Fe}]$  sequence reach values of  $[\alpha/\text{Fe}]$  that are characteristic of the high- $[\alpha/\text{Fe}]$  population. Hence, rather than subsequently declining to roughly solar  $[\alpha/\text{Fe}]$  in response to enrichment by Type Ia SNe ejecta, it simply never reaches values of  $[\alpha/\text{Fe}]$  as elevated as those realised by the natal gas of the high- $[\alpha/\text{Fe}]$  population.

The contrasting enrichment histories of the two gas populations are made more apparent by inspection of the centre-left and bottom-left panels of Fig. 2.6. Respectively, these show the temporal evolution of  $[\alpha/\text{Fe}]$  and  $[\text{Fe}/\text{H}]$ , with the thick solid lines denoting median values and the shaded regions the interquartile range. As with the upper-left panel, since star formation samples a very unrepresentative subset of the gas comprising each population, we stress that the coloured tracks do not denote the typical abundances with which the stars of each population form at the corresponding epoch. To give a sense of how the median abundances of each population differ from the latter, we again show the galaxy's SFR-weighted mean abundance as a dashed black track. All three gas populations do initially become  $\alpha$ -enriched in response to early star formation; the natal gas of the high- $[\alpha/\text{Fe}]$  stars is rapidly enriched to

$[\alpha/\text{Fe}] \simeq 0.5$  and  $[\text{Fe}/\text{H}] \simeq -0.5$ , and is mostly consumed by  $t \simeq 4$  Gyr. After its initial enrichment with  $\alpha$ -elements, the low- $[\alpha/\text{Fe}]$  population's natal gas settles to a value of  $[\alpha/\text{Fe}] \simeq 0.35$  at  $t \simeq 5$  Gyr ( $z \simeq 1.5$ ), after which it is steadily enriched by Type Ia SNe as it is consumed. This gradually reduces its  $[\alpha/\text{Fe}]$ , and increases its  $[\text{Fe}/\text{H}]$ , in a broadly monotonic fashion. The evolution of  $[\text{Fe}/\text{H}]$  for this population is much more gradual than is the case for the natal gas of the high- $[\alpha/\text{Fe}]$  stars, the latter reaching  $[\text{Fe}/\text{H}] \gtrsim -0.5$  more than 3 Gyr sooner than the former. The correspondence of the high- $[\text{Fe}/\text{H}]$  population with the low- $[\alpha/\text{Fe}]$  population is also apparent from inspection of the time evolution of  $[\alpha/\text{Fe}]$  and  $[\text{Fe}/\text{H}]$ . The high- $[\text{Fe}/\text{H}]$  population represents the late-infalling subset of the overall low- $[\alpha/\text{Fe}]$  sequence, resulting in a lower abundance of  $\alpha$  elements and a higher abundance of Fe.

We can conclude from analysis of this galaxy that the elemental abundances of the natal gas of its high- and low- $[\alpha/\text{Fe}]$  populations evolved along distinct paths. Although the latter briefly exhibits elevated  $[\alpha/\text{Fe}]$  at early times, which subsequently declines in response to enrichment by Type Ia SNe, this gas never reaches  $[\alpha/\text{Fe}]$  comparable to that of the stars comprising the high- $[\alpha/\text{Fe}]$  sequence. The formation of the high- $[\alpha/\text{Fe}]$  sequence is therefore not imprinted in the abundances of the gas from which the low- $[\alpha/\text{Fe}]$  sequence subsequently forms, as one might expect if, as postulated by the two-infall model, the low- $[\alpha/\text{Fe}]$  sequence forms from a mixture of gas accreted from the intergalactic medium and interstellar gas remaining after an initial episode of star formation. This notwithstanding, the characteristic  $\alpha$ -element and Fe abundances with which stars form, quantified by the mean SFR-weighted coordinate in  $[\alpha/\text{Fe}]$ - $[\text{Fe}/\text{H}]$  space, does evolve in a fashion that is qualitatively similar to the expectations of the two-infall model: the typical  $[\alpha/\text{Fe}]$  declines rapidly as the formation of the high- $[\alpha/\text{Fe}]$  sequence draws to a close and the low- $[\alpha/\text{Fe}]$  sequence begins to dominate. However, as was also noted recently by ? following analysis of the Auriga simulations, the continuous increase of  $[\text{Fe}/\text{H}]$  of the natal gas of all populations is incompatible with a key expectation of the two-infall model, namely that the metallicity of the gas from which the Milky Way's disc stars are formed converges towards an equilibrium value.

The dissimilar evolutionary histories of the natal gas of the stars comprising high- and low- $[\alpha/\text{Fe}]$  sequences implies that these gas populations remained physically separated, and hence chemically independent, prior to their consumption by star formation. This suggests that they accreted onto the galaxy at different times. To explore this possibility, we crudely reconstruct the collapse history of the natal gas of the three populations defined in the upper-left panel of Fig. 2.6. This is achieved by computing the spherical galactocentric radii of the unconsumed gas particles as a function of cosmic time, relative to the coordinate of the most-bound particle of the galaxy’s main progenitor subhalo. The resulting trajectories are shown in the upper-right panel, with the tracks denoting the median radius and the shading denoting the interquartile range. The plot adopts proper (rather than comoving) coordinates, to highlight the expansion of gas with the Hubble flow at epochs prior to turnaround, and the horizontal dotted line at 30 pkpc provides a threshold for considering the gas to have accreted onto the galaxy; this definition is consistent with that used in Section 2.2.2. We again stress that, since star formation does not uniformly sample the gas comprising each population, the median tracks do not denote the typical radius at which stars form at each epoch; we do not include a SFR-weighted track here, as the value is always  $\ll 30$  pkpc.

The high- $[\alpha/\text{Fe}]$  population reaches its radius of maximum expansion (the “turnaround radius”) earlier ( $t \simeq 1$  Gyr) than the low- $[\alpha/\text{Fe}]$  population ( $t \simeq 2$  Gyr), and does so at a median galactocentric radius that is more than a factor of two smaller. A significant fraction of natal gas of the low- $[\alpha/\text{Fe}]$  population is delivered by a gas-rich satellite at  $t \simeq 10$  Gyr, which induces the oscillatory structure in its median radius. The natal gas of the high- and low- $[\alpha/\text{Fe}]$  populations is in general not co-spatial, precluding significant mixing of their kernel-smoothed element abundances: the median galactocentric radius of the high- $[\alpha/\text{Fe}]$  population drops below 30 pkpc at  $t = 3.4$  Gyr, at which time only 3 percent of the particles comprising the low- $[\alpha/\text{Fe}]$  population are located within 30 pkpc. The median galactocentric radius of the latter falls below 30 pkpc much later, at  $t \simeq 9$  Gyr, by which time all of the high- $[\alpha/\text{Fe}]$  population’s stars have already formed.

The influence of the accretion history on the enrichment of these populations is made

clear by the centre-right and bottom-right panels of Fig. 2.6. The former shows the evolution of the consumption timescale,  $t_g$ , of the gas, the latter shows the evolution of the gas-phase mass fraction of Fe synthesised by Type Ia SNe  $f_{\text{Fe,SNIa}}$ . Here,  $t_g$  is computed as per Equation 2.4, replacing  $P_\star$  by the gas particle’s pressure. For consistency with Fig. 2.4, we assume this to be the equation of state pressure corresponding to the density of the gas,  $P_{\text{eos}}(\rho)$ . Since we are specifically concerned in these two panels with the subset of the gas sampled by star formation, the coloured tracks here show the SFR-weighted mean of the quantity in question, and they begin when at least 30 particles have a non-zero SFR. The shaded regions show the 16<sup>th</sup> – 84<sup>th</sup> percentile scatter, as an estimate of the  $1\sigma$  scatter about the mean.

The early collapse of the natal gas of the high- $[\alpha/\text{Fe}]$  population drives it to high densities and pressures, fostering its rapid conversion to stellar particles with a characteristic consumption timescale that is typically  $t_g \lesssim 500$  Myr, and hence much shorter than the e-folding ( $\tau = 2$  Gyr, upper dashed line) and half-life ( $t_{1/2} = \tau \log(2) = 1.39$  Gyr, lower dotted line) timescales of the Type Ia SNe delay time function. In contrast, over 75 percent of the stars comprising the low- $[\alpha/\text{Fe}]$  sequence (and nearly all of the high- $[\text{Fe}/\text{H}]$  stars) form from gas with a consumption timescale of  $t_g \gtrsim 1.0$  Gyr. The influence of this dichotomy on the enrichment of star-forming gas by Type Ia SNe is then clear from inspection of the bottom-right panel of Fig 2.6. At early epochs, when the high- $[\alpha/\text{Fe}]$  stars form, the typical fraction is  $f_{\text{Fe,SNIa}} \simeq 0.35$ . At  $t \gtrsim 4$  Gyr there is a clear jump in the typical Fe mass fraction from Type Ia SNe, with the low- $[\alpha/\text{Fe}]$  and high- $[\text{Fe}/\text{H}]$  populations, which largely form after this transition, typically exhibiting  $f_{\text{Fe,SNIa}} \simeq 0.55$ .

Returning briefly to the upper-right panel of Fig. 2.6, it is striking that the gas from which the stars comprising the high- $[\alpha/\text{Fe}]$  sequence formed was significantly more compact prior to its consumption than was the gas that fuelled the formation of the low- $[\alpha/\text{Fe}]$  stars. This is perhaps to be expected; linear tidal torque theory (??) posits that the angular momentum of matter grows whilst it expands with the Hubble flow ( $L \propto a^{3/2}$ ), and remains constant after turnaround. Gas that reaches its radius of maximum expansion later is therefore expected to build more angular momentum, and

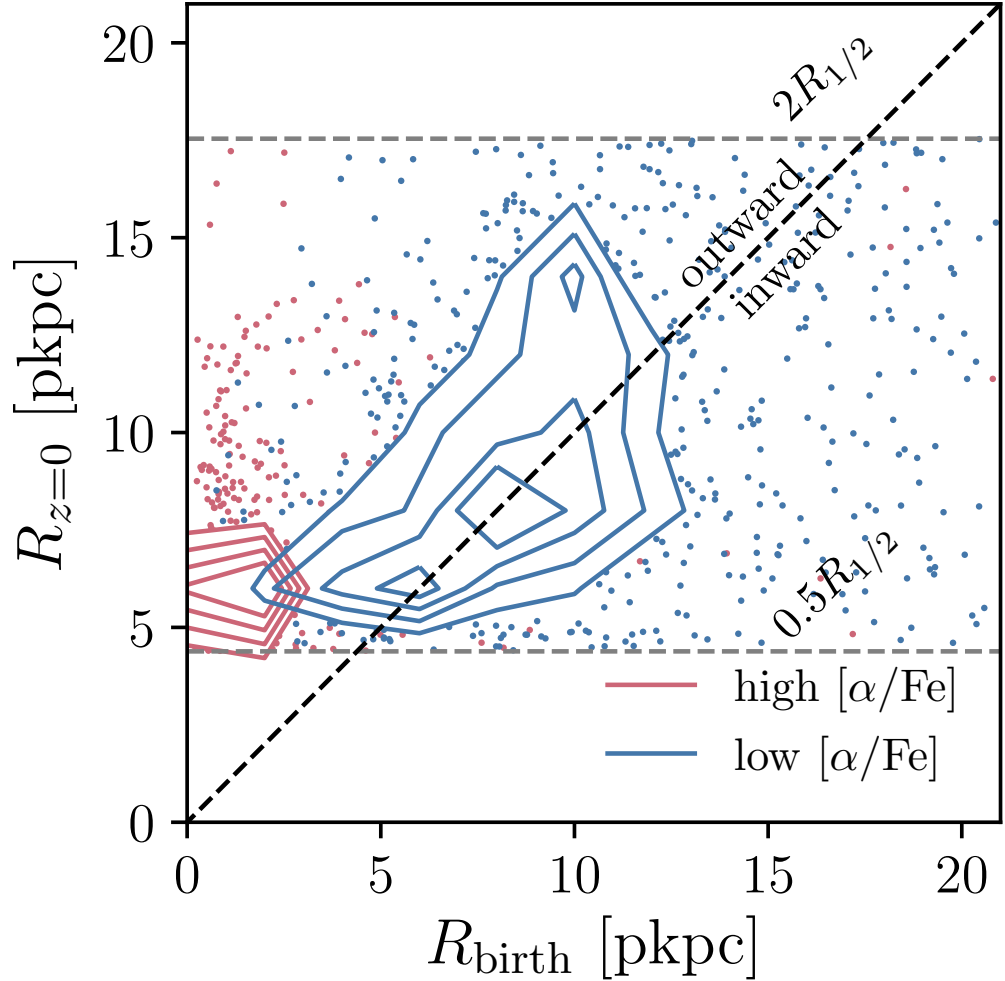


Figure 2.7: The cylindrical radii at the present day,  $R_{z=0}$ , of the stellar particles comprising the high- (red) and low- $[\alpha/\text{Fe}]$  (blue) populations of the example galaxy from Ref-L025N0376, as a function of their cylindrical radii at birth,  $R_{\text{birth}}$ . The distribution is shown with contours denoting the levels containing 50, 60, 70 and 80% of the points, with individual particles drawn beyond the outer (80%) contour. Grey dashed lines at  $R_{z=0} = 0.5R_{1/2}$  and  $R_{z=0} = 2R_{1/2}$  show the cylindrical radial boundaries used to define the disc stars, and the black dashed line denotes the locus  $R_{z=0} = R_{\text{birth}}$ . The low- $[\alpha/\text{Fe}]$  population has experienced mild outward radial migration, albeit with large scatter. The high- $[\alpha/\text{Fe}]$  population has necessarily experienced significant outward radial migration in order to be identified as part of the disc, since these stars formed almost exclusively within 5 pkpc of the galactic centre.

settle farther out in the galaxy disc. This raises the question of how the stars of both the high- and low- $[\alpha/\text{Fe}]$  populations came to be broadly co-spatial at the present day.

Fig. 2.7 plots the distribution of the present-day cylindrical galactocentric radius of the high- and low- $[\alpha/\text{Fe}]$  stars,  $R_{z=0}$ , of the example galaxy from Ref-L025N0376, as a function of their cylindrical galactocentric radius at birth,  $R_{\text{birth}}$ . Horizontal dashed lines denote  $0.5R_{1/2}$  and  $2R_{1/2}$ , the cylindrical radial boundaries we impose to select disc stars at  $z = 0$ , whilst the black dashed line denotes the locus  $R_{z=0} = R_{\text{birth}}$ . The low- $[\alpha/\text{Fe}]$  population generally tracks this locus, albeit with a large scatter such that significant positive and negative migration is common. Overall there is a mild preference for net positive migration. In contrast, the high- $[\alpha/\text{Fe}]$  population of this galaxy forms almost entirely at  $R_{\text{birth}} < 3 \text{ pkpc}$ , which is likely a necessary condition in order to realise the short consumption timescales that preclude the enrichment of their natal gas with Type Ia SNe ejecta. Positive outward migration of these stellar particles is therefore necessary in order for them to be categorised as part of the (geometric) disc.

Isolating the physical cause of this migration is beyond the scope of this study. We note that the limited resolution of our simulations, and their implicit treatment of the cold interstellar gas phase, preclude an examination of whether such migration might be dominated by the ‘blurring’ or ‘churning’ processes discussed by ?. That notwithstanding, as recently argued by ? following analysis of the high-resolution APOSTLE simulations (?) that also use the EAGLE galaxy formation model, dynamical effects similar to those expected to follow from detailed internal processes can also arise in response to the evolution of the ISM from a ‘thick’ state at early times to a more settled state at low redshift, as the accretion of gas onto (and ejection of gas from) galaxy discs declines (see also ???).

### 2.4.1 Applicability to galaxies in the Ref-L100N1504 simulation

Visual inspection of the  $[\alpha/\text{Fe}]\text{-}[\text{Fe}/\text{H}]$  planes of the 133 EAGLE galaxies in our sample reveals six that exhibit two clearly-separated sequences in  $[\alpha/\text{Fe}]\text{-}[\text{Fe}/\text{H}]$  space. The  $[\alpha/\text{Fe}]\text{-}[\text{Fe}/\text{H}]$  distributions of these galaxies are shown in the left-hand column

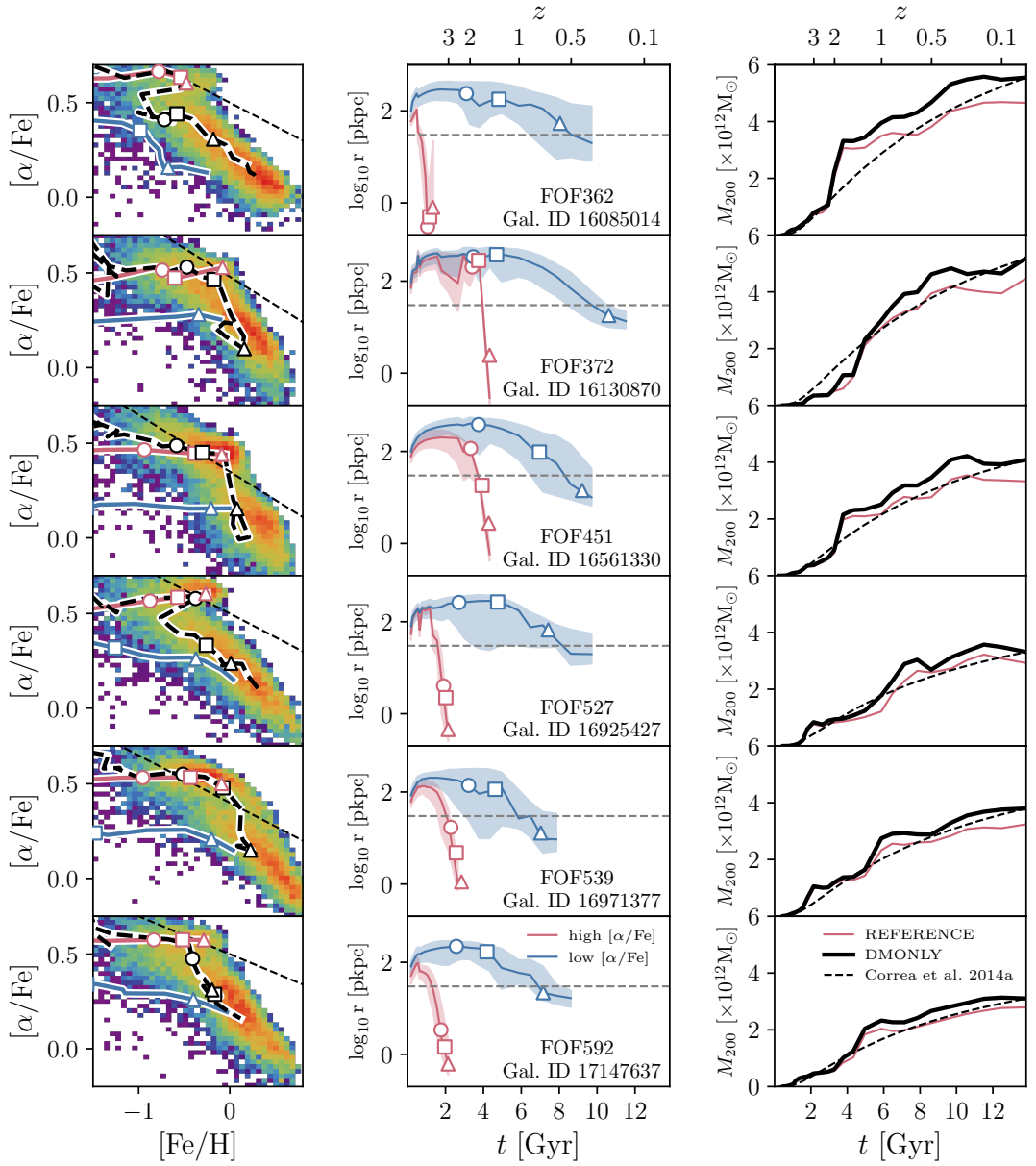


Figure 2.8: The evolution of the six galaxies from Ref-L100N1504 that exhibit bimodality in  $[\alpha/\text{Fe}]$  at fixed  $[\text{Fe}/\text{H}]$ . Similarly to Fig. 2.6, the left-hand column shows the  $[\alpha/\text{Fe}]$ - $[\text{Fe}/\text{H}]$  distribution of the disc stars of these galaxies as a 2-dimensional histogram. Here the disc stars are split into high- and low- $[\alpha/\text{Fe}]$  populations with a simple visually-defined cut, shown by the thin dashed line. The centre column shows the expansion, collapse and accretion onto the galaxy of the natal gas of these two populations. The right-hand column, discussed in Section 2.5, shows the total mass accretion history of the galaxies, i.e.  $M_{200}(t)$ . The red curve shows this quantity within the Ref-L100N1504 simulation, whilst the black curve denote the evolution of the same halo identified in its dark matter-only counterpart, DM ONLY-L100N1504. Here, the dashed black curve denotes the typical accretion history of haloes with the same present-day mass as the DM ONLY realisation of the halo, as parametrised by ?.

of Fig. 2.8. In a similar fashion to the case discussed in Section 2.4, we split the population of disc stars of these galaxies into high- and low- $[\alpha/\text{Fe}]$  sequences, to examine their evolution separately. These examples exhibit a diversity of  $[\alpha/\text{Fe}]\text{-}[\text{Fe}/\text{H}]$  morphologies, so we adopt simple, visually-defined cuts that assign all disc stars to one of the two sequences, as indicated by the dashed lines on each panel. The cuts are defined such that they best separate the sequences where they are well separated. The overlaid tracks and symbols are defined as per the top-left panel of Fig. 2.6. Similarly, the centre column shows the collapse histories of the gas from which the two populations formed, as per the upper-right panel of Fig. 2.6. We discuss the right-hand column later in Section 2.5.

These panels reveal illuminating features, similarities and differences with respect to the example in Fig. 2.6. As there, the natal gas populations of the stars comprising the high- and low- $[\alpha/\text{Fe}]$  sequences exhibit distinct enrichment histories, implying a general lack of mixing of their element abundances prior to their consumption by star formation. In all cases, the natal gas of the high- $[\alpha/\text{Fe}]$  sequence reaches a relatively short radius of maximum expansion, "turning around" and accreting onto the galaxy significantly earlier than that of the low- $[\alpha/\text{Fe}]$  sequence. This early collapse enables rapid formation of the high- $[\alpha/\text{Fe}]$  sequence, with the short consumption timescales necessary to inhibit enrichment by the ejecta of Type Ia SNe. As might be expected, the most  $\alpha$ -rich sequences are formed by the galaxies for which the natal gas collapses at the earliest epochs (FOF362, FOF527 and FOF592), whilst the example for which the natal gas of the two sequences is the most cospatial prior to its accretion onto the galaxy (FOF372) exhibits the least well-separated sequences in  $[\alpha/\text{Fe}]\text{-}[\text{Fe}/\text{H}]$  space. The galaxies also exhibit diversity in the maximum  $[\text{Fe}/\text{H}]$  abundance to which the high- $[\alpha/\text{Fe}]$  sequence extends; as expected, we find this is correlated to the mass of stars formed from the gas delivered in the initial episode.

The track of the mean SFR-weighted element abundances exhibits significant diversity, reflecting the non-trivial enrichment evolution of the *star-forming* ISM. The tracks for galaxies FOF 362 and FOF527 illustrate that, as the formation of the high- $[\alpha/\text{Fe}]$  sequence concludes and the formation of low- $[\alpha/\text{Fe}]$  stars begins to dominate, the decline

of the characteristic  $[\alpha/\text{Fe}]$  is accompanied by a temporary decrease in the characteristic Fe abundance with which new stars are formed (by  $\Delta[\text{Fe}/\text{H}] \lesssim -0.5$ ). This indicates that, as posited by the two-infall model, in these two cases the accretion of unenriched gas temporarily lowers the metallicity of the star-forming ISM. Conversely, in the other four bimodal galaxies, the decrease in  $[\alpha/\text{Fe}]$  associated with the transition from the high- to low- $[\alpha/\text{Fe}]$  sequence is accompanied by mild increase in  $[\text{Fe}/\text{H}]$ .

## 2.5 Connecting disc star element abundances to halo mass accretion histories

The analyses presented in Section 2.4 show that distinct sequences in  $[\alpha/\text{Fe}]\text{-}[\text{Fe}/\text{H}]$  space arise in galaxies where disc stars are formed from gas that was accreted onto the galaxy in somewhat separated episodes. Since the accretion of gas is primarily driven by the gravitational evolution of a galaxy’s dark matter halo (?????), this finding highlights that the distribution of disc stars in the  $[\alpha/\text{Fe}]\text{-}[\text{Fe}/\text{H}]$  plane is influenced not only by astrophysical processes, but perhaps more fundamentally by the hierarchical formation and assembly of the galaxy. We therefore briefly examine in this section the connection between bimodality in  $[\alpha/\text{Fe}]$  at fixed  $[\text{Fe}/\text{H}]$ , and the accretion history of a galaxy’s dark matter halo.

The right-hand column of Fig. 2.8 shows the total mass accretion history of the six bimodal galaxies discussed in Section 2.4.1, characterised by the evolution of the halo virial mass,  $M_{200}(t)$ . In each case, the red curve shows growth of the virial mass of the halo within the Ref-L100N1504 simulation. The thick solid curve shows the evolution of  $M_{200}^{\text{DMO}}(t)$ , the virial mass of the same halo, identified using the techniques described by ?, in a simulation of the L100N1504 volume considering only collisionless gravitational dynamics (DMONLY-L100N1504). This track is instructive as it eliminates the influence of astrophysical processes associated with baryons, such as adiabatic contraction, which acts to increase the central density of the halo, and the reduction of the halo’s mass and accretion rate due to the ejection of baryons by feedback pro-

cesses. The dashed curve shows the typical accretion history of a halo with the same present-day mass as the halo in the DMONLY-L100N1504 simulation, as derived by ? through application of the extended Press-Schechter (EPS) formalism to the growth rate of initial density perturbations.

The importance of accounting for the influence of baryon physics, in particular ejective feedback, is made clear by comparison of the Reference and DMONLY curves. In each case, these curves diverge significantly at intermediate redshifts ( $1 \lesssim z \lesssim 3$ ). As shown by ?, their Fig. 1, the median of the ratio  $M_{200}/M_{200}^{\text{DMO}}$  at  $z = 0$  is  $\simeq 0.85$  for haloes of  $M_{200}^{\text{DMO}} \sim 10^{12} - 10^{13} M_{\odot}$ . Comparison of the DMONLY curves with the ? fitting function reveals that a common feature of the mass accretion histories of the 6 bimodal galaxies is rapid growth at early times ( $4 \lesssim t \lesssim 6$  Gyr or  $1 \lesssim z \lesssim 2$ ), such that early in their assembly, they grow faster than is typical for haloes of the same present-day mass. Their accretion rate subsequently declines relative to the average rate for haloes of the same  $z=0$  mass, such that at late times  $M_{200}^{\text{DMO}}(t)$  grows at a significantly *lower* rate than is typical. Naïvely, an elevated mass accretion rate at early cosmic epochs is qualitatively consistent with the early collapse of the gas that fuels the formation of the high-[ $\alpha/\text{Fe}$ ] sequence. This also motivates the question of whether the haloes that host disc-dominated galaxies with distinct sequences in [ $\alpha/\text{Fe}$ ]-[Fe/H] space differ significantly and systematically from those hosting disc-dominated galaxies with unimodal [ $\alpha/\text{Fe}$ ]-[Fe/H] distributions.

We therefore identify the DMONLY counterpart haloes of all 133 Milky Way-like galaxies in Ref-L100N1504. We plot in Fig. 2.9 the median and interquartile range of  $M_{200}^{\text{DMO}}(t)$  derived from these samples (blue curves denote the entire sample, red curves denote the six bimodal galaxies). As per the right-hand column of Fig. 2.8, the overlaid dashed curves that intersect the median curves at  $z = 0$  denote the typical accretion histories, as parametrised by Correa et al. (2017a), of haloes with the same present-day mass. Comparison of the two median tracks indicates that the phase of rapid growth exhibited by bimodal galaxies between  $t \simeq 4$  and  $t \simeq 8$  Gyr (corresponding to  $z \simeq 1.6$  and  $z \simeq 0.5$ ) is not common amongst the broader population of Milky Way-like galaxies. In general, the latter exhibit accretion histories that are

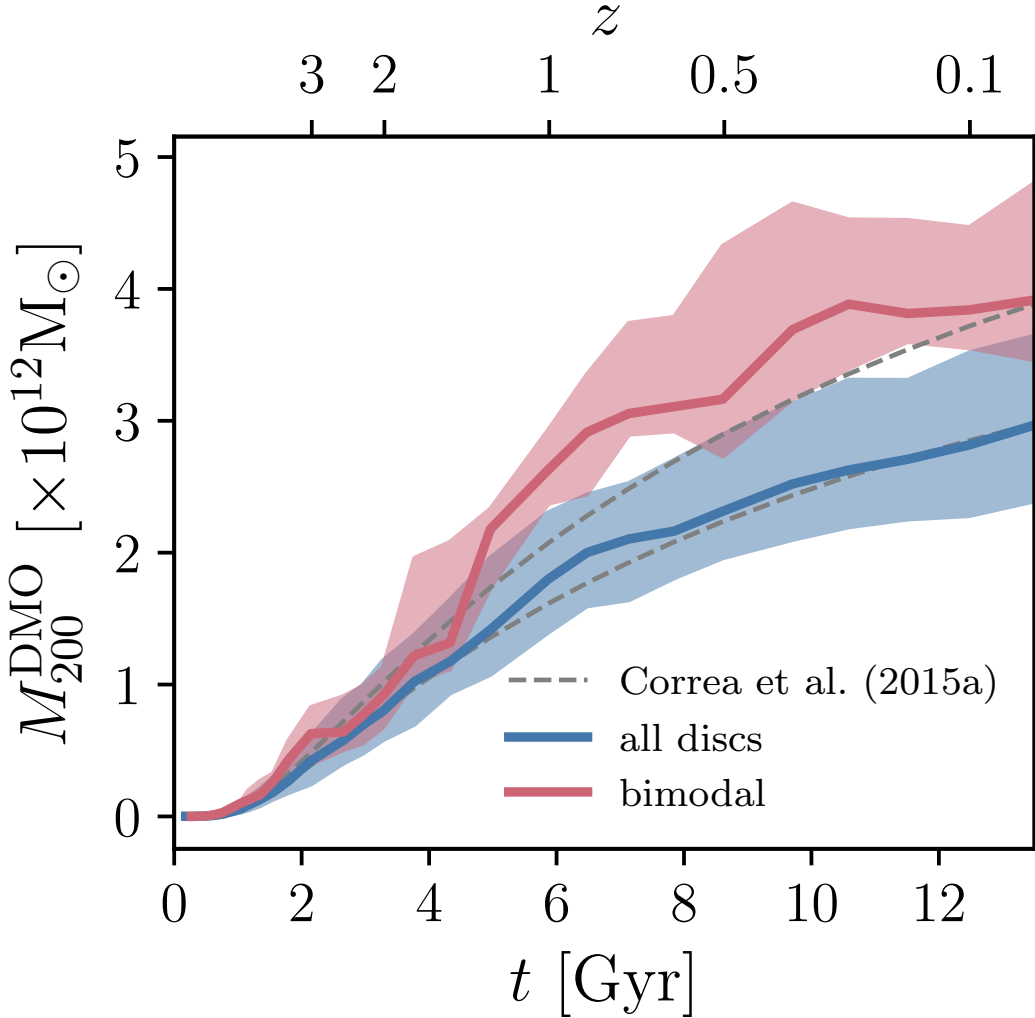


Figure 2.9: The mass accretion history,  $M_{200}(t)$ , of haloes identified in the DMONLY-L100N1504 simulation. The thick curves corresponds to the median, whilst the shaded regions denote the interquartile range. The blue curve corresponds to the partner haloes of all 133 galaxies in our Milky Way-like sample, whilst the red curve corresponds to the partner haloes of the 6 galaxies exhibiting bimodality in  $[\alpha/\text{Fe}]$  at fixed  $[\text{Fe}/\text{H}]$ . Dashed curves meeting the two median curves at  $z = 0$  show the typical accretion history, as parametrised by (?), of haloes with these  $z = 0$  masses. Haloes which host galaxies exhibiting  $[\alpha/\text{Fe}]$  bimodality have systematically different dark matter accretion histories

much more representative of the entire population of haloes with similar present-day mass. We therefore conclude that the accretion histories of bimodal galaxies are indeed atypical. We note that the present day halo masses of the bimodal galaxies are not representative of the overall distribution; the median  $M_{200}^{\text{DMO}}(z = 0)$  of the bimodal galaxies is equal to the 80<sup>th</sup> percentile of that of the overall sample of Milky Way-like galaxies. However, we have verified that median accretion history of the latter remains largely unchanged if one examines instead a sub-sample of these haloes whose present day masses span the same range as those of the bimodal galaxies.

An early and rapid phase of mass accretion onto a galaxy’s halo therefore appears to be a necessary (but perhaps not sufficient) condition for the emergence of distinct sequences in the  $[\alpha/\text{Fe}]\text{-}[\text{Fe}/\text{H}]$  distribution of disc stars. Further, more detailed examination of the connection between halo accretion histories and the elemental abundances of disc stars is beyond the scope of this study, however we can already note two implications of these findings. Firstly, since halo accretion histories are purely a consequence of the initial phase-space configuration of the matter destined to comprise a galaxy’s dark matter halo, whether or not a galaxy will develop bimodal sequences in the  $[\alpha/\text{Fe}]\text{-}[\text{Fe}/\text{H}]$  plane is effectively determined at early cosmic epochs. Secondly, the key role played by a galaxy’s accretion history implies that predictive modelling of the emergence of the  $[\alpha/\text{Fe}]\text{-}[\text{Fe}/\text{H}]$  distribution of disc stars requires that the formation and assembly of the galaxy is considered in its cosmological context. Specifically, this entails accounting for growth, merging history and chemical evolution of a galaxy’s progenitors. These processes are incorporated self-consistently in cosmological hydrodynamical simulations, but are challenging to incorporate realistically into analytic models.

## 2.6 Summary and discussion

We have examined the enrichment history of disc stars in present-day galaxies in the EAGLE simulations of galaxy formation. In particular, we have focussed on the formation and assembly of galaxies whose disc stars exhibit distinct sequences in the

$[\alpha/\text{Fe}]$ - $[\text{Fe}/\text{H}]$  plane. Our findings can be summarised as follows:

- The distribution in  $[\alpha/\text{Fe}]$ - $[\text{Fe}/\text{H}]$  space of the disc stars of simulated Milky Way-like galaxies is characterised by a roughly constant  $\alpha$ -element abundance of  $[\alpha/\text{Fe}] \simeq 0.5$  for  $[\text{Fe}/\text{H}] < -0.5$ , whilst it declines roughly linearly at higher Fe abundance, to  $[\alpha/\text{Fe}] \simeq -0.1$  at  $[\text{Fe}/\text{H}] = 1.0$  (Fig. 2.1).
- At any fixed  $[\text{Fe}/\text{H}]$ ,  $[\alpha/\text{Fe}]$  anti-correlates linearly with  $f_{\text{Fe,SNIa}}$ , the mass fraction of a star's Fe that was synthesised by Type Ia SNe. This demonstrates that the key driver of elevated  $\alpha$ -element abundances is, unsurprisingly, the smaller fraction of Fe synthesised by this channel. There is also a weaker trend such that at fixed  $[\alpha/\text{Fe}]$ ,  $f_{\text{Fe,SNIa}}$  declines with increasing  $[\text{Fe}/\text{H}]$ , since the main pathway for increasing  $[\text{Fe}/\text{H}]$  without reducing  $[\alpha/\text{Fe}]$  is to source a greater fraction of Fe from the same source as the  $\alpha$  elements, i.e. Type II SNe (Fig. 2.2).
- Broadly, the oldest stars exhibit low  $[\text{Fe}/\text{H}]$  and high  $[\alpha/\text{Fe}]$ , whilst the youngest stars exhibit the opposite. But the correlation of age with both abundance diagnostics saturates such that large areas of the  $[\alpha/\text{Fe}]$ - $[\text{Fe}/\text{H}]$  plane exhibit similar characteristic ages, precluding the use of either as an accurate chronometer and demonstrating that age is not the sole driver of element abundances (Fig. 2.3).
- At fixed  $[\text{Fe}/\text{H}]$ , the most  $\alpha$ -rich stars formed from gas with the shortest consumption timescales, highlighting that the key to yielding high values of  $[\alpha/\text{Fe}]$  is the consumption of star-forming gas before it can be substantially enriched with Fe from Type Ia SNe (Fig. 2.4).
- The distributions of the disc stars of rotationally-supported galaxies with similar mass to the Milky Way in the  $[\alpha/\text{Fe}]$ - $[\text{Fe}/\text{H}]$  plane are diverse. The majority are unlike that of the Milky Way, insofar as they do not exhibit two distinct sequences. Only  $\simeq 5$  percent of Milky Way-like galaxies in EAGLE exhibit bimodality in  $[\alpha/\text{Fe}]$  at fixed  $[\text{Fe}/\text{H}]$ . A few galaxies exhibit only the high- $[\alpha/\text{Fe}]$  sequence. The distribution is closely connected to the star formation history of the disc stars, with the high- $[\alpha/\text{Fe}]$  sequence resulting from intense star forma-

tion at early times ( $z \gtrsim 2$ ), and the low-[ $\alpha$ /Fe] sequence from extended star formation at later times (Fig. 2.5).

- In galaxies exhibiting distinct high- and low-[ $\alpha$ /Fe] sequences, the gas from which the stars comprising each sequence formed is accreted onto the galaxy in distinct episodes. This temporal separation inhibits mixing of the two gas populations, enabling divergent evolution of their element abundances from an early epoch. The low-[ $\alpha$ /Fe] sequence does not form (primarily) from interstellar gas left unconsumed by the formation of the high-[ $\alpha$ /Fe] sequence, therefore the oldest stars of the former can exhibit lower [Fe/H] than the youngest stars of the latter. The median Fe abundance of both sequences increases monotonically and continuously and, in contrast to the common assumption of analytic models, does not reach a constant equilibrium value (Fig. 2.6).
- The early collapse of the natal gas of the high-[ $\alpha$ /Fe] stars fosters star formation with short consumption times, precluding strong enrichment by Type Ia SNe (Fig. 2.6).
- The formation of high-[ $\alpha$ /Fe] stars from gas with short consumption timescales requires that they are born in a compact configuration; they are found in the disc at the present day having experienced a net outward radial migration over  $\simeq 8 - 10$  Gyr (Fig. 2.7).
- We identify six galaxies from our sample of 133 ( $\simeq 5$  percent), whose disc stars exhibit distinct sequences in [ $\alpha$ /Fe]-[Fe/H] space. In each case, the formation of the high-[ $\alpha$ /Fe] sequence is associated with the early infall of gas onto the galaxy, which is rapidly consumed by star formation. In galaxies for which the two accretion episodes are more clearly separated, the two sequences are also more distinct (Fig. 2.8).
- The dark matter haloes that host the six bimodal galaxies exhibit (total) mass accretion histories characterised by a rapid phase of growth at intermediate epochs ( $1 \lesssim z \lesssim 3$ ), followed by a tailing off to a significantly lower rate of growth.

Such accretion histories are atypical, as highlighted by comparison with the average accretion history of dark matter haloes with the same present-day virial mass (Fig. 2.8). Milky Way-like galaxies that exhibit only the low-[ $\alpha$ /Fe] sequence have dark matter halo accretion histories that are much more typical (Fig. 2.9).

The results presented here demonstrate that realistic cosmological hydrodynamical simulations do form galaxies whose present-day disc stars exhibit two distinct sequences in the [ $\alpha$ /Fe]-[Fe/H] plane, as revealed by spectroscopic surveys of the Galaxy. As also shown by ?, such sequences form in response to distinct episodes of gas accretion onto galaxies. We have shown that distinct accretion episodes lead to the formation of stars with differing characteristic gas consumption timescales: whilst the low-[ $\alpha$ /Fe] sequence forms from gas whose consumption timescale is similar to the e-folding timescale of the Type Ia SNe delay time distribution, the natal gas of the high-[ $\alpha$ /Fe] sequence is consumed on a much shorter timescale, suppressing enrichment by Type Ia SNe.

Our results corroborate the conclusion of ? that such a dichotomy is not ubiquitous<sup>3</sup> (c.f also ??). The large volume of the EAGLE Ref-L100N1504 simulation yields a sample of 133 ‘Milky Way-like’ galaxies (defined on the basis of their stellar mass and kinematics), enabling us to place, for the first time, galaxies with distinct [ $\alpha$ /Fe]-[Fe/H] sequences into the broader context of the galaxy population. The relative scarcity within EAGLE of galaxies with [ $\alpha$ /Fe]-[Fe/H] distributions similar to that observed in the Galaxy indicates that in this respect the Milky Way is likely unrepresentative of the broader population of  $\sim L^*$  late-type galaxies. We have demonstrated that such abundance patterns are likely to prove uncommon because distinct gas accretion episodes require an atypical mass accretion history, characterised by a phase of rapid growth at relatively early epochs. That the Galaxy’s element abundances and dark matter halo accretion history may be unrepresentative of the broader population

---

<sup>3</sup>The initial conditions of the Auriga simulations are drawn from the EAGLE Ref-L100N1504 volume; The EAGLE galaxies that form in the same haloes resimulated for the Auriga Project do not satisfy our selection criteria (Section 2.2.2), but we have examined these galaxies and found their [ $\alpha$ /Fe]-[Fe/H] planes to be qualitatively similar to those presented by ?.

of similarly massive disc galaxies suggests that caution should be exercised when generalising the findings of Galactic surveys, particularly for ‘near-field cosmology’ applications.

The conclusion of ?, that the enrichment history of galaxies in cosmological simulations contrasts with the expectations of leading analytic Galactic chemical evolution models, is also corroborated by our findings. The EAGLE simulations indicate that the metallicity of the natal gas of disc stars tends to increase continuously over time, and does not tend to an equilibrium value established by the balance of enrichment and gas infall. Our conclusion that two distinct accretion episodes are necessary to foster a bimodality in  $[\alpha/\text{Fe}]$  is an aspect in common with the ?? two-infall model (see also ?, who arrived at similar conclusions by fitting empirical star formation histories to measurements of the SNIa delay time distribution), but in other respects the simulations differ markedly from that model. The major difference is that the assumption of instantaneous and complete mixing of star-forming gas in the two infall model precludes the contemporaneous formation of stars with high- and low- $[\alpha/\text{Fe}]$ , and hence unavoidably imprints the natal gas of the low- $[\alpha/\text{Fe}]$  sequence with a chemical record of the formation of the high- $[\alpha/\text{Fe}]$  sequence. By contrast, although our simulations indicate that high- $[\alpha/\text{Fe}]$  stars do in general form prior to their low- $[\alpha/\text{Fe}]$  counterparts, the age distributions of the two populations can and do overlap. This is possible because the populations of gas from which they form remain largely unmixed prior to their consumption, precluding significant mixing of their element abundances. This aspect of our findings is similar to the model of ??, in which the inner (high- $[\alpha/\text{Fe}]$ ) and outer (low- $[\alpha/\text{Fe}]$ ) components of the Galaxy disc form from gas that remains physically and chemically separated prior to its consumption.

The chief systematic uncertainty to which our findings are subject is that of metal mixing, on both resolved and unresolved spatial scales. As discussed in Section 2.2.1, the EAGLE simulations do not incorporate an explicit subgrid diffusion scheme for element abundances, as the appropriate effective diffusion coefficients are not known *a priori*. As shown by ?, see their Fig. 9, inclusion of such a scheme most notably influences the metal-poor ( $Z_{\text{gas}} \lesssim 0.1Z_{\odot}$ ) regime of the metallicity distribution by assigning

a small, non-zero metal mass to a greater fraction of (mostly low density, intergalactic) gas. A rudimentary means of assessing the influence of small-scale mixing can be achieved by comparing, for example, the fiducial  $[\alpha/\text{Fe}]\text{-}[\text{Fe}/\text{H}]$  distribution (constructed using kernel-smoothed abundances) with that constructed using unsmoothed abundances (see e.g. Appendix B of ?). We have performed such a comparison and find that the induced changes to the  $[\alpha/\text{Fe}]\text{-}[\text{Fe}/\text{H}]$  plane are small and do not alter our conclusions.

There is also the possibility that EAGLE underestimates the macroscopic mixing of gas on resolved scales. As shown by ?, relatively little interstellar gas ejected from EAGLE galaxies is later reincorporated into the ISM to form stars. Other galaxy formation simulations have reported more prevalent reincorporation of ejected gas (see, e.g. ?), and this process remains poorly-constrained by observations. Greater recycling of gas within the circumgalactic medium (CGM) can in principle promote the mixing of gas that fuels the formation of disc stars, inhibiting the formation of very distinct sequences in  $[\alpha/\text{Fe}]\text{-}[\text{Fe}/\text{H}]$  space. However, since in the majority of cases examined here the natal gas of the high- $[\alpha/\text{Fe}]$  sequence is consumed prior to the gas of the low- $[\alpha/\text{Fe}]$  sequence reaching the turnaround radius, significant mixing is likely precluded, irrespective of the prevalence of halo recycling. Nonetheless, should macroscopic mixing be found to be underestimated in the EAGLE simulations, the likely conclusion is that galaxies with element abundances similar to the Milky Way are even more rare than inferred here.

The recent advent of large cosmological simulations that reproduce a broad array of observed galaxy properties presents an exciting opportunity to advance studies of the Galaxy's chemical history using forward modelling, in contrast to the largely inverse methods that attempt to reverse engineer its observed elemental abundances. In seeking to further our understanding of the formation and assembly of the Milky Way, and galactic archaeology more generally, we expect on-going improvements to the detail and realism of cosmological simulations to prove an important ally to the development of next generation of spectroscopic surveys of the Galaxy.

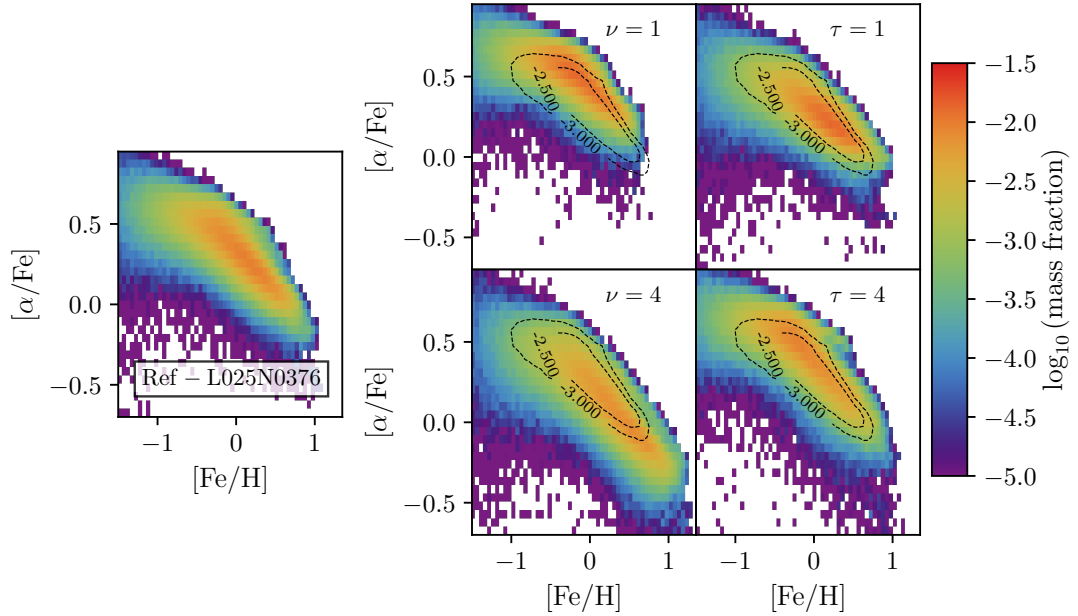


Figure 2.10: The  $[\alpha/\text{Fe}]$ - $[\text{Fe}/\text{H}]$  distribution of Milky Way like galaxies in simulations of the L025N0376 volume. The left panel shows the distribution realised by the Ref-L025N0376 simulation, whilst the four panels on the right show that from simulations in which a parameter governing the number of Type SNIa per unit stellar mass formed,  $\nu$ , or the characteristic e-folding timescale of the Type SNIa delay function,  $\tau$ , has been varied. On these panels, the overlaid black contours are from the Ref-L025N0376 distribution, highlighting the significant changes to the  $[\alpha/\text{Fe}]$ - $[\text{Fe}/\text{H}]$  distribution induced by these parameter changes.

## 2.7 Subgrid physics variations

We briefly examine in this appendix the degree to which variation of the subgrid parameters governing the rate of Type Ia SNe influences the  $[\alpha/\text{Fe}]$ - $[\text{Fe}/\text{H}]$  distribution of disc stars of Milky Way-like galaxies. We analyse four simulations that adopt the same initial conditions as the Ref-L025N0376 simulation, two of which vary the total number of Type Ia SNe per unit of initial stellar mass formed, adopting  $\nu = 1 \times 10^{-3} M_{\odot}^{-1}$  and  $\nu = 4 \times 10^{-3} M_{\odot}^{-1}$  (relative to the Reference model, which adopts  $\nu = 2 \times 10^{-3} M_{\odot}^{-1}$ ), and two of which vary the characteristic e-folding timescale of the Type Ia SNe delay time distribution, adopting  $\tau = 1 \text{ Gyr}$  and  $\tau = 4 \text{ Gyr}$  (where the Reference model assumes  $\tau = 2 \text{ Gyr}$ ).

We examine the 56 galaxies in the Ref-L025N0376 simulation with  $\kappa_{\text{co}} > 0.4$  and stellar mass in the interval  $4 < M_* < 8 \times 10^{10} M_{\odot}$ . We identify the same haloes in

the 4 variation runs using the same particle matching technique (?) used to pair haloes with their counterpart in the DMONLY simulation.

The right four panels of Fig. 2.10 show the  $[\alpha/\text{Fe}]\text{-}[\text{Fe}/\text{H}]$  distribution of these galaxies in the varied simulations as 2-dimensional histograms, with the overlaid contours showing the equivalent distribution from the Reference simulation, shown in its entirety in the left panel. Varying the number of Type Ia SNe per unit stellar mass formed has a significant impact on the distribution, as changing the number of Type Ia SNe also changes the total mass of Fe synthesised per unit stellar mass formed. Decreasing (increasing) the number of Type Ia SNe therefore shifts the distribution upward (downward) to a higher (lower)  $[\alpha/\text{Fe}]$ , and truncates the distribution at a lower (higher)  $[\text{Fe}/\text{H}]$ . The characteristic delay timescale of Type Ia SNe governs the likelihood of gas becoming enriched with the Fe synthesised by Type Ia SNe whose progenitors formed recently. A shorter (longer) delay timescale results in a greater (lesser) fraction of stars forming from Fe-rich gas, inhibiting (aiding) the formation of a high- $[\alpha/\text{Fe}]$  sequence.

These results indicate that the parameters governing the subgrid implementation of enrichment by Type Ia SNe, which are in general rather poorly constrained, have a tangible impact on the resulting  $[\alpha/\text{Fe}]\text{-}[\text{Fe}/\text{H}]$  distribution of disc stars. This highlights the importance of quantifying these sources of systematic uncertainty, and of ensuring that models used to examine the evolution of galaxy elemental abundances are broadly compatible with orthogonal constraints. As discussed by ?, the values of  $\nu$  and  $\tau$  adopted by EAGLE were calibrated to ensure that the simulations broadly reproduce the observed evolution of the cosmic Type Ia SNe rate density.

# Chapter 3

## High Eccentricity Population

### 3.1 Introduction

It is now well established that accretion of lower mass systems is a fundamental component of the evolution and mass build up of galaxies (?). Due to its very long dynamical timescale, the stellar halo of the Milky Way keeps a record of the Galaxy's past accretion activity. That record can be accessed through the collection of precision 6D phase space and multi-element abundance information for very large samples of halo stars, which together enable fundamental tests of galaxy formation models. While this field has a long history (e.g., ??), we highlight only a few of the main contributions from the past decade, for brevity. ? and ? were the first to identify the presence of an older, high  $\alpha$  and a younger, low  $\alpha$  halo population at metallicity lower than that of the Galactic disc in the solar neighbourhood, whose kinematics suggested an *in situ* and an accreted nature, respectively. More recently, ? proposed abundance ratio diagnostics to distinguish accreted from *in situ* halo stars, arguing that the accreted population dominates the nearby halo. Using APOGEE data, ? and ? studied the chemical compositions and kinematics of the metal-rich nearby halo, suggesting that much of the low halo population is associated with the debris of accreted satellites, likely with a similar star formation history to the Large Magellanic Cloud (LMC).

Studies of the Galactic halo are being revolutionised by the advent of large astrometric, photometric, and spectroscopic surveys of the stellar populations of the Galaxy. The *Gaia* astrometric satellite has opened new avenues for exploration of substructure in phase space, with the potential for new discoveries further amplified by the addition of chemical information from spectroscopic surveys. Indeed, combining *Gaia* parallaxes and proper motions (??) with spectroscopic data from SDSS (?) and APOGEE (?), two groups have identified what seems to be the accretion of a relatively massive stellar system that dominates the stellar populations of the nearby halo. Analysing a sample of SDSS-*Gaia* DR1 main sequence stars, ? showed that the velocity ellipsoid of halo stars becomes strongly anisotropic for stars with  $[Fe/H] > -1.7$ . Comparing their data to a suite of N-body only cosmological numerical simulations, they concluded that such orbital configurations are likely to result from the accretion of a massive satellite at about the time of the formation of the Galactic disc, roughly between  $z = 1$  and 3.

Based on *Gaia* DR2 data, ? determined the configuration of MW globular clusters (GCs) in action space. They find that 12 GCs in the halo are consistent with an origin in a single massive accretion event, consistent with the conclusions reached by ?. ? find that these clusters have highly eccentric orbits, at  $e \gtrsim 0.85$ , and suggest that the fact that all the clusters occupy a similar region in action space supports the idea that this highly anisotropic stellar population in the halo is mainly formed from the debris of a single accretion event.

In a follow up study, ? estimated the orbital parameters for a sample of nearby main-sequence and distant horizontal-branch stars by combining *Gaia* DR2 data (?) with spectroscopic outputs from SDSS-DR9 (?). They found that the apocentre radii of a significant population of stars in the halo appear to ‘pile up’ at an  $r_{ap} \sim 20$  kpc. The authors link this population with that found by ?, which they nickname the “sausage”, due to the shape of the distribution in velocity space. This result has special significance in light of the analysis of numerical simulations by ?, who proposed that the existence of a “break radius” in the Milky Way halo, beyond which the stellar density drops precipitously, is associated with the “pile up” of stellar apocenters at a comparable Galactocentric distance. ? argue that the observed existence of a break radius in

the Milky Way halo and the absence of such a break in the Andromeda galaxy (M31) suggests that the latter had a much more prolonged accretion history than the former.

An independent analysis of *Gaia* DR2 data conducted by ? identified the presence of a large, old, and metal-poor slightly counter-rotating structure in phase space (which they refer to as the “blob”). They concluded that this population is associated with a relatively massive object which, they hypothesised, may have been responsible for the heating of the thick disc. Following up on that result, ? used kinematic, chemical, and age information for a large sample of stars in *Gaia* and APOGEE to identify a population of metal-poor stars with the same phase space characteristics as the “blob”. The distribution of this stellar population in the  $[\alpha/\text{Fe}]\text{-}[\text{Fe}/\text{H}]$  plane, with relatively low  $[\alpha/\text{Fe}]$  and a large spread in  $[\text{Fe}/\text{H}]$ , suggests the chemical evolution trend of a relatively massive system (the recent preprint posting of ?, hints at a similar conclusion, also on the basis of APOGEE data). Moreover, the positions of the stars in the HR diagram are consistent with old ages (10-13 Gyr). According to ?, the accretion of a dwarf galaxy with an approximate mass of the Small Magellanic Cloud (necessary to explain the chemistry of this accreted population, ?)  $\sim 10$  Gyr ago may have been responsible for the heating of the thick disc. The notion that the thick disc was formed from the vertical heating of a thinner progenitor disc competes with the so-called ‘upside-down’ formation scenario (see, e.g. ??) according to which the early gaseous disc was thick as a result of strong stellar feedback, and slowly settled as the star formation waned to form the thinner components of the disc. Despite their differences, both scenarios are consistent with at least some heating of the stellar disc by satellite mergers, which in turn are also likely necessary to explain the flaring of high  $[\alpha/\text{Fe}]$  mono-age disc populations (e.g. ??). In general, recent observational results do not seem to point towards a scenario where the thick disc formed thin and was heated entirely by mergers, which would produce a plateau in the age or  $\alpha$  abundance against scale height relationship that is not currently borne out by the data (e.g. ???????)

In addition to, and in support of these findings, ? recently inferred that the Milky Way has had a rather atypical assembly history given its mass, based on analysis of the age-metallicity relation of Galactic GCs. They found that the assembly rate of the Milky

Way was among the uppermost quartile of galaxies in their simulation, and identified three recent massive accretion events. According to those authors, two of the accretion events were proposed to correspond to the Sagittarius dwarf and Canis Major. The most massive of the identified accretion events is suggested to have no known debris, and have a stellar mass  $> 10^9 M_\odot$ , and correspond to GCs that reside close to the Galactic center. It seems possible, given the evidence in the GC population, that the accreted satellite identified by ? and ? corresponds to the Canis Major debris identified in that work, given that the ‘sausage’ GCs identified by ? are further out in the halo, and the Canis Major GCs were those at Galactocentric distances  $> 10$  kpc. The finding that the assembly history of the Milky Way is atypical is also consistent with the work of ?, who found that Milky Way stellar mass galaxies in the EAGLE simulation with  $[\alpha/\text{Fe}]$  abundance patterns similar to the Milky Way had atypical dark matter accretion histories, characterised by early, rapid accretion, which slowed at late times.

In summary, the local stellar halo has been shown to be dominated by a population of moderately metal-poor, low  $[\alpha/\text{Fe}]$ , old stars on highly eccentric orbits. This population is the likely remnant of a major accretion event that took place at about the same time that the Galactic disc was itself forming. These results have important implications, which prompted us to examine the chemical and kinematic properties of the newly discovered stellar population in detail. In this paper we present an analysis of the abundance pattern of stars in common between the *Gaia*-DR2 and APOGEE-DR14 catalogs, and discuss the implications of their kinematic properties in light of the EAGLE suite of numerical cosmological simulations. We extend the studies of the element abundances in these populations to include odd- $Z$  and Iron peak elements, and examine the detailed kinematics of stars in sub-populations defined by abundances and orbit eccentricity. We also extend previous theoretical work on this population by examining the kinematics of accreted debris from a fully self-consistent cosmological simulation that provides a cosmologically motivated sample of accreted satellite debris onto Milky Way mass haloes. In Section 3.2 we describe our sample selection and orbital parameter determination, as well as the details of the EAGLE simulations. In Section 3.3 we discuss the chemical and kinematic properties of this population. In

Section 3.4 we contrast the kinematic properties of the newly discovered stellar population with the expectations from cosmological numerical simulations. Our conclusions are summarised in Section 3.5.

## 3.2 Sample and Data

### 3.2.1 APOGEE DR14

Our study is based on a cross-match between the SDSS-APOGEE DR14 and *Gaia* DR2 catalogues. APOGEE (?) is a near infrared spectroscopic survey of the stellar populations of the Galaxy and its Local group neighbours. The data employed in this paper come from the DR14 catalogue (?), which comprises a re-reduction and analysis of APOGEE-1 data (from SDSS-III, ?), alongside a set of newly reduced and analysed observations from APOGEE-2 (taken as part of SDSS-IV, ?). APOGEE DR14 contains high S/N,  $R \sim 22,500$  spectra, radial velocities, stellar photospheric parameters, and element abundances for over 270,000 stars in the  $H$ -band ( $1.5\text{--}1.7\mu\text{m}$ ). Observations are carried out using the 2.5m SDSS Telescope at Apache Point Observatory (APO) (?), and fibre-fed to the APOGEE spectrograph (?). Targeting is performed so as to simplify as much as possible the survey selection function whilst preferentially selecting red giant stars, by employing selection bins in the apparent  $H$ -band magnitude, and a simple colour selection in dereddened  $(J - K)_0$  (??). Spectra are reduced, combined and then analysed through the APOGEE data reduction pipeline (?), and the APOGEE Stellar Parameters and Chemical Abundances Pipeline (ASPCAP, ?). ASPCAP relies on a pre-computed library of synthetic stellar spectra (?) computed using a customised linelist (?) to measure stellar parameters, 19 element abundances and heliocentric radial velocities of MW stars (?). Abundances are well tested against samples from the literature (?; in press.). We use distances for stars in APOGEE DR14 measured by the Brazilian Participation Group (BPG, ?), included in a publicly available Value-Added Catalogue (VAC). These distances are measured using an early version of the StarHorse code (?), and combine spectroscopic and photometric information to make

a Bayesian distance estimation. The expected precision of these measurements is expected to be  $\sim 15\%$ , which we determine to be similar to distance estimates derived from the current *Gaia* parallaxes at the range of distances spanned by our sample of interest. Given that the parallax measurements can be uncertain in some cases, and especially so for distant stars, we believe the use of spectro-photometric distances to be well motivated.

We examined the distribution of our sample stars in chemical composition space considering all elemental abundances available in the APOGEE DR14 catalog. However, in this paper we choose to focus on the abundances of Fe, Mg, Al, and Ni, which are the ones providing interesting insights into the nature of the accreted halo stellar population. The elemental abundances are measured as part of the ASPCAP pipeline, which uses a two-step process. First, the stellar parameters  $T_{\text{eff}}$ ,  $\log(g)$ ,  $v_{\mu}$ , [M/H], [ $\alpha$ /M], [C/M], and [N/M] (where  $v_{\mu}$  is the micro-turbulent velocity) are determined via a global fit to the aforementioned spectral library (?). The individual element abundances are then calculated by adjusting the [M/H] ([C/M] and [N/M] for Carbon and Nitrogen, and [ $\alpha$ /M] for  $\alpha$  elements) of the best-fit spectrum, and finding the best match to the observed spectrum in windows around features in the spectrum which are dominated by each element. The abundances are then all estimated consistently, and can then be calibrated internally relative to open cluster observations. The internal calibrations are performed to account for systematic abundance variations with  $T_{\text{eff}}$ . In DR14, an external calibration is applied that forces the abundance ratios of solar metallicity stars located near the solar circle to be equal to solar (?; in press). This small zero-point correction should be taken into consideration when making comparisons between our results and other data.

### 3.2.2 *Gaia* DR2 and cross matching

The ESA-*Gaia* mission is a space-based astrometric survey which is providing an unprecedented mapping of MW stars in phase space. The second data-release, *Gaia* DR2 (?), provides 5-parameter astrometry (proper motions, positions and parallaxes)

for over 1.3 million objects in the Galaxy. Combined with accurate radial velocities and spectro-photometric distance estimates from APOGEE DR14, these data make possible the calculation of 6D phase space coordinates for each object. Many improvements were made to the data-processing between *Gaia* DR1 (?) and DR2, examples of which include: improvements to the source detection algorithm, better modelling of the spacecraft attitude, and the fact that DR2 uses its own reference frame based on quasars (whereas DR1 was tied to the *Tycho-2* and HIPPARCOS catalogues for proper motion measurements). As a result of these improvements, the typical uncertainty on astrometric parameters is expected to be  $\sim 0.2$  to  $0.3$  mas in the middle of the magnitude range (going up to  $\sim 2$  mas for the faintest sources). While the exact selection function of *Gaia* is as yet not well known, DR2 has improved completeness in bright stars, and the survey is expected to be complete between  $G = 12$  and  $17$ .

We perform a cross-match between APOGEE DR14 and *Gaia* DR2 using the CDS X-match service<sup>1</sup> and adopting a conservative position mismatch tolerance of  $0.5''$ . We find that the raw APOGEE DR14 catalogue has 254,789 matched objects in *Gaia* DR2 ( $\sim 99\%$ ), 83,189 of which have full 6D phase-space coordinates (using APOGEE radial velocities), have no warning or bad flags from the APOGEE reduction and AS-PCAP analysis, and were not observed during commissioning of the APOGEE instrument (the main factor that reduces the sample size are the APOGEE data quality flag cuts). Of these objects, 81,491 have reliable distance measurements in the APOGEE DR14 distance VAC. We transform the observed data into the Galactocentric coordinate frame, assuming the solar motion of ?, propagating the observational uncertainties while accounting for the correlation between errors in the *Gaia* data. The sample extends from Galactocentric cylindrical radii  $R \sim 3$  kpc out to  $R > 15$  kpc, reaching up to a maximum of 10 kpc away from the midplane. Throughout the paper, we assume the solar radius  $R_0 = 8$  kpc, and its distance from the midplane  $z_0 = 0.025$  kpc.

Stars located within  $r = 3 r_{\text{tidal}}$  of the centres of known globular clusters were excluded from the sample. Tidal radii,  $r_{\text{tidal}}$ , and cluster centres were adopted from the

---

<sup>1</sup><http://cdsxmatch.u-strasbg.fr/xmatch>

2010 edition of the ? catalog<sup>2</sup>. This conservative cut removes 19 stars, after removal of stars not belonging to the main APOGEE sample (e.g., stars from APOGEE ancillary science programs).

### 3.2.3 Orbital parameters

To study the kinematical structure of the halo population in the APOGEE-*Gaia* catalogue, it is necessary to estimate the orbital parameters of the stars and their associated uncertainties robustly. To make these estimates, we use the fast orbit parameter estimation method of ?, which adapts the Stäckel fudge method for estimating action-angle coordinates in axisymmetric potentials (presented in ?) to directly estimate the orbital eccentricity,  $e$ , apo- and pericentre radii,  $r_{\text{ap}}$  and  $r_{\text{peri}}$ , and the maximum vertical excursion,  $Z_{\text{max}}$ , to high precision and without recourse to orbit integration (which can make the proper propagation of uncertainties computationally costly at this scale). We also estimate the orbital actions,  $J_R$ ,  $L_Z$ , and  $J_Z$  for each star via the same method. All estimates are performed using the implementation of the Stäckel approximation in the python package `galpy` (?). For each star, we Monte-Carlo (MC) sample the errors by constructing the covariance matrix of the observed data. We sample 100 realisations of the observed coordinates of each star, and compute the orbit parameters and actions for each sampled point, cataloguing the median value of the samples for each parameter, their standard deviation, and the correlation between parameters.

### 3.2.4 The EAGLE simulations

In Section 3.4 we undertake a simple analysis of simulated galaxies from the EAGLE suite (??). EAGLE models the formation and evolution of galaxies in the context of  $\Lambda$ CDM cosmology. The simulations are run using a version of the smoothed particle hydrodynamics (SPH) and TreePM gravity solver GADGET 3 (described most recently by ?), modified to include the ? pressure-entropy formulation of SPH, a time-step

---

<sup>2</sup><http://physwww.mcmaster.ca/~harris/mwgc.dat>

limiter (?), and switches for artificial viscosity and conduction (as proposed by ??). EAGLE produces a realistic population of galaxies by virtue of the calibration of its feedback efficiency to the observed galaxy stellar mass function (GSMF), the stellar vs. black hole mass relation and galaxy disc sines, but has been shown to reproduce a broad range of observed galaxy properties and scaling relations, such as the Tully-Fisher relation (?), colour-magnitude relationships (???), and galaxy size evolution (?). All particle data and galaxy catalogues are now available publicly (see ?) and are accessible online<sup>3</sup>.

The EAGLE suite offers various box sizes ranging from 12.5 to 100 cMpc on a side. Here, we only examine the higher resolution simulation adopting the ‘Recalibrated’ model parameters (see ?), referred to here as L025N752-Recal. The motivation behind this decision is the better resolution of small dwarf galaxies, and therefore better sampling of the accreted galaxy population within the EAGLE haloes. L025N752-Recal has dark matter particles of mass  $1.21 \times 10^6 M_{\odot}$  and an initially equal number of SPH particles with mass  $2.26 \times 10^5 M_{\odot}$ , adopting a Plummer-equivalent gravitational softening length  $\epsilon_{\text{com}} = 1.33 \text{ ckpc}$ , limited to a maximum proper length of  $\epsilon_{\text{prop}} = 0.35 \text{ pkpc}$ . We select a sample of galaxies which have virial masses roughly equal to that proposed for the Milky Way, between  $M_{200} = 0.8$  and  $2.0 \times 10^{12} M_{\odot}$ . In the L025N752-Recal simulation, this corresponds to  $N = 22$  galaxies with a wide range of stellar masses, and a range of assembly and accretion histories. This sample makes a good testbed for understanding the origin of satellite debris in the Milky Way, allowing us to study the  $z = 0$  characteristics of a diverse sample of satellite galaxies accreted onto Milky-Way-like haloes.

To calculate the eccentricities for the simulated star particles, we solve (using the bisection method) the equation

$$L^2 + 2r^2(\Phi(r) - E) = 0, \quad (3.1)$$

where  $L$  is the angular momentum,  $\Phi(r)$  the gravitational potential and  $E$  the total

---

<sup>3</sup><http://galaxy-catalogue.dur.ac.uk>

energy of the particle. For a bound orbit the equation has two solutions (the peri- and apocentre distances,  $r_{\text{peri}}$  and  $r_{\text{ap}}$ ), which are equal for a perfectly circular orbit (? , eq. 3.14). Unbound particles are disregarded. The eccentricity is then calculated as

$$e = \frac{(r_{\text{ap}} - r_{\text{peri}})}{(r_{\text{ap}} + r_{\text{peri}})}. \quad (3.2)$$

### 3.3 The high eccentricity halo population

As mentioned above, ? used APOGEE-DR14 abundances to show that a stellar population they initially identified in phase space occupies a distinct locus in the  $[\alpha/\text{Fe}]$ - $[\text{Fe}/\text{H}]$  plane. Among all  $\alpha$  elements available from APOGEE spectra, Mg is the one for which abundances are the most reliable in the metal-poor regime, due to the number of available lines and their strength at low metallicity. Therefore we decide to first look at how stellar populations are distributed in the Mg-Fe plane as a function of orbital eccentricity. We show the  $-\text{[Fe/H]}$  distribution of APOGEE DR14 in Figure 3.1, where the greyscale is such that stars with higher orbital eccentricity  $e$  are represented by darker symbols.

Three main groups of stars are apparent in  $-\text{[Fe/H]}$  space, which we indicate using solid and dashed black lines (the dotted gray line indicates the upper limit imposed on  $[\text{Fe}/\text{H}]$  for the analysis in Section 3.3.1). The focus of this paper is on the group we call the *accreted halo*, which occupies the same locus as the stellar population identified by other groups as associated to a major accretion event (see Section 3.1). It also corresponds to the “LMg” population identified by ? and? on the basis of APOGEE DR13 chemistry and kinematics. It extends between  $([\text{Fe}/\text{H}], ) \sim (-2.0, 0.3)$  to  $\sim (-0.5, -0.1)$  and is dominated by high eccentricity stars. The other groups are the well known high- $\alpha$  and low- $\alpha$  *disc* populations, characterised in detail in several previous studies (e.g. ?????), and commonly conflated with the thick and thin discs, respectively. As expected, the latter populations are dominated by stars in very circular orbits, although the high- $\alpha$  group contains a non-negligible population of stars in fairly eccentric orbits (e.g.  $> 0.7$ )—a topic that will be explored in a future study.

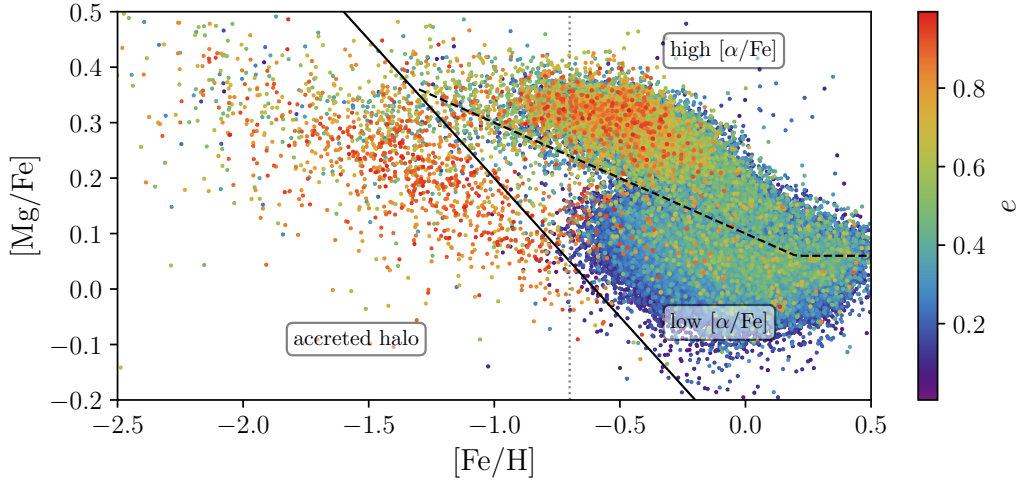


Figure 3.1: The  $-[\text{Fe}/\text{H}]$  plane in APOGEE DR14, coloured by orbital eccentricity  $e$ , as estimated using the method of ?. The points are plotted with the highest  $e$  stars overlaying the points at lower  $e$ , such that the highest  $e$  populations stand out. It is clear that a population extends from  $([\text{Fe}/\text{H}], [\text{Mg}/\text{Fe}]) \sim (-2.0, 0.3)$  to  $\sim (-1.0, 0.1)$  that appears to consist mainly of stars on highly eccentric orbits, with a distinct element abundance pattern to that of the Galactic disc (at  $[\text{Fe}/\text{H}] > -0.7$ ). The dotted gray line reflects the cut in  $[\text{Fe}/\text{H}]$  which is imposed to perform the  $k$ -means analysis.

Careful inspection of the ‘accreted halo’ stars in Figure 3.1 suggests that there is some dependence of  $e$  on eccentricity, in that stars with higher  $e$  have slightly lower  $e$ . Further examination of the data suggests that the same was the case for  $\alpha$  and possibly  $\text{Fe}$  and to a lesser extent  $[(\text{C}+\text{N})/\text{Fe}]$ . This finding motivates us to attempt an identification of sub-structure in chemo-kinematic space in an objective and data-driven fashion, so as to avoid “cherry-picking” arbitrary selection limits in various parameters. In this way we hope to characterise the populations in the accreted halo regime by subdividing its member stars into meaningful groups. We use the scikit-learn  $k$ -means clustering algorithm (?) in the space of  $[\text{Fe}/\text{H}]$ ,  $\alpha$ ,  $\text{Fe}$ , and eccentricity  $e$ . The choice of these parameters is guided by the fact that, on one hand, these elements fall into the main groups:  $\alpha$ , odd-z and Fe peak elements, respectively, and on the other hand it appears, at least from Figure 3.1, that eccentricity is a useful discriminator between disc and accreted halo populations. We limit the maximum  $[\text{Fe}/\text{H}]$  to  $-0.7$ , to minimise contamination by disc stars, finding that high  $e$  stars in the low  $[\alpha/\text{Fe}]$  disc locus at higher  $[\text{Fe}/\text{H}]$  are not chemically similar to those in the ‘accreted halo’ population and can be confidently disregarded. We set the assumed number of clusters,

$k = 4$ , to anticipate the expected separation of the high and low  $[\alpha/\text{Fe}]$  disc, and then to allow for subdivision of the accreted halo population into any potentially meaningful groups. We find that the algorithm groups the high and low  $[\alpha/\text{Fe}]$  disc stars separately, and finds two clear groups in the lower  $[\text{Fe}/\text{H}]$  space. Setting  $k > 4$  subdivides the lower  $[\text{Fe}/\text{H}]$  groups in an unstable manner, while  $k = 4$  provides very good stability over many iterations of the algorithm. We also test the algorithm at  $k < 4$ , finding that the stability is decreased also at lower  $k$ . If the ‘accreted’ halo group from Figure 3.1 is isolated, using  $k = 2$  clustering can still recover the two groups found when clustering the whole data set. We retain the full data-set and use the  $k = 4$  clustering to avoid resorting to an arbitrary selection of the division between halo and disc stars. Rescaling the data and re-running the clustering provides little difference to the results. It is worth noticing that both accreted halo populations have lower abundance ratios than thick disc stars (in the region where they overlap in  $[\text{Fe}/\text{H}]$ ) for C+N, Si, K, Ca, Ti, and possibly also Mn.

We show the eccentricity distributions of the  $k$ -means groups in Figure 3.2. The high and low  $[\alpha/\text{Fe}]$  disc groups are combined into a single group here, as these stars are not of interest to this work, except as a comparison sample. The halo stars are separated into one group with intermediate eccentricities, peaking at  $e \sim 0.5$ , and a group with very high eccentricity, peaking at  $e \sim 0.9$ . The lower  $e$  population distribution is fairly broad whereas the high  $e$  population is very strongly peaked toward the highest  $e$  values (with some small skew to low  $e$ ). The high and low  $e$  groups contain 679 and 318 stars, respectively. We also show the  $k$ -means groups in - space in Figure 3.3. This abundance plane was shown by ? to discriminate well between accreted and in-situ stellar populations in the Milky Way, with the former occupying the low , low region of the plot. Indeed, we find that the accreted halo population separates out from the disc population very clearly in this plane, being characterised by lower Al and Mg abundances. Moreover, while there is considerable overlap between high and low  $e$  populations in this abundance plane, the high  $e$  group occupies a lower locus, on average, in this plane compared to the low  $e$  group.

In conclusion, the results above show that once APOGEE chemical compositions are

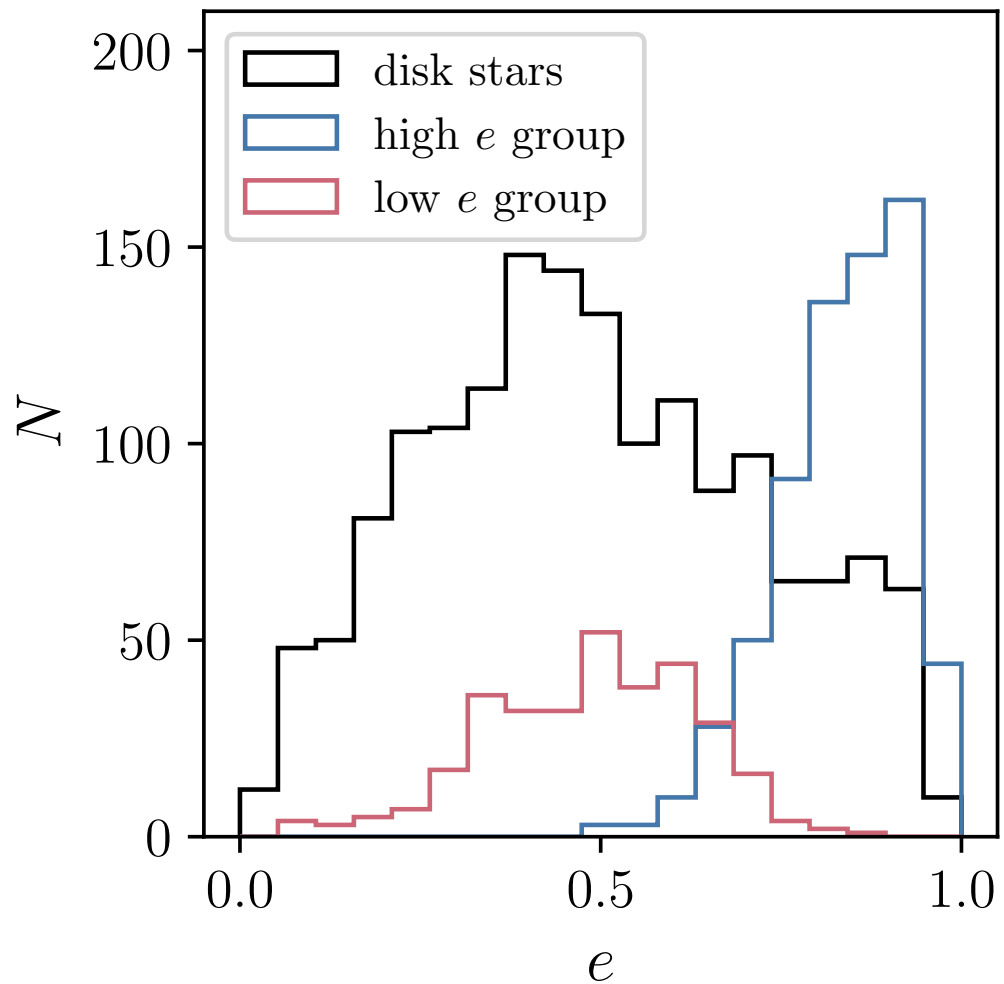


Figure 3.2: Eccentricity distributions of stars in three groups identified by performing a  $k$ -means detection of structure in the eccentricity-[Fe/H]--- space. The  $k$ -means algorithm cleanly separates the accreted halo component into two groups, one characterised by low eccentricities (in red), and the other with a peak at very high  $e$  (in blue). We show the stars assigned to the disc (with  $[\text{Fe}/\text{H}] < -0.7$ ) in black as a comparison sample.

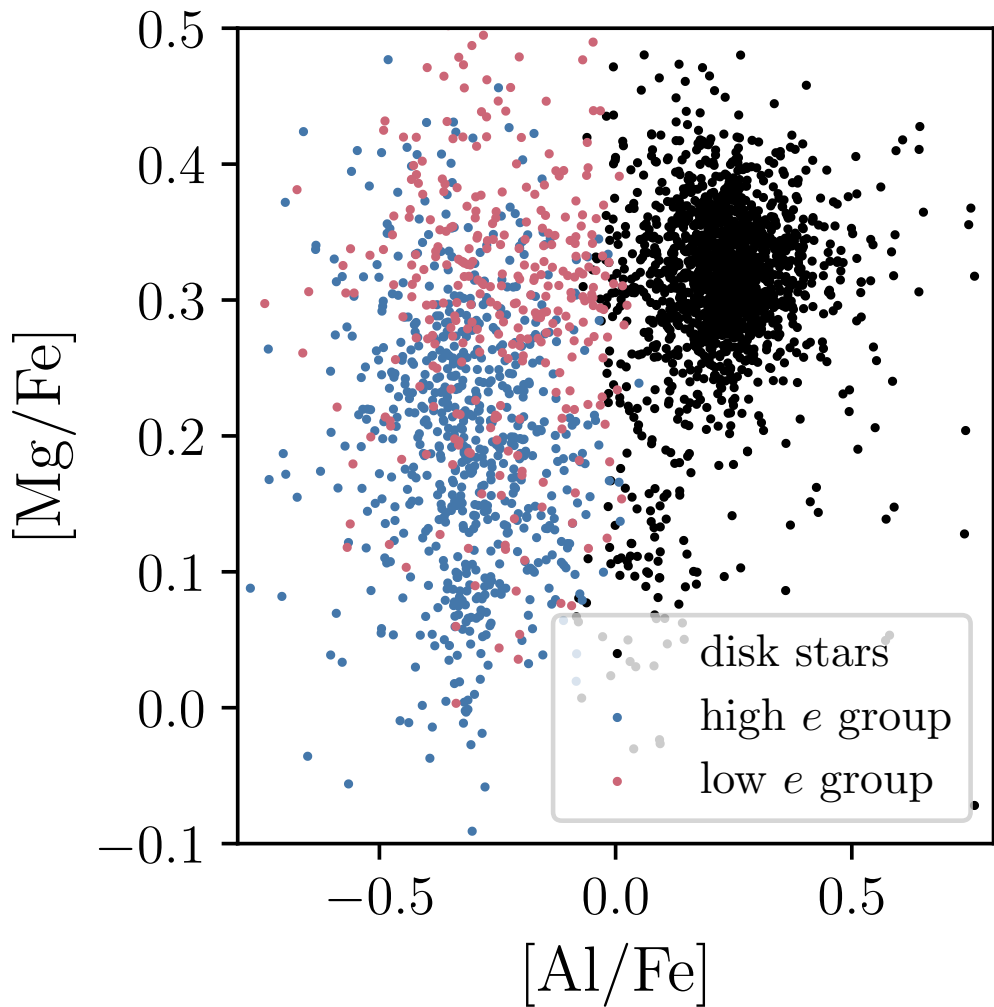


Figure 3.3: Distribution of the stars in the different  $k$ -means groups in the - plane. High  $e$  stars occupy preferentially the low , low region of the plot, a locus which was identified in ? as being common to accreted halo populations. Low  $e$  group stars tend to be more distributed at higher and slightly higher . Discdisc stars (in black) are enhanced in Al and, to a lesser extent, Mg, relative to the high and low  $e$  groups.

combined with kinematics inferred from Gaia DR2 distances and proper motions,  $\sim 2/3$  of the stars in the accreted halo population identified in previous studies are characterised by highly eccentric orbits. In the following sub-sections we examine the properties of this population in both orbital and element abundance space compared to those of their low  $e$  counterparts.

### 3.3.1 Chemical Compositions

#### Metallicity Distributions

In this Section we examine more closely the chemical compositions of the accreted halo populations, keeping track of the differences between the the high and low  $e$  groups. We start by examining the metallicity distribution function (MDF) of these populations. The *raw* MDFs are displayed in Figure 3.4, and are *not* corrected for the APOGEE selection function. Correction for selection function effects can not be performed to the full sample of stars studied here, as many of the sample stars belong to magnitude bins on plates where observations were incomplete in DR14 and so are not part of the statistical sample (see ??, for details on the selection function of APOGEE and the targeting strategy, respectively). For this reason, the corrected MDF of stars in DR14 which could be corrected for is plagued by noise due to low number statistics, particularly in the case of the (smaller) low  $e$  population sample. We nevertheless compared the lower  $N$ , corrected and raw MDFs for the larger high  $e$  sample, which is statistically more robust, finding them to be in good overall agreement with similar peak position and width. Therefore, we can confidently compare the MDF of the high  $e$  population with those of others systems, at least to first order. In addition, it is safe to assume that relative differences between the MDFs of the high and low  $e$  populations are not affected significantly by selection biases from the targeting strategy, and that any differences in the MDFs are likely to be real.

With the above caveats in mind, examining Figure 3.4 we learn that the MDF of the high- $e$  population peaks at  $[\text{Fe}/\text{H}] \sim -1.3$  and has a width of approximately 0.6 dex

(FWHM), with a tail towards the metal-poor end, resembling the MDF of a classical closed-box model. Its MDF is in fact qualitatively similar to those of dwarf galaxies in the Local Group (e.g. ?), and in particular quite similar to those of the Small Magellanic Cloud (SMC, ?) and Leo I (?). This is an interesting result given that ? showed that their LMg population (of which the high- $e$  stars are a sub-group) had a star formation history similar to that of massive dwarfs like the LMC prior to its accretion, which would have likely been around present day SMC mass ( $\sim 3 \times 10^8 M_\odot$ , e.g. ??) at the time that the LMg population was accreted (??).

It is also instructive to compare the MDFs of the high and low  $e$  populations. The most striking difference is that the MDF of the low  $e$  population has no strong peak, but rather two smaller (likely significant) peaks at lower metallicities. The sharp edge at  $[Fe/H]=-0.7$  is due to the  $[Fe/H]$  limit adopted in our  $k$ -means grouping, and the smaller peak of the low  $e$  population at  $[Fe/H]>-1.0$  is probably due to disc contamination. Interestingly, the two peaks towards the lower metallicity end happen at similar metallicities to those previously assigned to the inner and outer halo populations (e.g. ???). Most importantly, the MDFs of the high and low  $e$  populations are strikingly different, and this difference is almost certainly insensitive to selection effects, which then strongly suggests that the two populations have different origins.

It is not entirely clear how the difference in shape between the MDFs of the high and low  $e$  populations can be understood in terms of the halo accretion history. While the MDF of the high  $e$  population lends support to the notion that those stars were injected into the halo as part of one major accretion event, it is hard to draw any strong conclusion regarding the low  $e$  population.

### Abundance Ratios

In this section we inspect abundance ratios of the high and low  $e$  groups, to gain further insights into the origins of these two populations. Figure 3.5 displays the run of  $[Mg/Fe]$ ,  $[Al/Fe]$ , and  $[Ni/Fe]$  as a function of  $[Fe/H]$ . For each element we take the running median and interquartile range of  $[X/Fe]$  as a function of  $[Fe/H]$ . We calculate

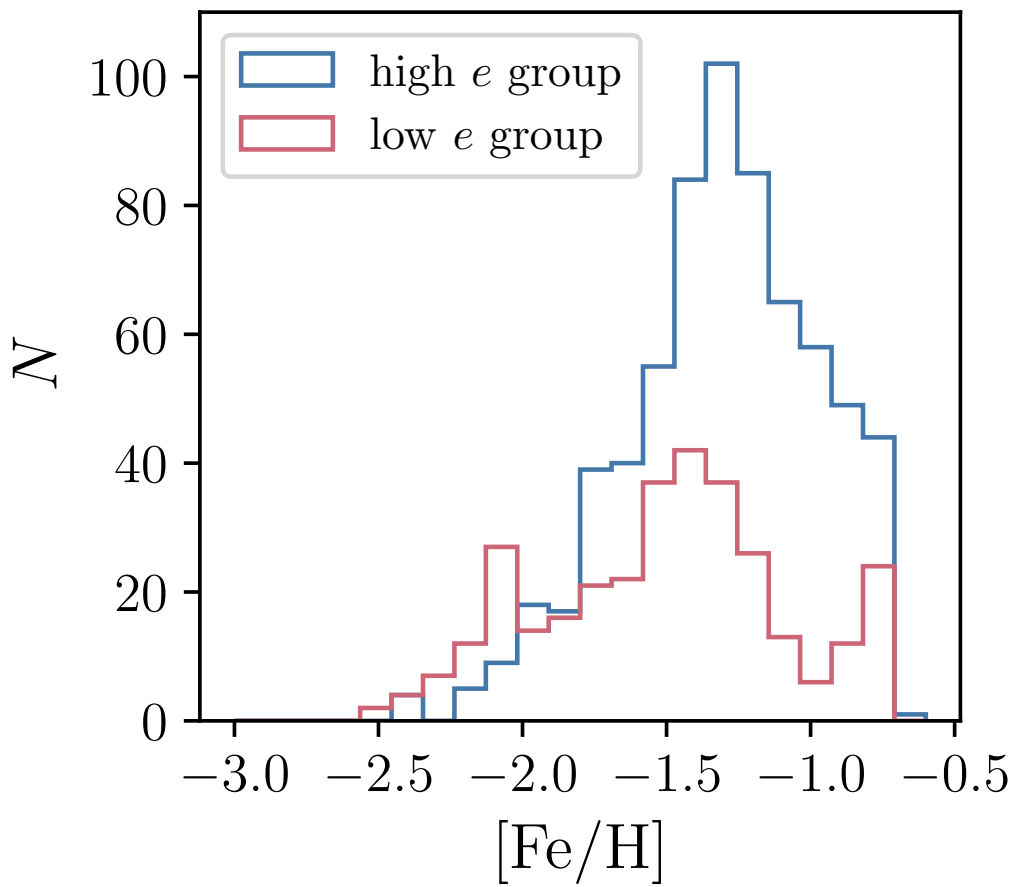


Figure 3.4: The raw metallicity distribution functions of the high and low  $e$  populations. Unlike their low  $e$  counterparts, the high  $e$  population shows a strong peak at about  $[Fe/H] \sim -1.3$ , resembling MDFs of Local Group dwarfs. The low  $e$  group shows peaks at both  $[Fe/H] \sim -2.1$  and  $\sim -1.4$ , and stars piled up at the imposed upper  $[Fe/H]$  limit at  $[Fe/H] = -0.7$ .

the median abundance in bins of 50 stars sorted by increasing [Fe/H], which is shown by the red and blue coloured bands for the high and low  $e$  populations, respectively.

The top panel shows that in general,  $\text{[Mg/Fe]}([e])$  decreases with [Fe/H], and both the high and low  $e$  populations have lower  $\text{[Mg/Fe]}$  than that of the high- $\alpha$  disc stars at same [Fe/H], in the metallicity interval where the two populations overlap ( $-1.5[\text{Fe}/\text{H}] - 0.5$ ), as previously discussed by ? and ?. Moreover, the high and low  $e$  populations occupy slightly separated sequences, such that the former has lower  $\text{[Mg/Fe]}$  at fixed [Fe/H]. It appears from the simple running median that the high  $e$  population exhibits a change in slope of  $\text{[Mg/Fe]}([e])$  against [Fe/H], at  $[\text{Fe}/\text{H}] \sim -1.3$ , whilst there is only slight evidence change of slope in the lower edge of the low  $e$  relation. In order to test this further, and to determine more rigorously the location of the change in slope, we use a Bayesian inference to determine a generative model for the  $-\text{[Fe/H]}$  distribution of both populations. The full procedure is outlined in Appendix 3.6, the basic principle being that we fit a piecewise-linear model to the data of the form:

$$\text{[Mg/Fe]}([\text{Fe}/\text{H}]) = \begin{cases} m_1[\text{Fe}/\text{H}] + b_1 & [\text{Fe}/\text{H}] < [\text{Fe}/\text{H}]_0 \\ m_2[\text{Fe}/\text{H}] + b_2 & [\text{Fe}/\text{H}] > [\text{Fe}/\text{H}]_0 \end{cases} \quad (3.3)$$

where  $m_{[1,2]}$  and  $b_{[1,2]}$  are the slope and  $y$ -intercept either side of the break, which is positioned at  $[\text{Fe}/\text{H}] = [\text{Fe}/\text{H}]_0$ . The fitting procedure accounts for the error on both  $\text{[Mg/Fe]}$  and [Fe/H], allowing a proper assessment of the significance of any fitted breaks. If there is no break in the range of  $\text{[Mg/Fe]}$  and [Fe/H] considered, the data are fit by a simple linear relation, as the break is pushed to the edge of the [Fe/H] range.

We show the models fitted to the high and low  $e$  groups in Figure 3.6. The data for each group are plotted in the black points, and the best fit and 95% confidence interval are shown by the line and coloured bands in each panel. The high  $e$  group model, shown in the top panel, has a change of slope found at high significance, indicated by the dashed crosshair, positioned at  $[\text{Fe}/\text{H}] = -1.31^{+0.03}_{-0.06}$  and  $= 0.22^{+0.01}_{-0.08}$ . The slope to the metal-poor side of the break is found to be  $-0.15 \pm 0.01$ , and is roughly consistent with the slope before the break in the high  $e$  disc star sequence (e.g. that seen in ?). A similar

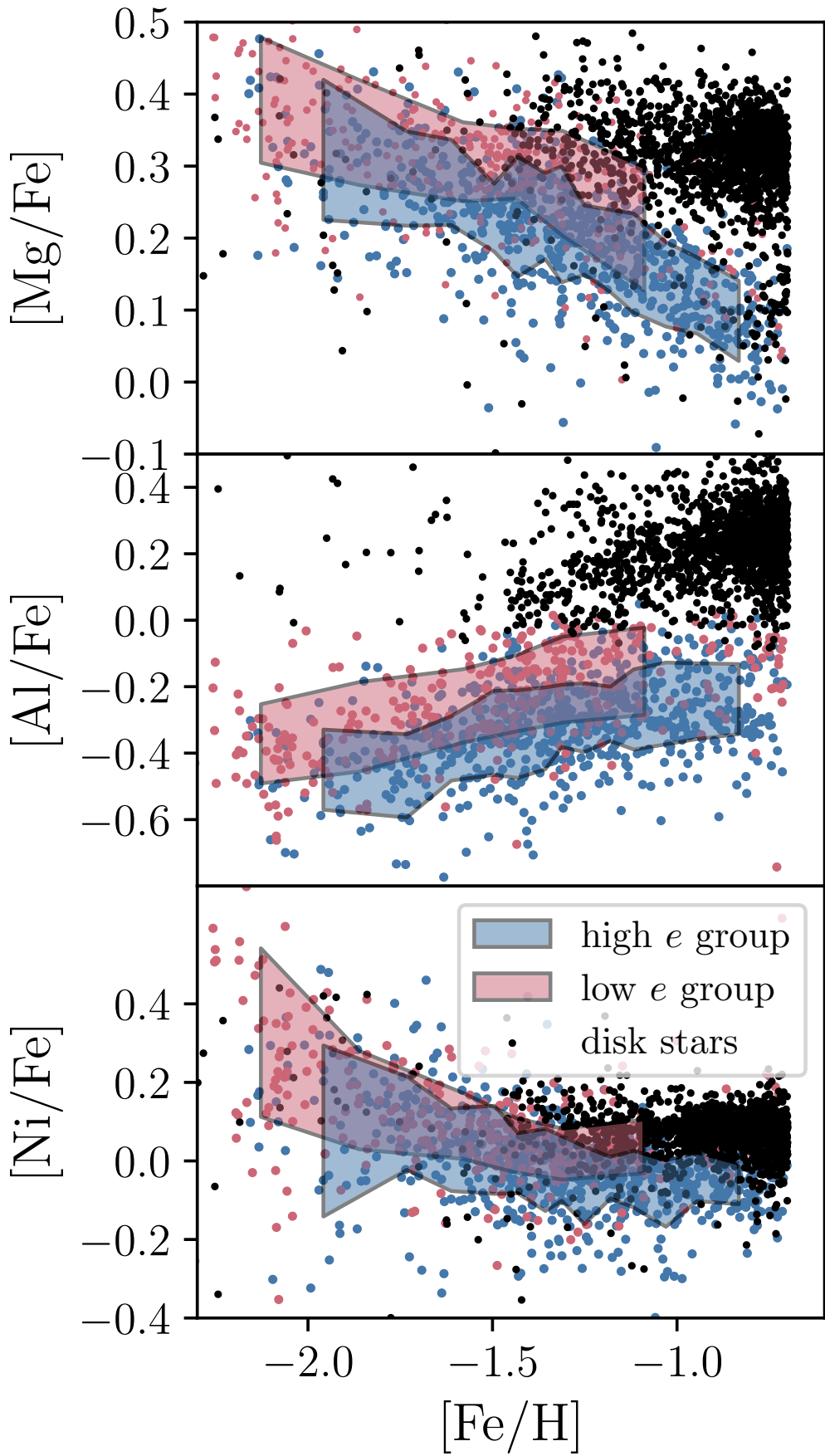


Figure 3.5: The Magnesium, Aluminium and Nickel abundances of the  $k$ -means groups. These elements are good representations of  $\alpha$ , odd- $Z$  and Fe peak elements that are measured by APOGEE. The  $e$  value is the orbital eccentricity, calculated from a fit of 50 radial velocity data points.

metal-poor end slope is also present in the work of ?, who used APOGEE DR12 data to determine also that a change of slope is present in low  $e$  stars, located at  $[\text{Fe}/\text{H}] \sim -1.0$  dex, in rough agreement with that found here. At  $[\text{Fe}/\text{H}] > [\text{Fe}/\text{H}]_0$ , the slope steepens to become  $-0.26 \pm 0.01$ . The low  $e$  population is well fit in this range of  $[\text{Fe}/\text{H}]$  by a simple linear relation with a slope equal to  $-0.14 \pm 0.01$ , with no significant break found. As it is likely that at least some of the stars at the highest  $[\text{Fe}/\text{H}]$ , and at high  $e$  in this population are high  $[\alpha/\text{Fe}]$  disc contaminants, we also perform the same fit using stars at  $[\text{Fe}/\text{H}] < -1.0$  dex, and still find no evidence of a break at the same position as that found in the high  $e$  group. Fitting only low  $e$  stars with  $[\text{Fe}/\text{H}] > -1.1$  dex, we find that the best fit is a single linear relation with a slope equal to that found when using the whole low  $e$  group.

This change of slope in the  $-[\text{Fe}/\text{H}]$  relation of the high  $e$  population offers important clues on the nature of this stellar population. It is most straightforwardly interpreted as being due to the onset of Fe enrichment by SNe Ia. The  $[\text{Fe}/\text{H}]$  at which the change of slope occurs is primarily related to the star formation efficiency (e.g. ?), and additionally depends on the gas inflow and outflow rates of its parent galaxy. It follows that it should also be a function of the mass of the parent galaxy, which regulates gas density and gas inflow/outflow. Data for stellar samples from Local Group dwarf galaxies indicate the presence of this same change of slope on the Mg-Fe plane, and it is suggested that the  $[\text{Fe}/\text{H}]$  at which it occurs is higher in galaxies with larger luminosity, and presumably higher stellar mass (see,e.g. ?). Given the  $[\text{Fe}/\text{H}]$  at which data for Local Group dwarf galaxies show a change of slope (see,e.g. ?), we estimate that the mass of the progenitor of this high  $e$  population was somewhere between  $10^8$  and  $10^9 M_\odot$ . This rough mass estimate is in good agreement with that inferred from arguments based on the MDF of the high  $e$  population in Section 3.3.1. It moreover places the mass involved in this accretion event in the range of the total stellar mass of the Galactic halo (?;  $\sim 4 - 7 \times 10^8 M_\odot$ ) which argues against the high  $e$  population belonging to more than one major accretion event, as multiple accretions at this mass would exceed this mass limit.

In contrast, the lack of a clear change of slope in the distribution of the low  $e$  stars

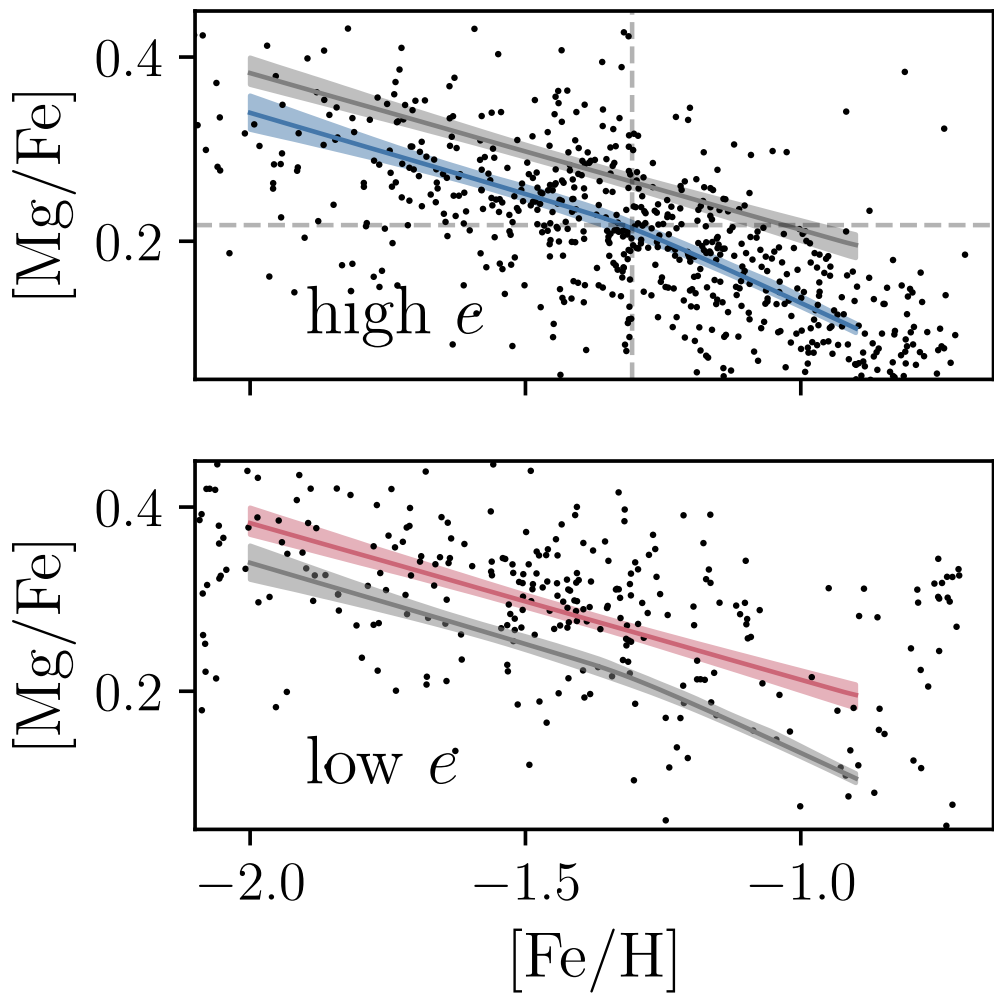


Figure 3.6: The best fit models for  $[{\rm Mg/Fe}]$  as a function of  $[{\rm Fe/H}]$  for the high and low  $e$   $k$ -means groups (shown top and bottom, respectively). The best fit model is shown by the blue and red lines, with the 95% confidence interval marked by the banded blue and red regions either side of this line (the fit for the other group is shown in each panel for reference). The raw data are shown by the black scatter points. The high  $e$  group is well-fit by a model with a break at  $[{\rm Fe/H}] = -1.31^{+0.03}_{-0.06}$  and  $= 0.22^{+0.01}_{-0.08}$ , as indicated by the dashed crosshair. The low  $e$  group is better fit by a single linear relation in the same range of  $[{\rm Fe/H}]$ . The position of the models also demonstrates the slightly higher  $[{\rm Mg/Fe}]$  of the low  $e$  group.

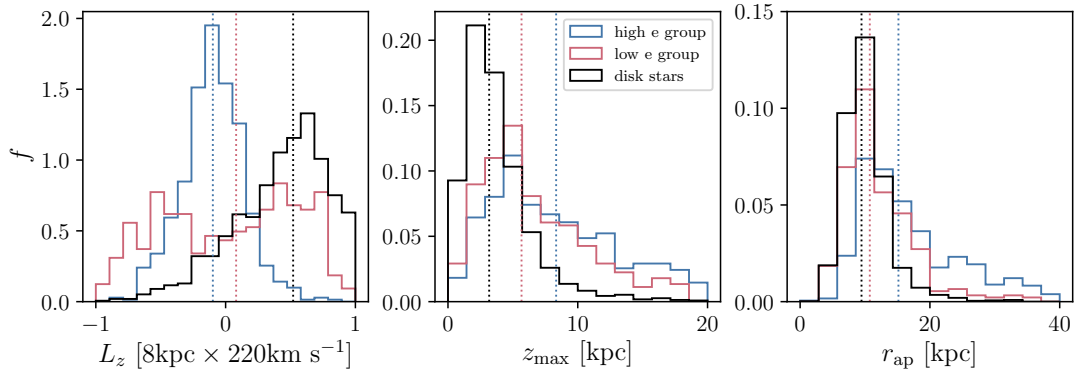


Figure 3.7: The kinematics of the abundance selected stars from Figure 3.1. The distribution of azimuthal angular momentum  $L_z$  (left), maximum vertical excursion from the disc plane  $z_{\max}$  (centre), and the spherical apocentre radius of orbits  $r_{\text{ap}}$  (right), is shown for the high and low  $[\alpha/\text{Fe}]$  disc (red and yellow, respectively) and the accreted halo population (blue). The halo stars clearly occupy a very different orbital distribution, having low  $L_z$ , and distributions of  $z_{\max}$  and  $r_{\text{ap}}$  that extend to very large distances. The median  $L_z$  is slightly negative, while the median  $z_{\max}$  and  $r_{\text{ap}}$  are  $\sim 10$  and  $\sim 20$  kpc, respectively. All histograms are normalised such that the summed probability under *each* group is equal to unity.

on the Mg-Fe plane, argues strongly for this group being in fact some mix of stellar populations with various origins, including stars accreted in different smaller events, stars formed *in situ*, ejected members of the disc, remnant contamination from the high  $e$  group.

The middle panel of Figure 3.5 shows the run of  $\epsilon$  with  $[\text{Fe}/\text{H}]$ . As pointed out by ?, the accreted populations are characterised by much lower  $\epsilon$  than the disc populations at same  $[\text{Fe}/\text{H}]$ . In fact,  $\epsilon$  in this system is comparable to that of stars in the Sagittarius dwarf spheroidal (?). Also very interestingly, the high and low  $e$  populations occupy separate tracks in  $-\text{[Fe}/\text{H}]$  space, with the high  $e$  population showing lower  $\epsilon$ . For both populations  $\epsilon$  increases with  $[\text{Fe}/\text{H}]$ . As an odd- $Z$  element, Al is an important component in the explosive ejecta of massive stars, synthesised in their carbon and nitrogen burning phases. It is also a product of Asymptotic Giant Branch (AGB) stellar nucleosynthesis, particularly at  $[\text{Fe}/\text{H}] > -0.2$  dex (see, e.g. ?). Importantly, it is known that even explosive odd- $Z$  element yields should be metallicity dependent to some extent due to their dependence on a high neutron surplus (e.g. ?). This fact may explain the slight correlation observed between  $\epsilon$  and  $[\text{Fe}/\text{H}]$  in each group and also in the disc populations. The depletion in Al relative to the MW disc in both groups is likely due to

the fact that the MW has seen more metallicity dependent yield of Al, and an increased contribution to the ISM from AGB stars.

While the trend in Ni abundances as a function of [Fe/H] of the high  $e$  group appears to be roughly similar to that of the low  $e$  group, it is noteworthy that the trend is negative in both groups, such that decreases with increasing [Fe/H]. Similarly to the other elements, Ni is slightly depleted in the high  $e$  group relative to the low  $e$  group, but this depletion is very small. At fixed [Fe/H], the high  $e$  group has a lower than the disc stars, whereas the low  $e$  group is nearly consistent with them.

We also studied the other  $\alpha$ , odd- $Z$  and Fe peak elements available in APOGEE. These trends appear to be consistent between most of the elements. It is noteworthy that in almost all elements, the low  $e$  group appears to show slightly higher abundance ratios than the high  $e$  group, at fixed [Fe/H], which may be difficult to explain by invoking lower mass accretion events, unless the star formation in these stellar populations was very short and intense. Our discussion of the EAGLE simulations in Section 3.4 sheds some light on this matter.

### 3.3.2 Kinematics

Figure 3.7 shows the distribution of the  $k$ -means groups in (from left to right) azimuthal angular-momentum  $L_z$  (equivalent to the azimuthal action  $J_\phi$ ), the maximum vertical excursion of orbits above the midplane  $z_{\max}$ , and the apocentric radius  $r_{\text{ap}}$ , which is the maximum orbital distance from the Galactic centre. The median value of each distribution is shown by the coloured vertical dashed line.

It is clear from this plot that the accreted halo groups (again, shown in red and blue) have a very different orbit distribution than the disc stars (in black). The latter are characterised by highly prograde orbits with relatively low vertical excursions. In turn, the two accreted halo populations differ substantially, particularly in terms of their  $L_z$  distributions. The high  $e$  stars all have extremely low angular momentum, such that many of the stars in this population have negative  $L_z$ . The lower  $e$  population has

a large spread in  $L_z$ , such that many stars are on prograde orbits while others have negative  $L_z$ , thus moving on retrograde orbits. The lack of a distinct single peak in  $L_z$  space for the low  $e$  group may indicate again that this group is in fact a superposition of populations with different origins, including the debris of smaller mass accreted satellites, whereas the single, clear peak in  $L_z$  for the high  $e$  group supports the notion that this population is mainly the debris of a single satellite. The median value of  $L_z$  for the high  $e$  stars is  $-176 \text{ km s}^{-1} \text{ kpc}$ . A slightly retrograde motion for stars in the halo at roughly these eccentricities was noted by ? and, as they suggest, could be either an effect of the assumption of the solar motion (which is likely subject to some systematic uncertainties), or could be a true feature of this population, and further supports its origin in a single accreted satellite. We find that a slight retrograde motion of the high  $e$  stars is present when assuming either the ? or ? solar motion measurements, which differ markedly.

The  $z_{\max}$  distribution shows that the stars belonging to the high and low  $e$  populations are on orbits that take them very far above the midplane of the Galaxy, extending to  $z_{\max} > 10 \text{ kpc}$ , as expected for halo stars. The median  $z_{\max}$  of the high  $e$  population is higher than the other two populations, at 8.8 kpc. Similarly, the apocentre radii of these stars extend to very large distances from the Galactic centre with a median  $r_{\text{ap}} = 15.1 \text{ kpc}$ . There appears to be a secondary peak in the distribution at  $r_{\text{ap}} > \sim 25 \text{ kpc}$ , which is roughly consistent with the “apocenter pile up” suggested by ?. Considering that the majority of the stars in the accreted halo population are on highly eccentric orbits ( $e > 0.9$ ) which are strongly out of the disc plane ( $z_{\max} > 10 \text{ kpc}$ ), and have a median apocentre radius which is comparable to that of the accreted halo population analysed by ?, it seems reasonable to conclude that the high  $e$  stars are part of that population.

Further insights into the nature of the high and low  $e$  stellar populations can be gained by inspection of Figure 3.8, where they are displayed together with disc populations on three cylindric coordinate velocity planes. The left panel shows the  $v_R - v_\phi$  plane, where the high  $e$  population has a wide spread in  $v_R$  and a much narrower distribution in  $v_\phi$ . This is the same locus as that of the population identified by ?, their Figure 2. The low  $e$  group, on the other hand, has a clearly bimodal distribution, with two

concentrations above and below the high  $e$  population. The concentration at higher  $v_\phi$  shows *prograde* rotation, overlapping well with the disc population. The grouping at lower  $v_\phi$  is markedly *retrograde*. These two sub-populations are also clearly seen on the right panel, where one can notice that their distributions in  $v_z$  are very similar. The presence of such obvious structure in velocity space calls for a closer scrutiny of those two sub-populations in chemical composition space.

We compared the low  $e$  prograde and retrograde populations in MDF, Mg-Fe, Al-Fe, and Ni-Fe spaces and found them to be, on one hand, indistinguishable from each other but, on the other hand, clearly distinct from the high  $e$  population in all diagnostic plots. It is likely that there is some degree of inter-contamination between all these groups, so that the left panel of Figure 3.8 suggests strongly that the prograde population can be contributed entirely or in part by the disc. This is also suggested by the presence of a secondary peak at the high [Fe/H] end of the low  $e$  MDF (see Figure 3.4) which is dominated by prograde stars. However, quite puzzlingly, the prograde population is chemically indistinguishable from its retrograde counterpart, which is unlikely to be contributed by the disc. We test this further by re-fitting the relation between  $\alpha$  and [Fe/H] for the separated prograde and retrograde components, using the procedure described in Appendix 3.6. We find that in both cases, the best fit relation matches that found for the combined population within the uncertainties, and furthermore, find no evidence of a change in slope in either population. Without further diagnostics with which to make a call on the nature of the distinct low  $e$  populations, we summarise the situation by concluding that it is likely to be a mix of stars contributed by the accretion of the high  $e$  population, smaller accretion events, puffed up disc, and stars formed *in situ*.

## 3.4 Accreted Stellar Populations in EAGLE

We have shown that the accreted stellar halo components observed by APOGEE (characterised by ?) have MDFs and abundance patterns that are similar to those of dwarf galaxies in the Local Group, which we divide into groups in terms of chemistry and

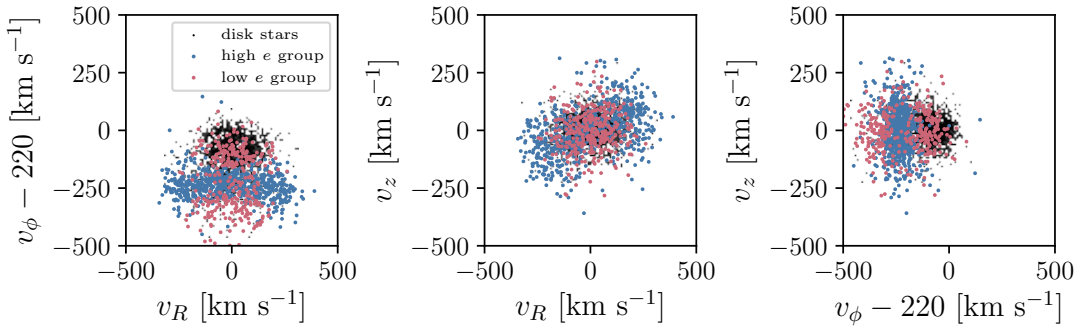


Figure 3.8: Distribution of disc and accreted halo populations in spherical polar coordinate planes. On the left panel, the high  $e$  population occupies the same locus in  $v_R - v_\phi$  space (left panel) as the population identified by ?. The low  $e$  population splits into two populations according to  $v_\phi$ , with one prograde and one retrograde component, suggesting that this population may in fact be from a mix of disc contaminants and debris from smaller satellites.

kinematics (see also ?). One of these groups is characterised by highly eccentric and slightly retrograde orbits, thus sharing similar properties with stellar populations ascribed to a major accretion event in the distant past. In this Section we examine predictions by numerical simulations, drawing parallels with the observations to gain insights into the nature of these accreted halo populations. The questions we intend to address with this exercise are the following: is the high  $e$  population the result of a single relatively massive accretion event, as claimed by other groups? Do the simulations provide insight into the nature of the low  $e$  population? Is it composed of a collection of small accretion events, or is it predominantly formed *in situ*?

The EAGLE simulations are a useful tool to address these questions, as they provide a cosmologically motivated history of satellite accretion for Milky Way-like galaxies, simulated self-consistently in a cosmological context. Therefore, we expect the  $z = 0$  dynamical state of accreted systems around Milky Way analogues in the simulations to be a good approximation to the observations in the Milky Way halo.

To address the above questions, we track star particles formed in galaxies which merged onto disc galaxies that eventually reach a virial mass roughly equal to that of the Milky Way ( $\sim 10^{12} M_\odot$ ). At  $z = 0$ , we measure the orbital eccentricity  $e$  of the star particles resulting from all well-resolved (in this case having  $> 20$  star particles) accretion events of stellar systems with stellar mass  $M_*$ , occurring at redshift  $z_{\text{merge}}$ . The individ-

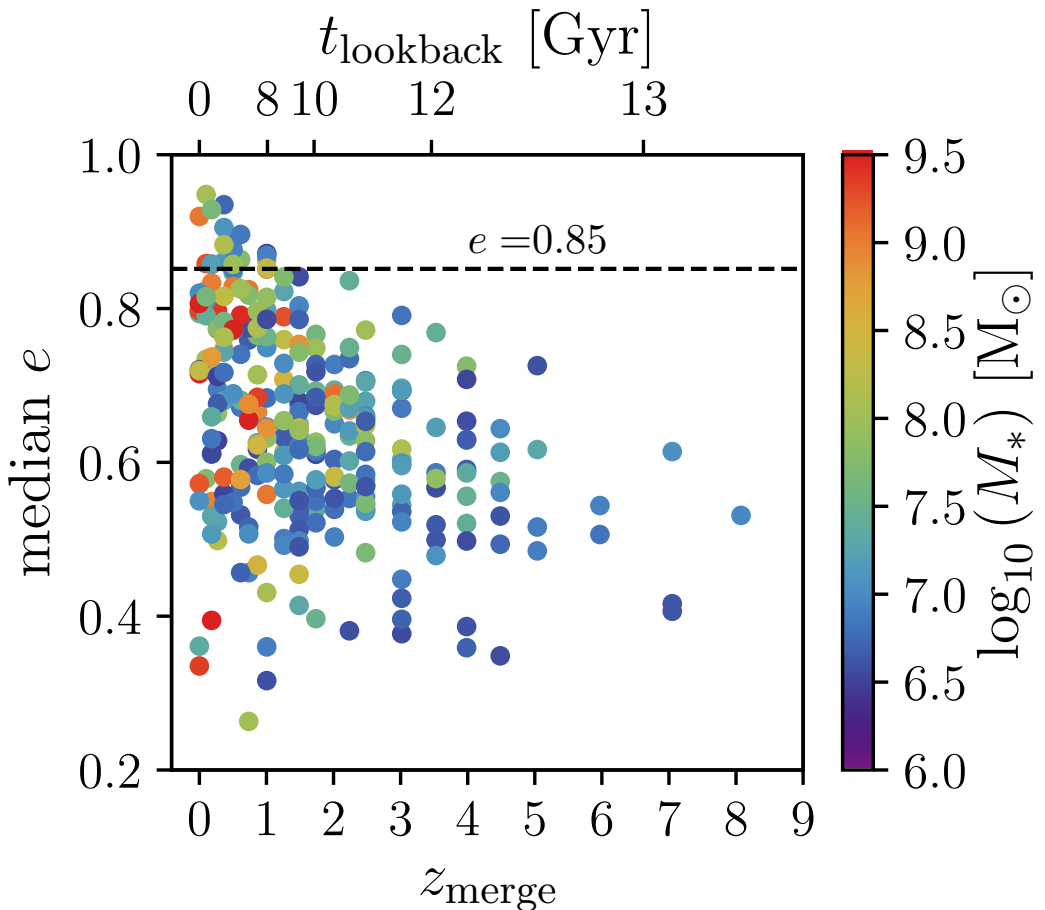


Figure 3.9: The merger time  $z_{\text{merge}}$  of satellites accreted onto 22 Milky Way mass haloes in EAGLE against the median eccentricity  $e$  of their stellar debris at  $z = 0$ . The points are coloured by the stellar mass of the accreted galaxies at the time of the merger,  $M_*$ . The dashed horizontal line indicates  $e = 0.85$ , which is the median eccentricity of the high  $e$  group characterised in Section 3.3. Only the latest merged haloes have debris at the highest and lowest  $e$ , whereas early mergers tend to occupy intermediate  $e$ . The most massive mergers also occur later, with early mergers dominated by low mass haloes.

ual eccentricity distributions of accreted debris compare well to the distributions we find in the Milky Way halo groups in terms of shape and their being unimodal. In Figure 3.9, we show the median  $e$  of these distributions against  $z_{\text{merge}}$  for accreted satellites onto the 22 Milky Way virial mass ( $\sim 10^{12} M_{\odot}$ ) galaxies in the EAGLE L025N752-Recal simulation. We colour each point by the stellar mass reached by the progenitor population prior to merging onto the main branch. The median eccentricity of the high  $e$  group in the Milky Way halo is indicated as a dashed horizontal line. To ensure that we properly resolve the orbital properties of the stellar component of the accreted satellites, we only show galaxies with 20 or more star particles, amounting to a total of 296 accreted satellites.

There is a striking trend of median  $e$  with  $z_{\text{merge}}$  in Figure 3.9. The maximum median  $e$  decreases with lookback time, creating an upper envelope to the distribution of data. As a result,  $z = 0$  stellar particles resulting from the earliest accretions typically have median  $e \sim 0.5$ , whereas the most recently accreted satellites occupy a large range of median  $e$  from  $\sim 0.3$  up to  $> 0.9$ . As we discuss below, this means that early accreted satellites were accreted onto intermediate to low  $e$  orbits. Most importantly, this result indicates that an accreted satellite with stars at  $z = 0$  on very radial orbits is unlikely to have been accreted earlier than  $z \sim 1.5$ . We discuss the implications of this finding for the formation of the Milky Way thick disc, as suggested by ?, in Section 3.5.

As expected from hierarchical clustering in a standard  $\Lambda$ -CDM universe, it can be seen in Figure 3.9 that, at the highest redshifts, merged satellite galaxies are relatively low mass. Conversely, those that were accreted more recently are the most massive. Almost all accretion of stellar systems with  $M_* 10^9 M_{\odot}$  happened at  $z \sim 1$ . This is mainly due to the time taken for satellites to build up their stellar mass. The fact that the satellite debris with the highest median  $e$  must have been accreted late also means that these satellites are likely to be high mass. We find that the median mass of accreted satellites with median  $e > 0.85$  is  $4.1 \times 10^8 M_{\odot}$ , and a minimum mass of  $0.77 \times 10^8 M_{\odot}$ . The median accretion time of high  $e$  debris is  $z \sim 0.6$ . This suggests that the high  $e$  Milky Way halo population we identify is likely to have had  $M_* \gtrsim 10^8 M_{\odot}$  and have been accreted after  $z \sim 1.5$ . Accretion events such as this are relatively rare in EAGLE,

with only 5 of the 22 ( $\sim 23\%$ ) central galaxies having accreted any system with  $10^8 < M_* < 10^9 M_\odot$  after  $z = 1.5$  *and* retaining a median  $e > 0.8$  at  $z = 0$ . For two of those five simulated galaxies, the aggregate of all accreted stellar mass far exceeds that of the Galactic halo (e.g. by a factor of 2 or more), leaving only 3 galaxies ( $\sim 14\%$ ) with accretion profiles resembling that suggested by the observations reported in this paper. It is also worth noticing that the high  $e$  populations of the latter three galaxies, although dominated by one massive accretion event, had not insignificant contributions by accretions of smaller mass systems. The latter suggests that it is possible that the high  $e$  population of the Galactic halo may have contributions by low mass systems as well.

Perhaps most importantly, the above discussion indicates that the accretion event which deposited the high  $e$  Milky Way debris was quite unusual for a galaxy of its  $z = 0$  virial mass. If one further considers that the Milky Way is currently accreting a similarly massive galaxy (the Sagittarius Dwarf), our results suggest that the overall accretion history of the Milky Way has been quite atypical when compared to the rest of the galaxies of same halo mass. This is an interesting result in light of the findings reported by ?, that suggest the Milky Way, by its  $[\alpha/\text{Fe}]-[\text{Fe}/\text{H}]$  abundance pattern, may be an outlier in terms of accretion history, for it's stellar mass. The Milky Way becomes even more unusual in this sense, if one considers the very massive *Kraken* accretion event proposed by ?. We discuss the implications of that work further in Section 3.5.

In Figure 3.10, we show how the eccentricity of satellite debris changes between the time of the merger and  $z = 0$ . We measure the initial eccentricity by taking the median eccentricity of the star particles in the snapshot immediately following that in which the satellite is identified as being merged onto the main progenitor. It is clear from this figure that the orbit eccentricities are not greatly changed following accretion. The median change in eccentricity is small, at  $\sim 4\%$ , although a few accreted satellites have changed their median eccentricity by as much as  $\sim 20\%$ . It is noticeable that the debris whose eccentricity has changed most is that from lower mass satellites. As noted previously, these are the satellites commonly accreted earlier, although we find no significant trend between  $z_{\text{merge}}$  and the change in eccentricity, meaning that

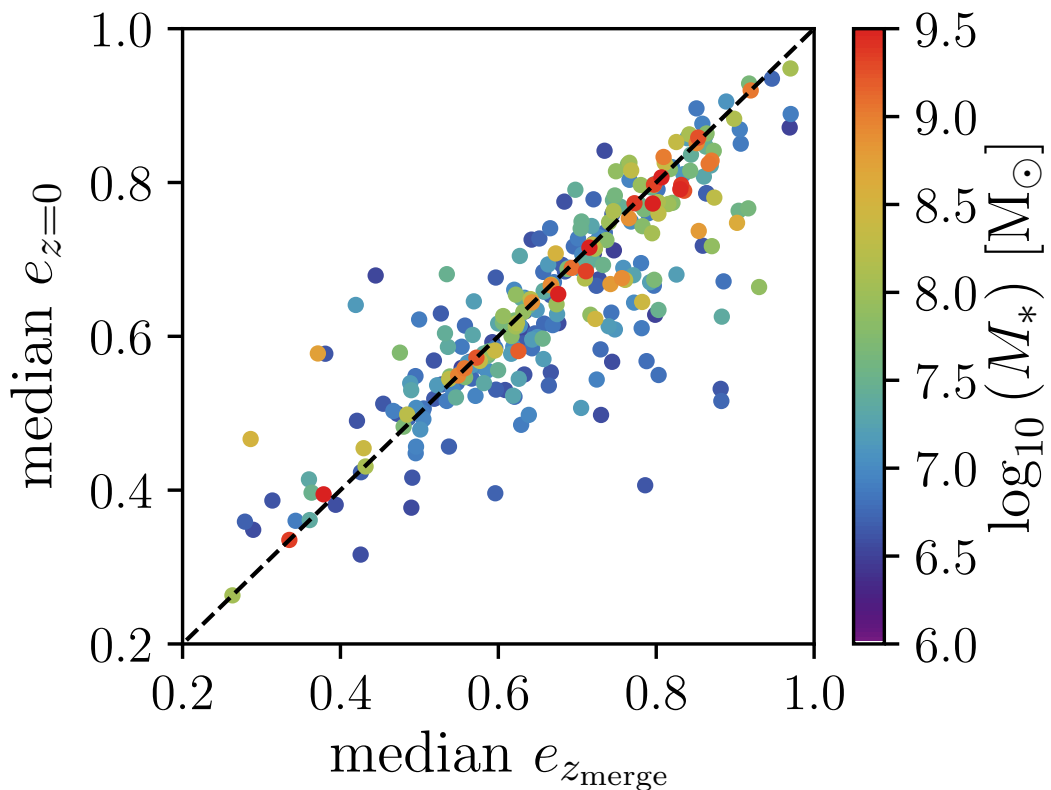


Figure 3.10: Median eccentricities at merger time  $e_{z_{\text{merge}}}$  against median eccentricity at  $z = 0$   $e_{z=0}$  for satellites accreted onto Milky Way mass haloes in EAGLE. The points are coloured by the stellar mass of the accreted galaxies at the time of the merger,  $M_*$ . Debris which falls below the dashed unity line has been circularised following accretion, whereas the debris above this line has been radialised after accretion. The majority of debris has a similar  $e$  at  $z = 0$  to the time at which it was accreted, but a few accreted satellites are circularised/radialised following accretion. High mass satellite debris has undergone the least change in median  $e$ .

changes in the median  $e$  are not strongly time dependent. By the same token, the highest mass satellite debris are those which have undergone the least change in median  $e$ , likely because they were accreted late, when the gravitational potential of the host dark matter halo is no longer varying significantly. Furthermore, no satellites accreted at lower  $e$  than  $\sim 0.7$  have debris that is radialised to higher than  $e \sim 0.8$  by  $z = 0$ . The finding that median  $e$  changes very little is important, as it means that the trend between  $z_{\text{merge}}$  and median  $e$  at  $z = 0$  (Figure 3.9) is cosmological in nature, and not due to dynamical effects, substantiating the idea that high orbit eccentricity is a good indicator of late-time accretion. The trend between  $z_{\text{merge}}$  and median  $e$  is likely a product of the changing merger cross-section with cosmic time, whereby the gravitational potential of the central halo dictates the maximum impact parameter for a successful accretion (as opposed to a “fly-by”). Galaxies in the early universe are smaller and less massive, and so approaching satellites must have a smaller impact parameter to be accreted. For instance, for a galaxy with  $r_{\text{vir}} \sim 50$  kpc,  $r_{\text{peri}}$  must be  $< 5.5$  kpc for  $e > 0.8$ , whereas for  $r_{\text{vir}} \sim 250$  kpc,  $r_{\text{peri}}$  can be as high as  $\sim 28$  kpc for a similar orbit, assuming  $r_{\text{vir}}$  determines the maximum  $r_{\text{apo}}$ . This logic supports our contention that the high  $e$  group in the Milky Way must have been a relatively late accretion event.

Regarding the low  $e$  group, the numerical simulations reinforce the notion that it may be contributed by a combination of smaller and/or earlier accretion events. Given that intermediate  $e$  populations can be accreted at almost any  $z_{\text{merge}}$  in EAGLE, and that the element abundances of this group show no clear [Mg/Fe] change of slope in the [Fe/H] range observed and no clear MDF peak at moderately high [Fe/H], it is then most likely that these stars were accreted at earlier times than the high  $e$  stars, and in small satellites. In general, earlier and lower mass accreted satellites in the simulation show  $\alpha$ -element enhancements, due to the fact that these must have formed quickly (with high SFE) to be accreted at early times.

## 3.5 Summary and Conclusions

This paper presents an analysis of chemical compositions and orbital information of accreted halo populations, based on APOGEE and Gaia data. We applied k-means clustering to identify subgroups in chemical composition and kinematics space, considering the abundances of  $\alpha$ , odd-Z and Fe peak elements, and orbital eccentricity. We have shown that  $\sim 2/3$  of the accreted halo stars exhibit very high orbital eccentricity and display chemical compositions that are characteristic of those seen in massive dwarf galaxy satellites of the Milky Way today, suggesting that this population is likely the progeny of a single, massive accretion event which occurred early in the history of the Milky Way Galaxy. The remaining 1/3 of the sample consists of stars with low orbital eccentricities and slightly higher abundance ratios than the high  $e$  population. The latter stars likely result from a mixture of different origins, including the remnants of less massive accretion events, *in situ* star formation, disc heating, and likely some contamination from the high  $e$  population.

We further examine this scenario by studying a numerical simulation from the EAGLE suite. We demonstrate that satellite galaxies accreted into MW mass haloes show clear trends between the time of accretion and the median eccentricity of the accreted stars at  $z = 0$ . The results from the simulations predict that debris with  $e > 0.8$ , like that of the population identified in this paper and by other groups (e.g. ?????) is only realised at  $z = 0$  for satellites accreted after  $z \sim 1.5$ . This constraint also means that such satellites are likely to be accreted at relatively high stellar mass ( $M_* \gtrsim 10^8 M_\odot$ ). We also showed that, according to the simulation, the median eccentricity of accreted debris generally does not appear to evolve significantly over time, further suggesting that a high orbital eccentricity is a good indicator of a relatively recent merger. Analysis of the numerical simulations further suggests that a massive accretion event such as that identified in the APOGEE/Gaia data is not very common for a Milky Way-like galaxy, suggesting an unusual accretion history in same vein as suggested in previous work by e.g. ?.

Recently, various accretion events have been reported by different groups. The high  $e$

population identified in the combined APOGEE/Gaia DR2 sample appears to be the same population as those discovered by ?, ? and ?. We have shown that the kinematics of the high  $e$  group is consistent with that found in these studies, having very low, slightly negative  $L_z$  consistent with the ? population, and  $r_{\text{ap}}$  as high as 40 kpc, with a median of 15.1 kpc, and a suggestive secondary peak at  $r_{\text{ap}} > 20$ , in rough consistency with the ? population. Our high  $e$  population has a median eccentricity in good agreement with those of the populations discussed by ? and the clusters measured by ?.

? suggest that the age-metallicity distribution of the Galactic globular cluster population can be used to infer the formation and assembly history of the Milky Way. They identify one very massive ( $M_* > 10^9 M_\odot$ ) accretion event (*Kraken*), which is associated with the overabundance of metal-rich GCs in the accreted cluster branch of the age-metallicity relation and has no known debris. This is not consistent with the accretion event identified in this paper, as it is both too massive, and likely not associated with the accreted GCs identified by ?. *Kraken* is more plausibly associated with GCs that reside inside 5 kpc from the Galactic center. It is more possible then that the population reported in this paper (and by connection, likely also that of, e.g. ?????) is associated with the less massive *Canis Major* accretion that was identified by ?. The clusters identified by ?, are more easily linked with this event, which ? argue is the progenitor of many of the GCs at Galactocentric radii  $> 10$  kpc. In summary, all of these results point towards confirmation that the assembly history of the Milky Way has been very active, and quite atypical compared to other galaxies of a similar mass.

? suggest that their population, *Gaia-Enceladus*, is the debris from an accretion event that caused the dynamical heating of the precursor to thick disc component of the Milky Way, having been accreted approximately 10 Gyr ago. The results from analysis of EAGLE suggest that if the debris at  $e \sim 0.85$  was accreted in a single satellite, then this may have occurred around 8-9 Gyr ago (Figure 3.9). The ? merger time is based on the minimum isochronal age of the stars in their sample so it is possibly indicative of the final time of star formation rather than the actual accretion time. On the other hand, EAGLE gives the time at which the satellite became bound to the central halo, so

these timescales are potentially consistent. Ages of stars in the Milky Way high  $[\alpha/\text{Fe}]$  disc population are generally found to be older than or similar to  $\sim 10$  Gyr (e.g. ???), so this does suggest that this population was in place before the merger occurred. It is worth mentioning here, however, that analysis of the origin of  $\alpha$ -enhanced populations in EAGLE suggest that these stars must form in an early collapse in a period of rapid gas accretion, in order to foster the high density ISM necessary to generate a short enough gas consumption time to consume the high  $[\alpha/\text{Fe}]$  gas into stars before it is polluted by SN Ia (?), rather than forming in a ‘primordial’ disc which would then be heated. This scenario is consistent with the ‘thick disc’ being the result of the geometric combination of the thick, centrally concentrated high  $[\alpha/\text{Fe}]$  disc and the extended, flared low  $[\alpha/\text{Fe}]$  disc (e.g. ???). Further work on this newly found halo component, and the high  $[\alpha/\text{Fe}]$  disc, will surely shed more light on this discussion.

### 3.6 Modelling as a function of [Fe/H]

In order to test whether a change in slope is found in the relationship between  $\alpha/\text{Fe}$  and  $[\text{Fe}/\text{H}]$  in the identified accreted halo groups, we use a Bayesian inference to fit a piecewise-linear model to the data. The form of the piecewise-linear function is given in Equation 3.3. We follow the general procedure outlined in Section 7 of ? for fitting models to data with two-dimensional uncertainties. For completeness, we re-iterate here the mathematics. The best fitting model is found by maximising the likelihood function for the parameters  $O = [[\text{Fe}/\text{H}]_0, [\text{Mg}/\text{Fe}]_0, \theta_1, \theta_2]$  given the data, which we assume here to be of the form

$$\ln \mathcal{L}(O | [\text{Fe}/\text{H}], [\text{Mg}/\text{Fe}]) = K - \sum_{i=1}^N \left( \frac{\Delta_i^2}{2\Sigma_i^2} + \ln |\Sigma_i^2| \right) \quad (3.4)$$

where  $\Delta_i^2$  defines the distance between the data-point  $i$  and the model, and  $\Sigma_i^2$  is the variance orthogonal to the model, determined by the covariance matrix of the data points.  $K$  is a normalisation constant, which is not necessary to consider in the optimisation. We assume uninformative flat priors on  $\theta_{[1,2]}$ , and allow  $[\text{Fe}/\text{H}]_0$  and  $[\text{Mg}/\text{Fe}]_0$

to be free. In this case,  $\Delta_i^2$  is defined by

$$\Delta_i^2 = \hat{\mathbf{v}}^T \mathbf{Z}_i - b \cos \theta_{[1,2]} \quad (3.5)$$

where  $\mathbf{Z}_i$  is the column vector made by  $(,[\text{Fe}/\text{H}])_i$ , and  $\hat{\mathbf{v}}$  is the unit vector orthogonal to the model:

$$\hat{\mathbf{v}} = \frac{1}{\sqrt{1 + m_{[1,2]}^2}} \begin{bmatrix} -m_{[1,2]} \\ 1 \end{bmatrix} = \begin{bmatrix} -\sin \theta_{[1,2]} \\ \cos \theta_{[1,2]} \end{bmatrix} \quad (3.6)$$

where  $\theta_{[1,2]}$ , here and in Equation (3.5), is the angle between the linear model at that [Fe/H] and the x-axis, which is equal to  $\arctan m_{[1,2]}$ .  $\Sigma_i^2$  is then simply defined as the projection of the data-point's covariance matrix  $\mathbf{S}_i$  orthogonal to the model at that [Fe/H]

$$\Sigma_i^2 = \hat{\mathbf{v}}^T \mathbf{S}_i \hat{\mathbf{v}}. \quad (3.7)$$

In this case, we assume that the uncertainties on  $\delta[\text{Fe}/\text{H}]$  and  $\delta[\text{Mg}/\text{Fe}]$  are uncorrelated, such that

$$\mathbf{S}_i = \begin{bmatrix} \delta[\text{Fe}/\text{H}]_i & 0 \\ 0 & \delta[\text{Mg}/\text{Fe}]_i \end{bmatrix} \quad (3.8)$$

where we use the catalogue values for the uncertainties on [Fe/H] and  $\delta[\text{Mg}/\text{Fe}]$ . We minimise the negative log-likelihood using a downhill simplex algorithm (?), and use this optimal solution to initiate an Markov Chain Monte Carlo (MCMC) sampling of the posterior PDF of the parameters  $\mathbf{O}$  using an affine-invariant ensemble MCMC sampler (?) as implemented in the python package emcee (?). We report the median and standard deviation of this posterior PDF as our best-fit parameters.

# Appendix A

## Example Appendix

Lorem ipsum dolor sit amet, consectetuer adipiscing elit. Ut purus elit, vestibulum ut, placerat ac, adipiscing vitae, felis. Curabitur dictum gravida mauris. Nam arcu libero, nonummy eget, consectetuer id, vulputate a, magna. Donec vehicula augue eu neque. Pellentesque habitant morbi tristique senectus et netus et malesuada fames ac turpis egestas. Mauris ut leo. Cras viverra metus rhoncus sem. Nulla et lectus vestibulum urna fringilla ultrices. Phasellus eu tellus sit amet tortor gravida placerat. Integer sapien est, iaculis in, pretium quis, viverra ac, nunc. Praesent eget sem vel leo ultrices bibendum. Aenean faucibus. Morbi dolor nulla, malesuada eu, pulvinar at, mollis ac, nulla. Curabitur auctor semper nulla. Donec varius orci eget risus. Duis nibh mi, congue eu, accumsan eleifend, sagittis quis, diam. Duis eget orci sit amet orci dignissim rutrum.

Nam dui ligula, fringilla a, euismod sodales, sollicitudin vel, wisi. Morbi auctor lorem non justo. Nam lacus libero, pretium at, lobortis vitae, ultricies et, tellus. Donec aliquet, tortor sed accumsan bibendum, erat ligula aliquet magna, vitae ornare odio metus a mi. Morbi ac orci et nisl hendrerit mollis. Suspendisse ut massa. Cras nec ante. Pellentesque a nulla. Cum sociis natoque penatibus et magnis dis parturient montes, nascetur ridiculus mus. Aliquam tincidunt urna. Nulla ullamcorper vestibulum turpis. Pellentesque cursus luctus mauris.

Nulla malesuada porttitor diam. Donec felis erat, congue non, volutpat at, tincidunt

tristique, libero. Vivamus viverra fermentum felis. Donec nonummy pellentesque ante. Phasellus adipiscing semper elit. Proin fermentum massa ac quam. Sed diam turpis, molestie vitae, placerat a, molestie nec, leo. Maecenas lacinia. Nam ipsum ligula, eleifend at, accumsan nec, suscipit a, ipsum. Morbi blandit ligula feugiat magna. Nunc eleifend consequat lorem. Sed lacinia nulla vitae enim. Pellentesque tincidunt purus vel magna. Integer non enim. Praesent euismod nunc eu purus. Donec bibendum quam in tellus. Nullam cursus pulvinar lectus. Donec et mi. Nam vulputate metus eu enim. Vestibulum pellentesque felis eu massa.

Quisque ullamcorper placerat ipsum. Cras nibh. Morbi vel justo vitae lacus tincidunt ultrices. Lorem ipsum dolor sit amet, consectetur adipiscing elit. In hac habitasse platea dictumst. Integer tempus convallis augue. Etiam facilisis. Nunc elementum fermentum wisi. Aenean placerat. Ut imperdiet, enim sed gravida sollicitudin, felis odio placerat quam, ac pulvinar elit purus eget enim. Nunc vitae tortor. Proin tempus nibh sit amet nisl. Vivamus quis tortor vitae risus porta vehicula.

Fusce mauris. Vestibulum luctus nibh at lectus. Sed bibendum, nulla a faucibus semper, leo velit ultricies tellus, ac venenatis arcu wisi vel nisl. Vestibulum diam. Aliquam pellentesque, augue quis sagittis posuere, turpis lacus congue quam, in hendrerit risus eros eget felis. Maecenas eget erat in sapien mattis porttitor. Vestibulum porttitor. Nulla facilisi. Sed a turpis eu lacus commodo facilisis. Morbi fringilla, wisi in dignissim interdum, justo lectus sagittis dui, et vehicula libero dui cursus dui. Mauris tempor ligula sed lacus. Duis cursus enim ut augue. Cras ac magna. Cras nulla. Nulla egestas. Curabitur a leo. Quisque egestas wisi eget nunc. Nam feugiat lacus vel est. Curabitur consectetur.

Suspendisse vel felis. Ut lorem lorem, interdum eu, tincidunt sit amet, laoreet vitae, arcu. Aenean faucibus pede eu ante. Praesent enim elit, rutrum at, molestie non, nonummy vel, nisl. Ut lectus eros, malesuada sit amet, fermentum eu, sodales cursus, magna. Donec eu purus. Quisque vehicula, urna sed ultricies auctor, pede lorem egestas dui, et convallis elit erat sed nulla. Donec luctus. Curabitur et nunc. Aliquam dolor odio, commodo pretium, ultricies non, pharetra in, velit. Integer arcu est, nonummy in, fermentum faucibus, egestas vel, odio.

Sed commodo posuere pede. Mauris ut est. Ut quis purus. Sed ac odio. Sed vehicula hendrerit sem. Duis non odio. Morbi ut dui. Sed accumsan risus eget odio. In hac habitasse platea dictumst. Pellentesque non elit. Fusce sed justo eu urna porta tincidunt. Mauris felis odio, sollicitudin sed, volutpat a, ornare ac, erat. Morbi quis dolor. Donec pellentesque, erat ac sagittis semper, nunc dui lobortis purus, quis congue purus metus ultricies tellus. Proin et quam. Class aptent taciti sociosqu ad litora torquent per conubia nostra, per inceptos hymenaeos. Praesent sapien turpis, fermentum vel, eleifend faucibus, vehicula eu, lacus.